UNIVERSITÀ DEGLI STUDI DI PALERMO
DIPARTIMENTO DI INGEGNERIA
Dottorato di Ricerca in Information and Communication Technologies

Development of Wearable Technologies and Biosignal Processing Methods for the Assessment of Physiological States

Ph. D. Candidate:
Ing. Gabriele Volpes

Tutor:
Prof. Luca Faes

Cotutor:
Prof. Riccardo Pernice

XXXVI CICLO - ANNO ACCADEMICO 2022 - 2023

DOTTORATO

To my grandfather Vincenzo, whose love and wisdom have shaped me into the person I am today

ACKNOWLEDGEMENTS

Firstly, I would like to express my authentic gratitude to my supervisors, Luca Faes and Riccardo Pernice, for accompanying me throughout this long doctoral journey, offering invaluable advice and sharing their experience in academic research with me. Without their support and presence, I would not have been able to acquire the skills I possess today.

A sincere thanks goes to professors Goran Stojanovic and Varun Jeoti, who warmly welcomed me into their Electronics laboratory at the University of Novi Sad during the foreign research period, allowing me to broaden my cultural and international research experience. Their availability from the very beginning has been of fundamental importance to my research path, giving rise to a fruitful academic collaboration that continues to endure to this day.

Also, I would like to thank all the research colleagues I have met over the years: Giuseppe, Hima, Yuri, Chiara, Laura, Valeria, Roberta, Marta, and all the others. I am very grateful to have spent this time with them as well.

A special thanks goes to my dear friend and colleague Simone, with whom I have shared and enjoyed every single moment of this intense journey, from the challenging and difficult experiences to the joyful and rewarding moments.

A heartfelt thanks goes to Mariachiara, my dear friend who has supported me throughout this intense but fulfilling journey.

Finally, I would like to express my deep gratitude to my family, especially my parents Francesca and Ignazio, my sister Alice, and my dear friend Giuseppe, who is now a part of it, for supporting me unconditionally and always believing in me.

SUMMARY

In recent years, scientific breakthroughs in the biomedical field have spurred a growing interest in healthcare, driving research and development of increasingly sophisticated biomedical devices and data analysis algorithms capable of providing crucial information for the assessment of individual well-being. Among these, Wearable Health Devices (WHDs) stand out as some of the most sought-after technologies, thanks to their capability of being comfortably worn by the user and of allowing non-invasive and comfortable monitoring of the subject's health state through the acquisition of key physiological parameters. The user-friendly design, reduced weight and size, and the escalating performance in terms of energy efficiency and measurement accuracy incentivize the massive research and development of WHDs, suggesting their application as biomedical devices for monitoring not only vulnerable but also healthy individuals. These features pave the way to the prospective use of WHDs as helpful tools in the clinical setting for early diagnosis, potentially averting the onset of specific pathologies and helping to alleviate the workload of the healthcare system.

Similarly, recent developments in the biomedical and clinical fields have involved the implementation and utilization of advanced data analysis algorithms that, starting from the raw signals acquired by biomedical devices, perform the extraction of important physiological indices for a more accurate assessment of organ functionality and individual physiological state. In fact, the growing interest from the scientific community in the field of biomedical signal processing has allowed researchers to identify new methodologies for the analysis and interpretation of biomedical data. This has brought to light innovative metrics, such as those derived from the information-theoretic domain and multivariate biomedical analysis, enabling the extraction of additional physiological indices to obtain novel insights into the dynamics of organ functions and their mutual influence in physiological and pathological states, thus allowing for a more comprehensive picture of physiological mechanisms and clinically relevant states. It appears evident how the combined and appropriate use of WHDs and algorithms for biomedical signal processing and analysis can be of fundamental importance in the healthcare context.

For this reason, there is a need to continue researching and developing increasingly cutting-edge wearable technologies that enable multiparametric acquisition and the implementation of data analysis algorithms for the extraction and interpretation of standard and advanced physiological indices.

This thesis addresses the concepts outlined above by (i) introducing a novel wearable biomedical device which has been specifically designed and realized to perform multiparametric and non-invasive acquisition of multiple biosignals detected in the same body area, and (ii) exploring both novel and standard techniques for biomedical data analysis to extract physiological indices capable of detecting diverse physiological states. Specifically, the realized device has been designed to be worn on the forefinger of the hand, it is user-friendly and allows for the acquisition of electrocardiographic (ECG), photoplethysmographic (PPG), skin conductance (SC), and motion signals. The device incorporates sensors for the non-invasive and comfortable acquisition, transmitting the data via a Bluetooth Low Energy (BLE) communication protocol to a computer equipped with a user interface specifically developed for the communication with the device, as well as for the real-time visualization and storage of the acquired data.

The ability to easily and efficiently extract important physiological indexes simultaneously from the ECG and PPG, along with the acquisition of the SC signal, allow to employ the device for detecting physiological states, identifying conditions of physical and mental stress, and assessing cardiovascular system functionality, also enabling an investigation into the potential of the realized wearable device as diagnostic and monitoring tool in everyday life. It is for this reason that the thesis also addresses biomedical signal processing and analysis, introducing and investigating about post-processing and filtering operations on the acquired biosignals that lead to the extraction of different physiological parameters, such as respiratory rate, as well as the computation of physiological indices obtained from the time series of interest, such as RRI and PPI series (i.e., the time periods between successive heartbeats), that are obtained respectively from ECG and PPG signals. The thesis then explores Heart Rate Variability (HRV) analysis, which is a valid and widely used tool for the assessment of stress states, for extracting physiological indices in the time, frequency, and novel information-theoretic domains, over standard 5-minute time windows, performing what is well-known in the literature as Short-Term (ST) analysis.

Furthermore, the work evaluates the feasibility of Ultra-Short-Term (UST) analysis, exploring an area which is currently under research and, due to the lower constraints associated with analyzing a very short time window, could represent a breakthrough in implementing this kind of analysis directly on wearable devices.

Finally, the developed wearable device was employed in a measurement campaign aimed at preliminary validation of its use for detecting physiological states. This was achieved through the implementation of the discussed data analyses conducted using the recordings of biosignals acquired by the device.

Data analysis algorithms are employed on the signals acquired by the realized wearable device, as well as other biomedical devices that has been used to collect biosignals, to evaluate the potential use of innovative indices, such as those obtained in the frequency and the information theoretical domain. Indeed, not all the analyses presented here were conducted on signals recorded with the wearable device, but the results of the analyses still serve to identify indices to be implemented on the wearable device in future developments of the present thesis work.

In the first chapter, the main topic is introduced, presenting the potential of wearable biomedical devices along with the importance of developing non-invasive measurement methodologies and biomedical data analysis. These cutting-edge technologies aim to make healthcare accessible to everyone, effectively enhancing health awareness in civil, industrial, and clinical domains. Chapter 2 provides the background on which this work is based, introducing the relevant biosignals and subsequently presenting the methods that illustrate the types of data analysis employed. Chapter 3 covers the design and development of the ring-shaped device from the hardware, firmware, and software perspectives. Finally, Chapter 4 reports the results of the data analysis conducted on the processed biosignals, as well as the measurement campaign using the ring-shaped device to preliminarily validate its use for detecting physiological states.

CONTENTS

List of Figures

List of Tables

List of Abbreviations

ADC – Analog-to-Digital Converter

AFE – Analog front-end

AIC – Akaike Information Criterion

ANS – Autonomic Nervous System

AR – Autoregressive

BLE – Bluetooth Low Energy

BMS – Battery Management System

BP – Blood Pressure

CB – Controlled Breathing

CE – Conditional Entropy

CSV – Comma-Separated Values

DE – Dynamic Entropy

ECG – Electrocardiography

ENIG – Electroless Nickel Immersion Gold

EMD – Empirical Mode Decomposition

FFT – Fast Fourier Transform

GAS – General Adaptation Syndrome

GSR – Galvanic Skin Response

GUI – Graphic-User Interface

HAL – Hardware Abstraction Layer

HASL – Hot Air Solder Leveling

HF – High-Frequency

HP – Heart Period

HR – Heart Rate

HRV – Heart Rate Variability

I^2C – Inter-Integrated Circuit

ICT – Information and Communicaton Technologies

IoMT – Internet of Medical Things

IRF – Impulse Response Function

LED – Light Emitting Diode

LF – Low-Frequency

LT – Long-Term

MCU – Microcontroller

NTC – Negative Thermistor

PAT – Pulse Arrival Time

PC – Personal Computer

PCB – Printed Circuit Board

PNS – Parasympathetic Nervous System

PPG – Photoplethysmogaphy

PPI (or **PP**) – Pulse-to-Pulse Interval

PRV – Pulse Rate Variability

PSD – Power Spectral Density

RISC – Reduced Instruction Set Computer

RLD – Right Leg Drive

RMSSD – Root Mean Square of Successive Differences

RRI (or **RR**) – R-to-R Interval

RSA – Respiratory Sinus Arrythmia

SaO_2 – Arterial Oxygen Saturation

SAP – Systolic Arterial Pressure

SB – Spontaneous Breathing

SC – Skin Conductance

SCL – Skin Conductance Level

SCR – Skin Conductance Response

SDNN – Standard Deviation of the interbeat interval between normal sinus beats

SE – Static Entropy

SNS – Sympathetic Nervous System

SpO_2 – Pulsoxymetrically measured Oxygen Saturation

ST – Short-Term

STD – Standard Deviation

U-ART – Universal-Asynchronous Receiver/Transmitter

ULF – Ultra-Low-Frequency

USB – Universal Serial Bus

UST – Ultra-Short-Term

VLF – Very-Low-Frequency

WHD – Wearable Health Device

CHAPTER 1

INTRODUCTION

1.1 MONITORING IN HEALTHCARE

The rapid advent of new technologies characterizing the current era, coupled with an increased awareness and understanding of human health, is leading to a growing interest and attention to healthcare [1], [2], [3]. In particular, the term "healthcare" refers to the collective set of all facilities, individuals, and processes involved in patient care and health protection within a society [4], [5]. Key actors in the healthcare system include medicians and hospitals as service providers, and more recently, emerging ICT and biomedical technologies that have paved the way for the field of Telemedicine: a new biomedical sector which seeks to redefine the concept of healthcare enabling continuous remote monitoring and real-time interconnection among patients, doctors, and healthcare facilities [6], [7], [8] thanks to cutting-edge technologies.

The growing interest in healthcare is driven by various factors originating primarily in civil, industrial, and clinical fields, which, when combined, result in the increasing need to pursue the health-status assessment by monitoring key physiological parameters. Furthermore, the ability to leverage Information and Communication Technologies (ICT) to pursue healthcare in the contexts just introduced has recently given rise to new fields, such as Industry 4.0 and the Internet of Medical Things (IoMT), complementing Telemedicine and Clinical Monitoring as sub-branches of nowadays healthcare, as summarized in Figure 1.1. In particular, the purpose varies depending on whether it pertains to the civil field, where there is a simple intention for a healthy individual to obtain feedback about their health status during daily life routines, the industrial field, where the typical need is to monitor the health of workers to prevent potential individual and collective dangers, or the clinical field, where there is a requirement to conduct routine examinations and monitor vulnerable individuals within healthcare environments and remotely during the convalescence [9], [10], [11], [12], [13].

As a consequence, it is therefore quite clear that healthcare monitoring is a very broad concept, encompassing the assessment of health status through numerous approaches, ranging from basic lifestyle monitoring to the screening of primary pathologies, depending on the context in which one is operating.

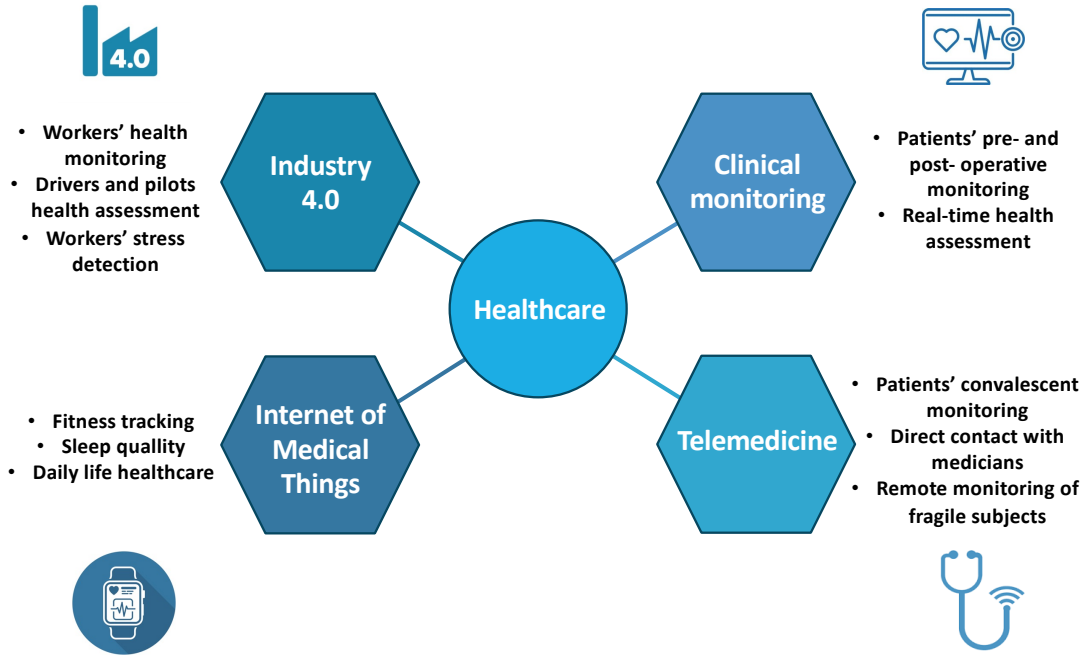

Figure 1.1 *– Conceptualization of healthcare and its importance in application scenarios in civil, industrial and clinical settings.*

Regardless of the application field, monitoring in healthcare is often pursued through the acquisition of different biosignals, from which it is possible to extract main physiological indices for assessing the functionalities of the organism [8], [14], [15]. Indeed, although the monitoring of biosignals is a small part of the vast landscape of healthcare, they represent the starting point not only for assessing health status, but also for identifying the potential onset or presence of certain pathologies, which will then be confirmed through specific screening and investigations.

Starting with the cardiovascular system, which is undoubtedly one of the most crucial, monitoring involves the recording of the electrocardiogram (ECG) and blood pressure (BP) levels [16], [17]. A comprehensive health monitoring also includes the assessment of blood oxygenation levels and respiratory rate, allowing for the evaluation of respiratory system functions [18], [19], [20].

Additionally, other parameters are typically recorded, such as movement, which helps recognize physical activity or potential involuntary tremors in the subject, body temperature, and levels of epidermal sweating, which could contribute to identifying the occurrence of stressful events [21], [22]. Lastly, building on this concept, it is essential to highlight the importance of detecting the activity of the autonomic nervous system (ANS), which directly and indirectly controls the mechanisms regulating the functions of all other systems and, thus, the organism itself [23], [24]. Its activity can be discerned from indices extracted from the data derived from all the aforementioned biosignals: consequently, understanding the levels of activation of the ANS is important to comprehend changes in the dynamics of other signals and physiological indices, in addition to providing information about changes individual physiological state.

Thanks to continuous advancements in technologies and electronic miniaturization process, today it is possible to find a huge number of biomedical devices aiding healthcare that can record a multitude of high-quality biosignals [25], [26]. Although many of them enable the acquisition of a wide range of biosignals using relatively little space in a non-invasive manner, only a few manage to do so without causing discomfort to the user. It is precisely for this reason that current research in this field is focused on developing increasingly compact and comfortable devices and studying non-invasive measurement methodologies for the extraction of the main physiological indices, with the final aim is to make biomedical devices user-friendly and comfortable even for inexperienced users, which is a fundamental requirement to integrate healthcare into everyday life.

1.2 NON-INVASIVE MONITORING IN HEALTHCARE APPLICATIONS

From the possibility of leveraging modern technologies to make healthcare accessible to everyone, there arises the need to identify, as mentioned earlier, measurement methodologies for biosignals that are non-invasive and easy to implement. In response to this, significant strides have been made over the years, leading to two main solutions to the problem [27], [28]. The first solution involves the ability to exploit increasingly compact and efficient electronic components, enabling the biosignal acquisition using the same measurement methodology, with the advantage of significantly reducing the weight and size of the probes worn by the user and the instrumentation needed to obtain the signal, thus allowing for less invasive and more comfortable measurements.

Moreover, the possibility of integrating a multitude of sensors into a single compact biomedical device has thus made it feasible to realize and commercialize multiparametric biomedical devices, which consist of single devices that integrate a multitude of biomedical sensors to allow the simultaneous acquisition of multiple biosignals and thus the extraction of several physiological parameters.

The second solution involves implementing non-invasive and alternative measurement methodologies, or at least less pervasive than standard ones (Figure 1.2), to obtain the same physiological index or alternative surrogates. Examples of this solution include the use of photoplethysmographic (PPG) technology, a non-invasive and easily deployable technique compared to ECG, for detecting heart rate and its variability [29], [30], [31]. Indeed, from PPG signal equivalent indices can be obtained, such as heart rate, together with other indices, whose surrogacy is currently under study, such as heart rate variability assessed with the PPG signal compared to the ECG. Other examples include the detection of blood oxygen saturation levels, evaluated again using PPG technique, providing SpO_2 levels (pulsoxymetrically measured oxygen saturation) as an alternative to SaO_2 (arterial oxygen saturation), as well as the respiration rate, that can be obtained using chest bands as an alternative to flow sensors, which require the use of nasal tubes [19], [30], [32], [33].

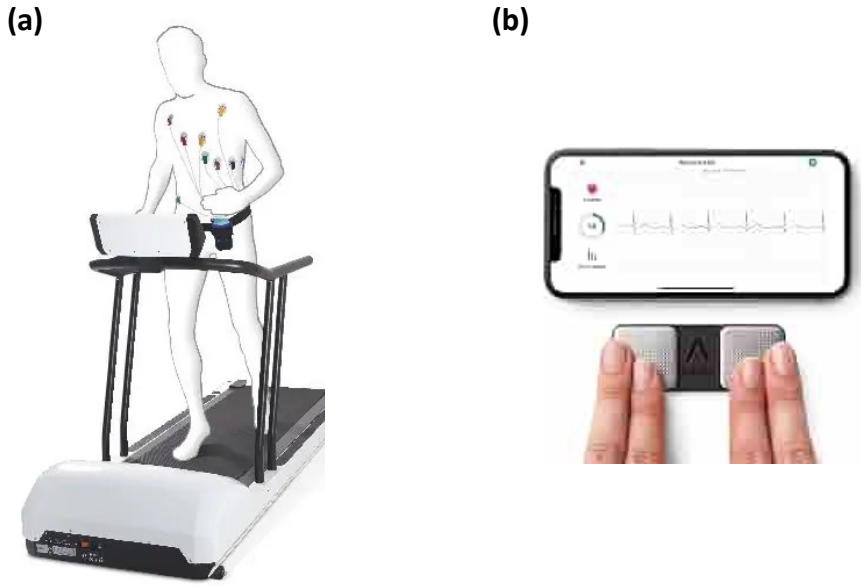

Figure 1.2 *– Pervasive versus non-invasive measurement of the ECG track. (**a**) Representation of the standard acquisition of the ECG trace with a holter: electrodes are attached to the body using adhesives, and the signal reaches the device through numerous bulky cables, causing discomfort to the user. (**b**)Acquisition of the same signal using a portable biomedical solution, produced by AliveCor, through compact and user-friendly hand-held device.*

Besides, equally important is the need to make biomedical devices used in healthcare not only performant and easy to use but also compact and comfortable, characteristics that would help reduce the pervasiveness of measurements.

For this reason, research and development of these technologies have led to the emergence of two main categories of devices aimed at addressing this need: portable biomedical devices and Wearable Health Devices (WHDs). The first ones are devices that exhibit higher performance in terms of the quantity of acquirable biosignals and measurement accuracy. Indeed, less stringent requirements in terms of weight and compactness allow for the integration of more complex components and biomedical sensors. Moreover, due to their portable nature, they typically deliver superior performance and sometimes there is the option to directly use line power, thus resolving power consumption issues. On the other hand, portable biomedical devices are mainly limited to scenarios involving measurements in conditions of most or total absence of movement, a circumstance that effectively imposes a constraint on the extensive integration of healthcare to the extent that it has been discussed here. It is precisely in this context where WHDs come in, which, despite their technical specifications being almost always smaller compared to portable devices, thanks to their feature of being comfortably worn without hindering user actions throughout their usage, offer a continuous health status monitoring solution.

1.3 WEARABLE HEALTH DEVICES: POTENTIAL AND CHALLENGES

WHDs have emerged as revolutionary tools in the realm of healthcare, seamlessly integrating technology into our daily lives to monitor and enhance well-being [34], [35]. These devices, worn on the body as accessories or integrated into clothing, leverage cutting-edge sensors and electronics to collect a wide quantity of physiological data, transforming the way individuals manage their health. The rise of WHDs aligns with the growing emphasis on preventive healthcare, offering continuous monitoring and early detection of potential health issues [36], [37]. These technologies were recently introduced into the biomedical landscape focused on the user-consumer market with the initial goal of providing users with a qualitative insight into their well-being during daily routines, and subsequently began to integrate progressively more advanced functions, ranging from fitness tracking to sophisticated health monitoring.

In Figure 1.3, the main categories of WHDs are illustrated with respect to the body area where they are worn and, consequently, where they act to assess individual functionalities.

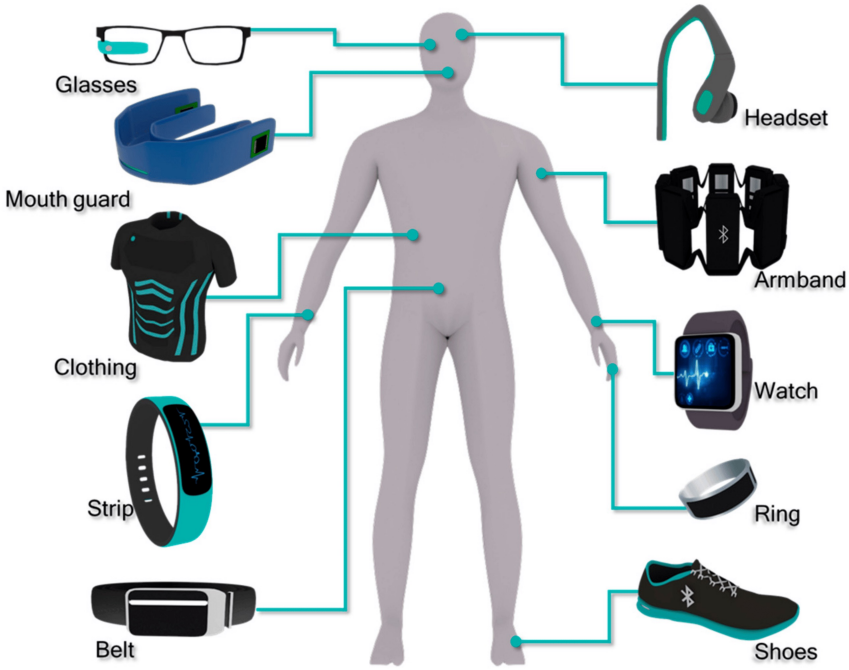

Figure 1.3 *– Types of commercialized wearable health devices and those currently in the research and development phase. It is noteworthy how the multitude of wearable devices, combined with the various body areas where they can be worn, promotes the multidistrict acquisition of multiple physiological parameters, contributing to a comprehensive and precise monitoring of the user's health status.*

Regardless of the type of device under consideration (e.g., t-shirt, glasses, wristband, etc.), they all share the integration of hi-tech components capable of performing the acquisition of biosignals comfortably and non-invasively, predominantly favoring biomedical sensors based on PPG signal acquisition and the use of electrodes for measuring biopotentials (such as ECG), as well as integrating inertial modules to track movement. Each of these devices boasts unique features, catering to different aspects of health and well-being. Indeed, they integrate an array of sensors, enabling users to track the main parameters of interest, such as physical activity and heart rate, also monitoring steps taken, sleep patterns, and providing insights into overall activity levels.

More advances models can go beyond that, by extracting vital parameters such as blood pressure (whose estimation methods are currently under investigation) and, at times, even recording entire ECG traces, thus transitioning from providing qualitative insight to becoming, in perspective, effective diagnostic tools capable of offering the user's clinical picture [37], [38].

Although each of these solutions has been specifically designed to acquire measurements in a particular body area, in last years we have witnessed a growing interest in wrist-worn and ring-shaped devices which, being much more versatile than others wearable solutions, they have become established in the market. Popular examples include smartwatch solutions, like the Apple Watch, Fitbit, Samsung Watch, and other even more compact and comfortable wearable technologies, such as ring-shaped devices like Oura Ring and Circul+. Table 1 lists and compares the main wrist-worn and ring-shaped devices available on the market, in terms of design, acquired biosignals, sampling rate, extracted features and computed physiological indices.

Table 1.1 *– Comparison of the main wearable wrist-worn and ring-shaped wearable devices available on the market in terms of design, recorded biosignals, features computed physiological indices and sampling rate [39], [40], [41], [42]*

Name	Type of device	Biosignals	Features and physiological indices	Sampling rate
Apple Watch	Wristband/smart watch	PPG, ECG, wrist temperature and motion	SpO_2 levels, HRV, sleep and physical activity tracking, fall recognition and atrial fibrillation detection	500 Hz
Galaxy Watch	Wristband/smart watch	PPG, ECG, wrist temperature and motion	SpO_2 levels, HR, sleep and physical activity tracking	25 Hz
Oura Ring	Ring	PPG, finger temperature and motion	SpO_2 levels, HRV, sleep and physical activity tracking, respiratory rate	250 Hz
Circul+	Ring	PPG, ECG, finger temperature and motion	SpO_2 levels, HRV, sleep and physical activity tracking, blood pressure	100 Hz

Thanks to technological advancements and the increasing interest in healthcare, the potential of WHDs is set to grow, extending well beyond personal health tracking. In fact, they also hold promise in clinical and industrial settings, respectively facilitating remote patient monitoring and improving healthcare delivery, and monitoring the health status of workers, contributing significantly to the emergence of Industry 4.0, Telemedicine and IoMT [7], [43], [44]. However, the massive integration of WHDs also presents challenges. Primarily, data privacy and security are paramount concerns, given the sensitive nature of health information [45], [46]. This issue actually involves the entire network of smart devices connected to the cloud, and that is why we are witnessing the emergence of numerous entities aiming to act as guardians of privacy, that promote research and development of new methods for a more reliable data encryption and, above all, encourage the updating of regulations in favor of data protection.

Ensuring the accuracy and reliability of the collected data is another hurdle that manufacturers must address to gain trust among users and healthcare professionals. In fact, the main limitation of wearable biomedical technologies concerns the loss of measurement accuracy under movement conditions [47], [48]. This is due to the fact that a significant portion of biomedical data is affected by motion artifacts, which degrade the signal, sometimes compromising the contained information and distorting the interpretation of extracted physiological indices. Furthermore, crucial importance lies in the selection of the most suitable data analysis algorithms for extracting relevant physiological indices. For this reason, current biomedical research is strongly focused on the research and development of data analysis algorithms capable of removing or at least reducing the effect of motion artifacts. Simultaneously, researchers are exploring the possibility of extracting advanced physiological indices that provide additional information, thus aiding WHDs in the pursuit of a comprehensive and accurate assessment of the user's health status.

1.4 DATA ANALYSIS FOR ASSESSING PHYSIOLOGICAL STATES

Once the challenge of acquiring physiological parameters non-invasively and comfortably is resolved through the use of WHDs, the issue shifts to the correct and unambiguous extraction of information contained in the recorded biosignals. After acquisition, the signals undergo processing using suitable filtering techniques to isolate the frequency band of interest, varying depending on the considered signal, from noise, which is eliminated by the employed filter. Subsequently, time series are usually obtained, and algorithms are applied to extract the corresponding physiological information, primarily obtaining indices in the time domain, such as heart rate in the case of the ECG track and pulse rate, its surrogate, in the case of the PPG signal [49], [50], [51], [52] and performing what is well known as Heart Rate Variability (HRV) Analysis. Metrics in the time domain are considered the most important, as they are standard in clinical settings and are more straightforward to interpret. Advanced metrics, leveraging more complex algorithms, enable the observation of behaviors not deducible from standard indices alone. Consequently, there is a growing interest in identifying additional metrics that extract supplementary information from the same signal, sometimes allowing the detection of functionalities of systems other than the one originating the examined biosignal. This expansion has broadened the scenarios of biomedical data analysis towards additional domains, such as the frequency and information theoretical domains, the latter capable of obtaining crucial insights into the dynamics and regularity of time series and the systems from which they derive [53], [54], [55], [56]. Typically, time series are extracted over acquisition windows ranging from Long-Term (LT, > 24 hours) to Short-Term (ST, approximately 5 minutes) duration, depending on usage scenarios, to perform HRV analysis and understanding, among all, cardiovascular and ANS funcionalities. However, not all applications can accommodate acquisition scenarios falling within long-term and, at times, even short-term durations. This drives research towards investigating new algorithms enabling the extraction of physiological indices over significantly shorter time windows, performing what is termed Ultra-Short-Term (UST) HRV Analysis, entailing the analysis of time series over windows shorter than 5 minutes [57], [58]. From the foregoing discussion, it becomes evident that continued research in both hardware and software aspects is crucial. Only a robust synergy between cutting-edge biomedical devices and efficient data analysis algorithms would be of fundamental importance to establishing WHDs as clinical tools supportive of healthcare.

CHAPTER 2

BACKGROUND & METHODS

2.1 NOTEWORTHY BIOSIGNALS FOR THE NON-INVASIVE EVALUATION OF HEALTH STATUS

In order to develop a wearable biomedical device for the assessment of user physiological states, as well as the investigation into the use of methodologies and techniques for biomedical data analysis, an in-depth study was conducted to identify key bio-signals that can be non-invasively acquired and provide important health-related information [59], [60], [61]. This study identified the fingers as the body district that best met the specifications of such a device, namely compactness, comfort, and multiparametric measurement capabilities, leading to the idea of creating a ring-shaped wearable device which is capable of acquiring biosignals that allow the assessment of cardiovascular, respiratory, and ANS functions.

Cardiovascular system functions are evaluated through the acquisition of ECG and PPG signals, which are among the most clinically important bio-signals. They allow obtaining crucial information about cardiac dynamics by analyzing both the temporal distance between successive peaks and the morphology of the two signals. Additionally, the synchronous acquisition of both signals enables the extraction of advanced indices, such as Pulse Arrival Time (PAT), providing information about the vascular system, detecting situations of arterial stiffness, and even estimating blood pressure (BP) with advanced techniques [16], [30], [62]. Finally, the PPG signal also provides information about the respiratory system, allowing to obtain information about SpO2 levels and, if appropriately filtered, respiration rate [19], [33].

In the second instance, there is the possibility of acquiring the SC signal. This signal tracks the sweat of the epidermal tissue, and the fingers are the body district where its variations can be significantly appreciated [63], [64]. It can provide important information about the occurrence of stressful events, aiding in understanding changes in the dynamics of signals coming from the cardiovascular system.

Finally, it proved useful to include an inertial module to track user movement, providing information about the presence of physical activity and other involuntary movements [47], [52]. Below are the bio-signals addressed in this work, discussing their nature, how they are extracted, and their use for biomedical analysis.

2.1.1 ELECTROCARDIOGRAPHY (ECG)

ECG is a gold standard diagnostic technique used in the field of cardiology to assess and monitor the electrical activity of the heart. This non-invasive procedure captures the electrical impulses generated by the heart muscle during each cardiac cycle. The resulting recording, commonly known as an ECG trace, provides a detailed representation of the heart's electrical behavior and is indispensable in diagnosing a wide range of cardiovascular conditions [65], [66].

Figure 2.1 shows the rapresentation of body districts from which to acquire the ECG signal, together with the ECG trace. The process of the ECG acquisition involves attaching electrodes to specific locations on the body, typically on the limbs, known as peripheral leads and chest, called precordial leads. The peripheral leads include the standard Lead I, Lead II, and Lead III, which record the voltage differences between different limb pairs. The precordial leads, on the other hand, are positioned across the chest to provide a more detailed view of the heart's activity from different angles, offering insights into specific regions of the cardiac muscle [67], [68].

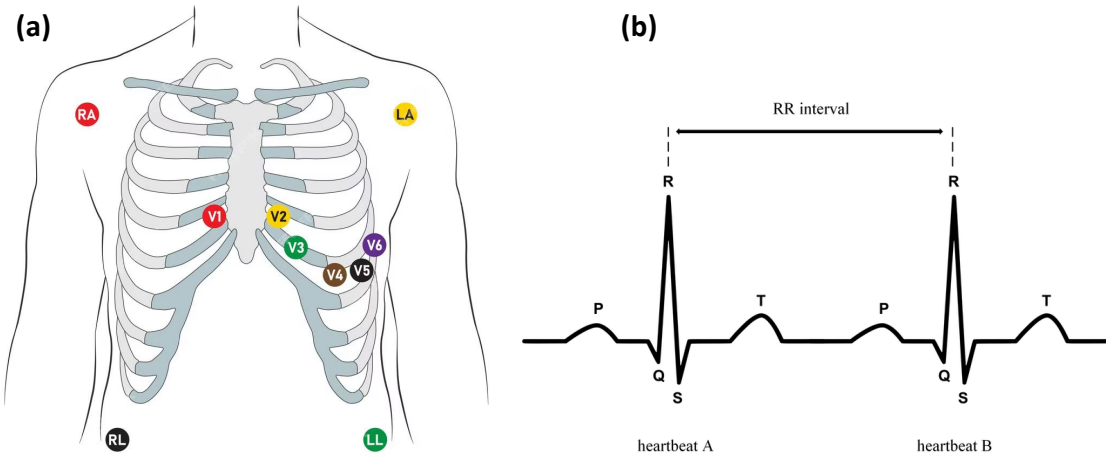

Figure 2.1 *– **(a)** Representation of the positions of the ECG electrodes for extracting peripheral (RA, LA, RL, and LL) and precordial derivations (V1 to V6). **(b)** ECG trace with identification of the P, T waves, and the QRS complex.*

The ECG trace consists of various waves, with the most prominent being the P wave, QRS complex, and T wave [69]. The P wave represents atrial depolarization, the QRS complex describes ventricular depolarization, and the T wave corresponds to ventricular repolarization. Analyzing the morphology and temporal distances between these waves provides valuable insights into the heart's functionality. In fact, the QRS complex's duration and shape can indicate issues such as arrhythmias or conduction abnormalities. Changes in the ST segment may suggest myocardial infarction, while variations in the T wave can provide information about electrolyte imbalances [70], [71]. Among the various types of analyses applicable to the characteristics of the ECG trace, one of the most important is related to the temporal distances between successive R peaks. Indeed, the R peak is the key identifier of the cardiac beat, and from the RR time series, it is possible to study what is commonly referred to in literature as Heart Rate Variability (HRV), which is extensively employed in this study and will be further detailed in the subsequent sections [49].

While having access to all leads of the ECG trace allows for a comprehensive view of the propagation of the electrical signal, recording such information would be overly pervasive and somewhat challenging for a wearable device. On the other hand, peripheral acquisition of the ECG trace still enables the visualization of the typical morphology and accurate extraction of the distances between successive R peaks [41], [72], [73], [74], [75]. For this reason, the developed device incorporates a mechanism to perform the first of the three peripheral ECG leads, considering the right and left fingers as the points of electrode application.

As well-established in the literature, this lead can be obtained by employing the physiological principle of Einthoven's Triangle, shown in Figure 2.2, which involves recording the electrical potential differences in specific body regions generated by the heart during the cardiac cycle. Specifically, these potential differences are detected by applying three electrodes at the vertices of an equilateral triangle drawn in the thoracic region of the human body, with one vertex facing downward. The ECG recorded from these three leads represents the sum of electrical signals from the heart according to the spatial orientation of the triangle, allowing for the analysis of the direction and intensity of the electric current flow through the heart.

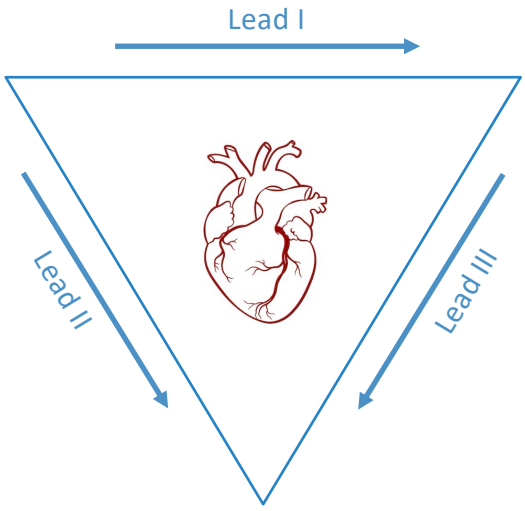

Figure 2.2 *– Einthoven's Triangle drawn around the heart. Electrodes applied to the vertices of the triangle allow for the detection of the electric field generating from the cardiac muscle by evaluating lead I, lead II, and lead III, which correspond to the sides of the triangle.*

2.1.2 PHOTOPLETHYSMOGRAPHY (PPG)

Although the ECG is the most relevant clinical signal for assessing cardiac health, the pervasive measurement methodology entails a non-negligible level of discomfort for the user. Moreover, there is the need to obtain information about the functions of the vascular system, which is crucial to complete the assessment of cardiovascular health. Therefore, most wearable biomedical devices exploit PPG, an easy to apply, inexpensive and non-invasive optical technique, which is able to detect blood volume changes in the peripheral vessels at different body locations [76].

Figure 2.3 illustrates an example of the acquisition technique in reflection mode and the typical waveform of the PPG signal. The working principle of PPG is based on the fact that blood has a different light absorption coefficient compared to the surrounding tissues. In particular, the simplest PPG device is composed of a single light emitting diode (LED) illuminating the body district of interest through the emission of light at a specific wavelength, typically between 530 nm and 940 nm, and of a photodetector capturing reflected or transmitted light (Figure 2.3a).

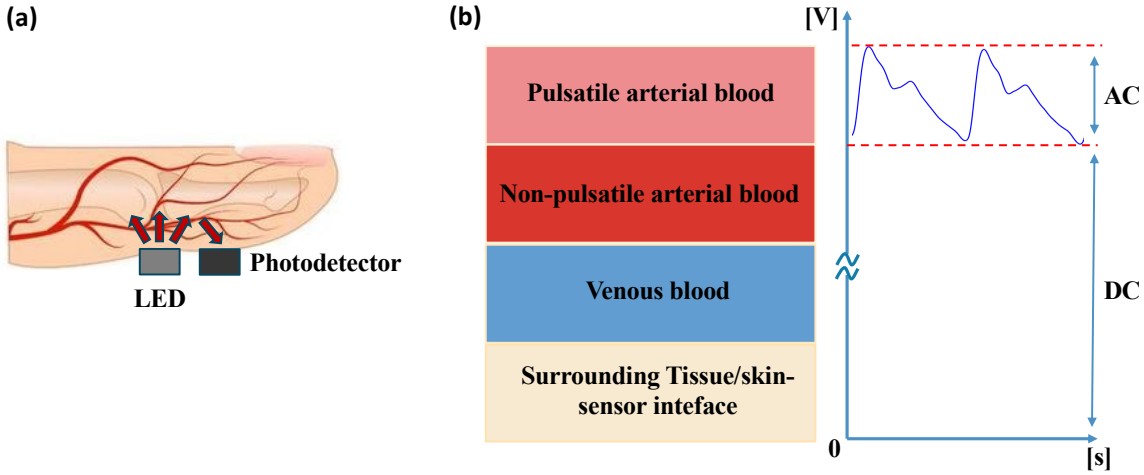

Figure 2.3 *– **(a)** Reflection mode PPG technique for the acquisition of the fingertip sphygmic waveform. **(b)** Path of the emitted light through the tissues that leads to the acquisition of both the pulsatile (AC) and non-pulsatile (DC) components that characterize the PPG signal.*

As shown in Figure 2.3b, a typical PPG signal acquired by a photodetector can be decomposed in both AC and DC components. The first one represents the pulsatile component of the PPG waveform, which contains information related to instantaneous volume changes in blood vessels of a given body location and can be considered as a function of the cardiac cycle. In particular, it is a periodic waveform with a fundamental frequency, depending on the heart rate, at around 1 Hz and consists in a rising trend followed by a falling one, respectively related to the systolic and diastolic phases of the cardiac cycle. In high-resolution acquisition systems it is even possible to detect a particular change in the pulsatile component between the systolic and diastolic phases, known as dicrotic notch, which has been widely related to aortic valve closure.

The non-pulsatile component, which usually represents most of the total amplitude of the PPG signal, is instead mainly due to the presence of other tissues layers between the LED-photodetector interface, such as skin, veins and bias blood volume inside the arteries, which involve a constant absorption of the light beam, resulting in a continuous component, so called DC component, constantly detected by the photodetector [77]. This component is subject to significant variations in the presence of ambient light and motion artifacts, sometimes degrading the pulsatile component of the PPG signal to the point of compromising its interpretation entirely. For this reason, modern integrated PPG sensors incorporate sophisticated DC component removal circuits, along with the ability to use inertial sensors for the detection and removal of motion artifacts [47], [78].

Lastly, since AC component is proportional to the change in blood vessels volume given by the cardiac cycle, it can be employed for extracting important cardiovascular parameters such as oxygenation, heart rate and its variability, blood pressure estimation, pulse transit time, pulse wave velocity and pulse to pulse interval [79], [80]. Recent works have, indeed, demonstrated that PPG signal can be employed as a surrogate of ECG to perform heart rate variability analysis, given the high degree of similarity with the indices extracted from ECG R-R intervals [31], [81], [82].

2.1.3 SKIN CONDUCTANCE (SC)

Another important biosignal that can be acquired in a simple and non-invasive manner is the skin conductance (SC), defined as the conductance exhibited by the epidermal tissue [51]. It is a signal that, under resting conditions, typically stabilizes at a constant and characteristic value for each individual, and it is subject to slow variation over time. However, it could undergo abrupt variations in response to stressful events, and for this reason it is interesting to study the variations and response of this signal over time, which is why it is referred to as Galvanic Skin Response (GSR) [83]. In fact, it reflects autonomic changes in the electrical properties of the skin due to the activity of the sweat glands, each one innervated by several sudomotor fibers [84], [85]. Specifically, this signal reflects the fact that the human organism reacts to a stressful event, either mental or physical, by activating the sympathetic nervous system (SNS), which produces sweating in several body districts, including the fingers. This defense mechanism is also known as general adaptation syndrome (GAS) and produces sudden changes in different physiological parameters (e.g., increased HR, blood pressure and sweating). Such changes are due to both sympathetic and parasympathetic (PNS) branches of the ANS, intervening to prepare the individual to react and overcome the stressor.

Figure 2.4 shows an example of SC acquisition on the fingers, along with the typical trends of the same signal acquired on different body districts. In the literature, measurements of SC are reported in very different body districts, and there is no true standard [63]. Instead, it is recommended to identify areas of the body with a higher concentration of sweat glands, such as the fingers [51].

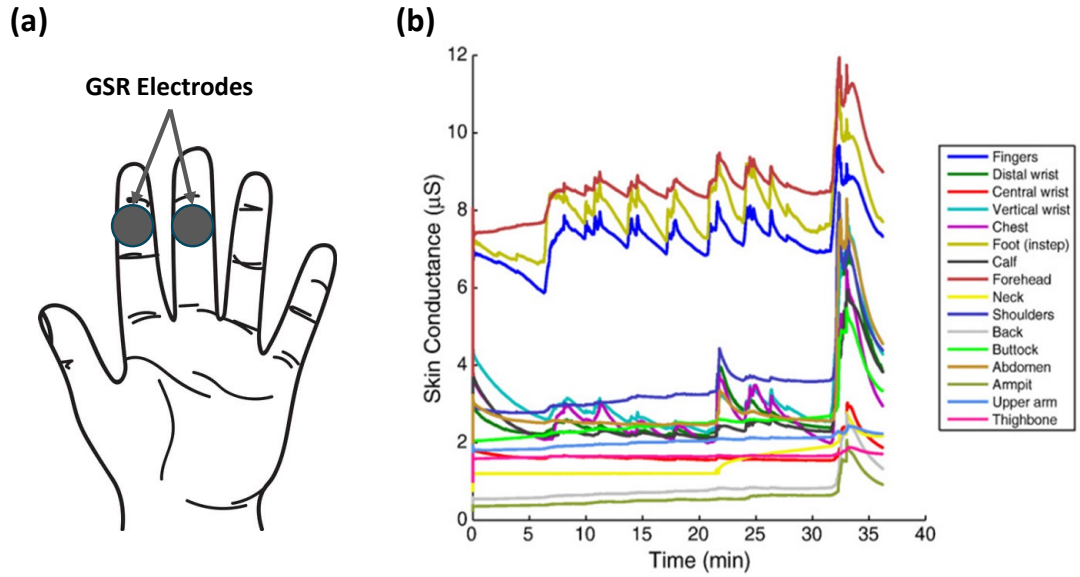

Figure 2.4 *– **(a)** Illustration of the electrode placement for acquiring GSR signals on index and middle fingers. **(b)** Skin conductance trends measured on different body districts.*

Moreover, the extremities of the limbs are involved in response to stressful events, both physical and emotional, through the phenomenon of Raynaud, which involves the sudden narrowing of blood vessels followed by a decrease in temperature and an increase in sweating [86]. Therefore, the possibility of acquiring SC directly on the fingers would allow for the discrimination of the presence of stressful phenomena, contributing to a correct interpretation of cardiovascular parameters as well as the user's health status.

The working principle of the skin conductance measure relies on the volt-amperometric method to obtain skin resistance measurements. Two electrodes are applied on a body area, such as the phalanges of the fingers, characterized by a high concentration of skin sweat glands; by applying an electric potential to the first electrode and detecting the residual potential, knowing the current flowing in the electrodes, it is possible to obtain the value of the resistance offered by the epidermal tissue [64], [87]. In this study, with the aim of conducting SC measurements using the developed wearable ring-shaped device, SC measurements were initially taken on middle and index fingers of the hand to establish reference values for comparison with those obtained on the same finger. Through subsequent prototypes, the capability was achieved to perform SC measurements considering two diametrically opposed zones of the forefinger, thus leveraging the ring-shaped form of the device and simultaneously obtaining results equivalent to those obtained from measurements on two different fingers.

While many literature works have demonstrated that stress can be properly estimated using only HRV [49], [88], [89], recent studies evidenced that GSR can be considered an excellent real-time correlation of stress, being linearly related to arousal [90], [91], [92]. Indeed, the GSR can be decomposed into two components, namely skin conductance level (SCL) and skin conductance response (SCR), which respectively provide information on the baseline level of SC (when the subject is at resting conditions) and stress levels, with SCR being more closely related to the activation of the SNS. Some researchers regard GSR as the foremost real-time indicator of stress, even superseding HRV measures, or suggest combining GSR as a measure of SNS activity and the high frequency HRV spectral component as a measure of PNS activity [93]. Therefore, stress detection accuracy can be enhanced through a multimodal approach that utilizes machine learning techniques to classify stress conditions based on a combination of both HRV and GSR indices, instead of relying solely on HRV measures [94], [95].

2.1.4 MEASURES OF MOTION

In WHDs context, understanding and quantifying physical activity are integral components for a comprehensive health assessment. Measures of motion play a pivotal role in capturing the dynamics of a user's movements, providing valuable insights into their daily activity levels [96], [97].

Gyroscopes, key components in these devices, measure rotational motion with precision. They function by detecting changes in orientation and angular velocity, expressed in degrees per second, in the space, allowing the device to determine the direction and speed of movement in the three directions, namely as G_x, G_y and G_z, as shown in Fig.2.5. The gyroscopic data contribute significantly to recognizing activities that involve rotation, such as turning, twisting, or any other motion involving changes in orientation. This information is vital for assessing the diversity of physical activities and understanding how the body moves in three-dimensional space. On the other hand, accelerometers are crucial for capturing linear acceleration along the three axes, respectively called as A_x, A_y and A_z.

These sensors enable the device to measure changes in velocity and direction, offering a comprehensive view of both rapid and gradual movements. The x-axis typically represents lateral movements, the y-axis captures vertical displacements, and the z-axis accounts for forward or backward motions. Through the combined data from accelerometers, wearable devices can track an individual's posture, detect changes in position, and quantify the intensity and duration of physical activities, thus enabling the detection of falls.

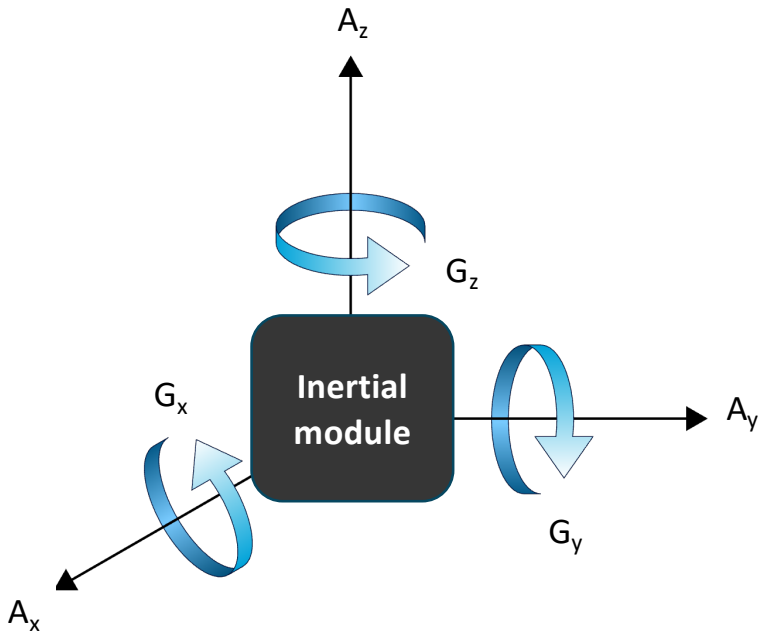

Figure 2.5 *– Spatial measurements in three axes performed by a generic inertial sensor in terms of gyroscope (G_x, G_y and G_z) and accelerometer (A_x, A_y and A_z) readings.*

Moreover, the ability to track body movement, as well as the wearable device itself, could be crucial for investigating the presence of motion artifacts, as algorithms could be implemented to reduce and eliminate such artifacts [98], [99], [100], [101]. Finally, detecting even low-intensity involuntary movements would enable the recording of any tremors that could reveal pathological conditions, thus aiding in the early diagnosis of diseases affecting the nervous system [52], [102].

2.2 DATA ANALYSIS: METHODS AND TECHNIQUES

Once the physiological signals to be used for detecting physiological states are identified and selected, the next step is to determine data analysis methodologies, each specific to the respective signals, capable of adequately extracting the physiological information they contain.

Below are the main data analysis techniques for extracting useful physiological indices from ECG, PPG, and SC signals. In particular, for the first two signals, data analyses based on RR and PP time series have been considered, respectively extracted by considering the temporal distance between two successive R peaks for the ECG signal and the peak of the photoplethymographic wave for the PPG signal. This allows the same data analysis methodology (i.e., HRV) to be applied to both time series. Although the term Pulse Rate Variability (PRV) is more suitable for the PPG signal, the type of analysis and implementable algorithms are the same. Therefore, the following paragraph will introduce HRV metrics that are applicable to both signals.

Similarly, methodologies for the correct interpretation of the SC signal will be discussed. Finally, techniques for extracting the two main parameters of the respiratory system, namely SpO_2 levels and respiration rate, directly from the PPG signal, are presented.

2.2.1 HEART RATE VARIABILITY METRICS

HRV is usually studied through the monitoring of ECG recordings, extracting the time series of R–R intervals (i.e., the time periods between successive heartbeats) [49]. In clinical settings, the use of 24 h recordings (i.e., LT analysis) is considered the “gold standard” for the investigation of cardiovascular control mechanisms, since such timeframe allows a better description of the physiological processes, taking into account slower temporal fluctuations (e.g., the circadian rhythms) and the response of the organism to a wider range of external stimuli [103]. On the other hand, ST measurements are typically based on 5 min recordings and have been more extensively employed for practical purposes, especially for assessing the balance between SNS and PNS activities, given that fluctuations mediated by ANS, reflecting respiratory, baroreflex and vascular tone regulatory mechanisms overlap to generate short-term dynamics and, finally, they are suitable for the study of autonomic tone. [31], [49], [103], [104], [105].

ST HRV is commonly investigated through different time-, frequency- and information-theoretic domain indexes computed starting from ECG R-R interval time series. Specifically, time–domain indexes are used to quantify both average heart rhythm and the extent of beat-to-beat variability [49], [106], while frequency–domain indexes extract information specific to various time scales of oscillations. Furthermore, more recently developed entropy-based measures permit the assessment of the regularity and complexity of cardiovascular dynamics [56], [107], [108], [109], [110]. ST HRV analysis has also been proven useful outside clinical settings, e.g., to monitor health and wellbeing at home and in everyday life scenarios using wearable technologies [34], [111], [112], [113].

With the widespread adoption of WHDs, especially in domestic settings (e.g., smart-healthcare), research now focuses on whether, and to what extent, shorter recordings can be exploited for cardiovascular variability analysis, given their lower computational and memory resources, in order to quickly extract useful physiological indexes [34], [36], [111], [114]. Several works have recently investigated on the so-called UST HRV analysis, which exploits recordings shorter than 5 min, comparing the results with those obtained using the ST standard [57], [115], [116], [117], [118], [119]. However, the choice of the time series length strongly influences the physiological indices derived from RR time series, in such a way that employing shorter recordings reduces the ability to resolve slower oscillations within the analyzed cardiovascular dynamics [106], [120]. Generally, at least 2 min recordings are recommended to observe Low-Frequency (LF, range: 0.04–0.15 Hz) dynamics, related especially to SNS, but also to PNS activity, and at least 1 min to observe High-Frequency (HF, range: 0.15–0.4 Hz) dynamics, mainly related to parasympathetic activity fluctuations associated with respiration [49], [106]. Longer recordings, i.e., 24 h period LT analysis, further allow detection of lower frequency components, such as the very-low-frequency (VLF, 0.0033–0.04 Hz) and the ultra-low-frequency (ULF, <0.003 Hz). Therefore, the use of recordings shorter than 5 min may result in a loss of information related to slower dynamics if compared to ST analysis. The reliability of the cardiovascular parameters computed from UST recordings also depends on the acquisition protocol and on the dynamics of the response mechanisms to the task or stimulus [120].

On the other hand, the possibility of performing UST analysis would provide significant advantages such as simplicity of acquisition for biomedical devices (especially wearables), reduced data storage requirements, better immunity to motion artifacts (i.e., higher chances of extracting artifact-free acquisition windows, as they would be of short duration), greater potential to obtain stationary windows, which are crucial for implementing algorithms in the information domain that require process stationarity. In this sense, the use of validated and widely employed protocols used in HRV analysis could be envisaged, e.g., the passive head-up tilt test to evoke orthostatic stress, that are able to study cardiovascular autonomic responses [121], [122].

2.2.1.1 TIME DOMAIN

In this work, HRV time domain analysis was performed on RR time series computing the average and the standard deviation of the series values, thus obtaining the two main indices in the time domain, which are respectively the temporal distance between two beats, from which the heart rate can be derived, and the standard deviation of the interbeat intervals between normal sinus beats (SDNN) [49]. Lastly, the root mean square of successive differences (RMSSD) was computed as follows to extract information about the beat-to-beat changes in heart rate mediated mostly by PNS [31], [49], [123]:

$$RMSSD = \sqrt{\left(\frac{1}{N-1}\right)\sum_{n=1}^{N-1}\left(x(n+1)-x(n)\right)^2} \quad (1)$$

being *x(n)* the *n*-th RR samples and *N* the time series length.

The use of all three physiological indices is very useful for evaluating not only the functions of the cardiovascular system but also the levels of activation of the ANS. Indeed, analyzing heart rate values over time provides information about the subject's physiological state, allowing the discrimination of unnatural states, such as the presence of an accelerated heartbeat (i.e., tachycardia) or an excessively slow heartbeat (i.e., bradycardia). Furthermore, a lower heart rate often signifies a dominant parasympathetic influence, suggesting a state of relaxation and minimal stress, while a higher heart rate may indicate increased sympathetic activity associated with heightened stress, physical exertion, or other physiological demands.

The same concept can be extended to SDNN and RMSSD, which provide crucial insights into the autonomic balance shaping heart rate dynamics. Specifically, SDNN, reflecting overall heart rate variability, provides a comprehensive view of the dynamic equilibrium between sympathetic and parasympathetic influences. Higher SDNN values suggest a more adaptable autonomic nervous system, capable of responding effectively to stressors and promoting cardiovascular resilience. RMSSD, on the other hand, specifically focuses on parasympathetic modulation with higher values associated with increased vagal tone, promoting a relaxed state and efficient recovery.

2.2.1.2 FREQUENCY DOMAIN

Frequency domain analysis allows to estimate the power spectrum of the time series into different frequency bands of physiological interest [49], [124]. Among the physiological indices extracted by performing HRV in the frequency domain, the most noteworthy are the low-frequency (LF) and high-frequency (HF), from which the LF/HF ratio can be derived.

In order to perform frequency analysis of time series, among the various methods, the Blackman-Tukey approach has been employed. This approach is a non-parametric method that allows for the estimation of power spectral density based on the computation of the fast Fourier transform (FFT) of the windowed autocovariance function. Specifically, a FFT of 512 points is performed on the windowed autocovariance function of the data, which is windowed using the Parzen window, which helps to reduce the spectral leakage of the spectral window (i.e., the FFT of the covariance lag window). The use of a windowing function, such as the Parzen window, ensures that the expected value of the spectral estimate coincides with the result of the convolution between the spectrum of the window and the true spectrum of the data. Consequently, in order to obtain a resolved estimate of the power spectral density, it is necessary to appropriately choose the truncation point M of the corresponding lag window, taking into account the bandwidth Bw of the spectral window, which, for the Parzen window, can be obtained considering the following equation:

$$Bw = \frac{1{,}273 \cdot F_S}{M} \tag{2}$$

where F_s is the sampling frequency of the signal under examination.

If the raw signal has undergone resampling, F_s represents the sampling frequency of the signal. Otherwise, F_s is defined as the inverse of the average time series (e.g., RR interval or PP interval) duration.

The LF band is primarily linked to the combined influence of sympathetic and parasympathetic activity, reflecting the modulation of heart rate by both branches of the autonomic nervous system. It is often considered an indicator of sympathetic modulation, particularly during conditions of stress or increased sympathetic activation. On the other hand, the HF band is largely influenced by parasympathetic (vagal) activity. This band reflects the respiratory sinus arrhythmia, the heart rate variability synchronized with the respiratory cycle. Increased HF power is generally associated with enhanced parasympathetic modulation, indicating a state of relaxation and recovery. Lastly, the balance between LF and HF components is crucial for understanding autonomic regulation, which is why typically, once the two indices are calculated, there is an interest in knowing their ratio. For instance, a higher LF/HF ratio may suggest increased sympathetic dominance, indicating a stress response, while a lower ratio could indicate parasympathetic dominance, signifying a more relaxed physiological state.

2.2.1.3 INFORMATION DOMAIN

Information theoretical measures, in their most general form, analyze the joint dynamics and interactions between multiple time series, allowing for the identification of connections between the values of these series and their variations. In this work, we have limited ourselves to studying the dynamics of a single series (i.e., RR, PP), by performing information-theoretic analysis to quantify the information carried by the physiological time series under examination, as well as their complexity. The latter is typically quantified as the unpredictability of the present sample given its past samples, and thus has been associated to the inverse of the regularity of the time series [110], [125].

The static entropy (SE), dynamic entropy (DE), and conditional entropy (CE) measures have been computed on RR and PP time series using both a parametric and a model-free estimation. Starting from a stationary stochastic process X, we can denote as $x = \{x_1, x_2, \dots, x_N\}$ the time series of length N, taken as a realization of the process X, as X_n is the variable obtained by sampling the process X at the present time n, and $X_n^m = [X_{n-1}, \dots, X_{n-m}]$ the variable describing the collection of the past m states.

Using such notation, the static entropy quantifies the "static" information contained in the current state of the process X, without considering its temporal dynamics, and can be defined as [126]:

$$SE = H(X_n) = -E[\log p(x_n)] \quad (3)$$

where $E[\cdot]$ is the expectation operator and $p(\cdot)$ the probability density, while $H[\cdot]$ denotes the entropy. The dynamic entropy (DE) instead represents the "joint" entropy of the present and past variables comprising the process; therefore, it provides the amount of information provided by the current sample of the series and by its past samples as well, thus providing "dynamic" information on the entire process. This can be defined as [127]:

$$DE = H(X_n, X_n^m) = -E[\log p(x_n, x_{n-1}, \dots, x_{n-m})] \quad (4)$$

where $H(\cdot,\cdot)$ is the joint entropy of two random variables. Then, the conditional entropy (CE) quantifies the average uncertainty that remains about the present state of the process when its past states are known (i.e., the new information contained in the current sample that cannot be inferred from the past history), and is defined as [126]:

$$CE = H(X_n|X_n^m) = H(X_n, X_n^m) - H(X_n^m) = -E[\log p(x_n|x_{n-1}, x_{n-2}, \dots, x_{n-m})] \quad (5)$$

where $H(\cdot \mid \cdot)$ denotes conditional entropy operator.

The computation of SE, DE, and CE indices was carried out through two different estimation approaches, in order to identify which method allows the best trade-off between computational costs and ability to discriminate among physiological changes (i.e., rest versus stress).

The first estimation method (hereinafter referred as *lin*) consists of a linear parametric approach based on the assumption that the observed process X is a stationary Gaussian process [126], which is a reasonable assumption given that many physiological data tend to follow a Gaussian distribution. Under this assumption, the above-mentioned entropies measures can be computed, after describing the dynamics of the process X with a linear regression model, from the covariance matrices of the variables sampling the process. In particular, the present and past variables of the process are related with the autoregressive (AR) model $X_n = A \cdot X_n^m + U_n$, where A is a vector of m regression coefficients and U is a white noise process modeling the prediction error.

AR model identification has been performed via ordinary least squares method [128] to obtain estimations of regression parameters and prediction error variance, thus estimating the variance and the covariance matrices of the process. Then, denoting as $\hat{\sigma}_X^2$ the variance of the process, as $\hat{\Sigma}_{X_n \boldsymbol{X}_n^m}$ the covariance matrix of the present and past states of X, and as $\hat{\sigma}_U^2$ the predicton error variance, the above defined entropy measured can be computed as [127]:

$$SE_{lin} = \frac{1}{2}\ln(2\pi e\hat{\sigma}_X^2) \tag{6}$$

$$DE_{lin} = \frac{1}{2}\ln\left((2\pi e)^{m+1}\left|\hat{\Sigma}_{X_n \boldsymbol{X}_n^m}\right|\right) \tag{7}$$

$$CE_{lin} = \frac{1}{2}\ln(2\pi e\hat{\sigma}_U^2) \tag{8}$$

where *e* is the Euler's number.

The second estimation method (hereinafter referred as *knn*) is a model-free approach based on nearest neighbor metrics, which exploits the intuitive notion that the local probability density around a given data point is inversely related to the distance between the point and its neighbors.

Using this approach, estimates of SE, DE and CE of the process X can be respectively computed through the following expressions [126], [127]:

$$SE_{knn} = \psi(N) + \langle \log \epsilon_{n,k} - \psi\left(N_{X_n} + 1\right)\rangle \tag{9}$$

$$DE_{lin} = \frac{1}{2}\ln\left((2\pi e)^{m+1}\left|\hat{\Sigma}_{X_n \boldsymbol{X}_n^m}\right|\right) \tag{10}$$

$$CE_{knn} = -\psi(k) + \langle \log \epsilon_{n,k} + \psi\left(N_{X_n^m} + 1\right)\rangle \tag{11}$$

where $\psi(\cdot)$ is the digamma function, *k* is the number of neighbors chosen for the analysis, $\epsilon_{n,k}$ represents twice the distance between the *n*-th realization of (X_n, X_n^m) and its *k*-th nearest neighbor, N_{X_n} and $N_{X_n^m}$, represent respectively the number of points with a distance from x_n and x_n^m smaller than $\frac{\epsilon_{n,k}}{2}$, and $\langle\cdot\rangle$ is the average operator; the average is taken over all the $N - m$ realization of the patterns (X_n, X_n^m) that can be extracted from a series of length *N*. Here, estimation of the SE and CE has been performed exploiting the distance projection method for bias compensation described in [126], [127].

Lastly, the number of neighbors chosen for the model-free estimator was $k = 10$, while the number of past components considered for the time series past histories was set equal to 2. Similarly, the order of the autoregressive model defined using standard least-squares regression for the *lin* approach was set to $m = 2$.

2.2.1.4 GRANGER CAUSALITY MEASURES

The methods and measures considered and discussed so far pertain to the domain of univariate data analysis, as they are types of data analysis aimed at extracting physiological information contained within a single process (i.e., biosignal or time series). In this paragraph, an additional measure is introduced that allows for expanding the scope of data analysis into the realm of multivariate analysis, specifically introducing Granger Causality measures to exploit the potential of the synchronous multiparametric acquisition.

Multivariate analysis refers to the statistical examination of multiple variables simultaneously to understand the relationships and patterns among them. In the context of biomedical signal processing, acquiring multiple biosignals offers a wealth of information about physiological processes. Conducting multivariate analysis becomes crucial in deciphering the intricate relationships between these signals and how they may influence each other. For instance, by simultaneously measuring ECG, PPG, and respiratory signals, it is possible to explore how changes in one signal/process may correlate with or drive changes in another one. Specifically, the driver process refers to a biosignal that influences or drives changes in another signal, known as the target process. Identifying these driver-target relationships is essential for unraveling the complex interactions between different physiological systems.

One quantitative measure commonly used to assess causality between biosignals is the Granger Causality measure, which evaluates the extent to which the past values of one signal can predict the future values of another signal, beyond what can be predicted by their own past values. In the context of biosignal analysis, Granger Causality provides insights into the directional influence between two signals, helping to elucidate causal relationships and uncover underlying physiological mechanisms.

In mathematical terms, it is possible to consider two processes Y_1 and Y_2, representing respectively the target process and the driver process. Considering the use of an autoregressive (AR) model, each pair of stationarity zero-mean Y_1 and $Y_2$and series form the bivariate process $\boldsymbol{Y}(n)$ which can be defined as [129]:

$$\boldsymbol{Y}(n) = \sum_{k=0}^{p} \boldsymbol{B}(k)\boldsymbol{Y}(n-k) + U(n) \tag{12}$$

where p is the model order and $\boldsymbol{Y}(n) = [Y_1(n)\ Y_2(n)]^T$. The 2x2 coefficient matrix $\boldsymbol{B}(k)$ relates the present with the past of the processes assessed at lag k, the latter taking the value 0 as well to bring instantaneous effects from $Y_2(n)$ to $Y_1(n)$ into the model in the form of the coefficient $b_{12}(0)$ of the matrix $\boldsymbol{B}(0)$. The vector $\boldsymbol{U}(n) = [U_1(n)\ U_2(n)]^T$ contains zero-mean uncorrelated white noises, with diagonal covariance matrix $\boldsymbol{\Sigma} = E[\boldsymbol{U}(n)U^T(n)] = diag\{\sigma_{ii}^2\}, i = 1{,}2$. While the full AR model in the previous equations provides a global representation of the bivariate process, to describe the individual dynamics of the target process Y_1, a reduced AR model involving only that process was formulated as:

$$Y_1(n) = \sum_{k=1}^{\infty} \tilde{a}_1(k)Y_1(n-k) + \tilde{U}_1(n) \tag{13}$$

where the coefficients $\tilde{a}_1(k)$ weight the past samples of the process $Y_1(n)$, and the innovation process $\tilde{U}_1(n)$ has variance $\tilde{\sigma}_{11}^2$. Note that to capture the full dynamical behavior of $Y_1(n)$ the order of the restricted AR process is infinite even when the original bivariate model has a finite order p [130]. The linear parametric formulation allows to compute the logarithmic measure of Granger Causality [131], [132] by comparing the variance of the residuals resulting from the two regressions:

$$F_{j\to i} = ln\left(\frac{\tilde{\sigma}_{ii}^2}{\sigma_{ii}^2}\right) \tag{14}$$

Moreover, from the full AR representation of the bivariate process, it is possible to represent the model coefficients in the Z domain through the Z-transform of the first equation, thus yielding $\boldsymbol{Y}(z) = \boldsymbol{H}(z)\boldsymbol{U}(z)$, where the 2x2 transfer matrix is computed as $\boldsymbol{H}(z) = [\boldsymbol{I} - \sum_{k=1}^{p} \boldsymbol{A}(k)z^{-k}]^{-1}$, being $\boldsymbol{I}$ the 2x2 identity matrix.

Computing $\boldsymbol{H}(z)$ on the unit circle in the complex plane, it is possible to derive the spectral density matrix of the bivariate process as $\boldsymbol{S}(\bar{f}) = \boldsymbol{H}(\bar{f})\boldsymbol{\Sigma}\boldsymbol{H}^{*}(\bar{f})$, where $\bar{f} \in [-0.5,0.5]$ is the normalized angular frequency $\bar{f} = f/f_s$, and * stands for the Hermitian transpose. This matrix contains the power spectral densities (PSDs) of the individual processes on the diagonal, and the cross PSDs between the two processes out of the diagonal. Moreover, a frequency-specific measure of Granger causality from Y_j to Y_i can be computed as [132]:

$$f_{j\to i}(\bar{f}) = ln\left(\frac{S_{ii}(\bar{f})}{\sigma_{ii}^2|H_{ii}(\bar{f})|^2}\right) \tag{15}$$

and interpreted as a measure of coupling strength, being 0 in the absence of directed coupling from Y_j to Y_i at the frequency $\bar{f}$, and increasing to infinite in the presence of full coupling. The integration the last equation alongside the whole frequency axis, with the Nyquist frequency in each spectral representation taken as $f_s/2 = 1/(2\langle HP\rangle)$, provides the correspondent time domain measure given in (14), i.e. we have $F_{j\to i} = 2\int_0^{1/2} f_{j\to i}(\bar{f})d\bar{f}$ [133].

2.2.2 GALVANIC SKIN RESPONSE: SCL AND SCR COMPONENTS

The GSR signal can be divided into two components: the skin conductance level (SCL) and the skin conductance response (SCR) [55], [83]. SCL is the measure of the basal level of the sweat glands activity (i.e., the sweating without stressors), which depends on the individual's physical characteristics, and is considered as a reference level to evaluate sweating variations. SCR (i.e., the phasic activity) is a highly variable signal that detects sudden changes of sweating following stressful events, reflecting a fast variation in the autonomic arousal. Acquiring a high-quality GSR signal allows for extracting the two components and thus an effective assessment of the activity of the SNS.

In this work, both SCL and SCR components were extracted employing the MATLAB-based toolbox LEDALAB; this software allowed us to separate the two components, exploiting the continuous decomposition analysis based on a standard deconvolution method [55]. Specifically, this method is based on the assumption that the activity of the sudomotor nerve causes peaks in SC with short time constants, which trigger SCR exhibiting larger time constants.

Consequently, deconvolution between SC data with an appropriate impulse response function (IRF) would allow for reversing this transformation and, therefore, obtaining an estimate of SCR amplitudes from SC values.

In mathematical terms, the sudomotor nerve activity is considered as a driver, which generates a sequence of mostly distinct impulses, that are the sudomotor nerve bursts, which trigger a specific impulse response (i.e., SCR). Therefore, the IRF describes the time course of this impulse response, which can be represented by the following equation:

$$SCR = Driver_{Phasic} * IRF \tag{16}$$

where the $(*)$ operator defines the convolution product.

SCL can also be equally represented as the convolution between the same IRF and a sort of tonic driver function, a circumstance that leads to the following equation:

$$SCL = Driver_{tonic} * IRF \tag{17}$$

Since the phasic activity was assumed to superimpose a slowly varying tonic activity (i.e., SCL), the whole SC activity thus can be assumed to be composed as:

$$SC = SCL + SCR = (Driver_{tonic} + Driver_{phasic}) * IRF \tag{18}$$

Finally, denoting as $(-)$ the deconvolution operator and applying it to the right member of the (13), it is possible to obtain the final equations:

$$\frac{SC}{IRF} = Driver_{tonic} + Driver_{phasic} = Driver_{SC} \tag{19}$$

Indeed, deconvolving SC data yields a driver function that includes both a phasic and a tonic component, thus identifying the driver of the whole SC activity. If one if the two components can be estimated, the other is implicitly determined.

According to this approach, thus, the extraction of both tonic and phasic activity was carried out through deconvolution of SC data, where the phasic driver component exhibits a virtual-zero baseline and distinct phasic responses [55].

Lastly, to assess variations among different physiological conditions, it is also important to evaluate the mean values of the GSR level and SCL component over time, together with the number of peaks of the SCR component, that could be potentially related to the level of cognitive and emotional stress [134].

2.2.3 RESPIRATORY SYSTEM PARAMETERS

As previously mentioned, the PPG signal is not only useful for assessing the cardiac and vascular health, but it also provides information about the respiratory system, as it allows for the determination of blood oxygen saturation levels through SpO_2 calculations, together with the possibility to estimate the respiration rate.

The SpO_2 values can be computed exploiting the fact that the absorbance of a red blood cell coincides with that of a hemoglobin solution [135]. This "transparency" of erythrocytes allows measurements of oxygen saturation, expressed as the percentage of hemoglobin that is saturated by oxygen, typically included between 95% and 100% at sea level [136]. For this purpose, it is possible to take advantage of the knowledge of the variation in the absorption spectrum of hemoglobin in relation to its degree of saturation by oxygen, shown in Figure 2.6 [137].

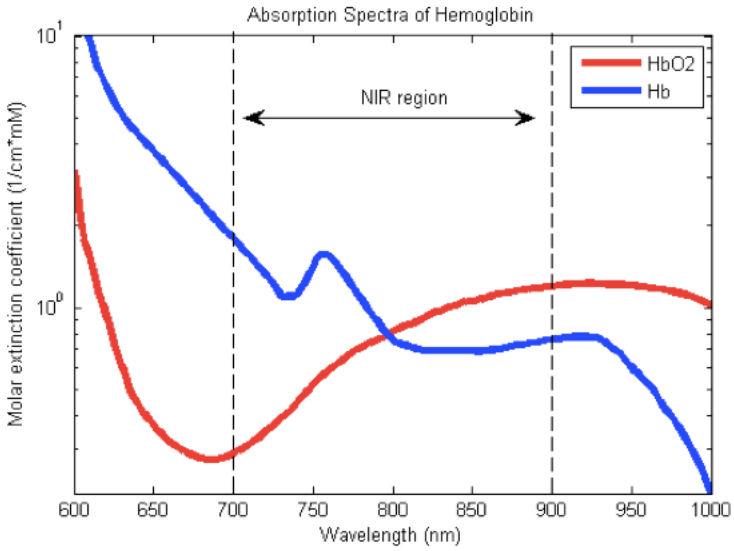

Figure 2.6 *– Absorbance curve of oxygenated and deoxygenated hemoglobin.*

Since the isosbestic point of the hemoglobin spectrum is located at 805 nm, a pulse oximeter usually exploits two LEDs emitting both a red light, typically with wavelength $\lambda = 650 - 670$ nm, and an infrared light, with $\lambda = 870 - 890$ nm, used in combination with a receiving photodiode.

After acquiring the two optical pulse waves from both the red and the infrared LEDs, is possible to express the so-called ratio of ratios "R" as [138]:

$$R = \frac{\frac{AC_{red}}{DC_{red}}}{\frac{AC_{ir}}{DC_{ir}}} \tag{20}$$

R is a ratio of ratios of the pulsatile and non-pulsatile components of red-to-IR light absorption; the light absorption of two wavelengths is thus derived from the pulsatile-added volume of oxygenated arterial blood [139], [140].

The AC and DC components of both red (i.e., AC_{red} and DC_{red}) and infrared (i.e., ACi_r and DCi_r) PPG signals can be evaluated starting from the extraction of the minimum and maximum peaks of the respectively waveforms. In particular, the DC component can be evaluated as the mean value between the maximum and minimum peaks of the pulse wave signal, while the AC component can be evaluated as the difference between the two peaks. A widely employed linear empirical equation for computing SpO_2 is the following [141]:

$$SpO_2 = a + b \cdot R \tag{21}$$

where a and b are two constants to be determined through calibration according to the optical characteristics of the adopted device.

As well-established in the literature, the PPG signal is modulated by respiration. Consequently, through specific data analysis techniques, it is possible to isolate the modulating component and extract the respiratory rate. Specifically, in this work have been considered two different techniques based respectively on a filtering-based approach and Empirical Mode Decomposition (EMD) [142].

The first approach, which is the simplest, involves applying a bandpass filter to the PPG signal, accounting for a range of respiratory frequencies determined in accordance with the knowledge that respiration variability usually falls within the HF band (i.e., 0.15-0.4 Hz) [32], [49]. The simplicity of this approach is counterbalanced by its weakness, which is due to the fact that, in this way, the respiratory signal is reconstructed within a band defined a priori, and this can lead to distorting estimates of respiratory frequency.

In fact, depending on the subject's physical activity and physio-pathological conditions, the respiratory frequency could fall outside the selected band. This situation would lead to the inconvenient circumstance of having to adjust the filtering settings each time to fit the optimal band, which varies from subject to subject.

For this reason, although this technique is much simpler to use, the technique based on the EMD algorithm has also been investigated and employed.

The EMD method has been already widely used for extracting breathing rate from PPG Signals [142], [143]. In this work has been used a simplified version of the EMD algorithm presented in [142], herein summarized:

i. Find the local maxima (M_i) and the local minima (m_i) of the PPG signal (*x(t)*);
ii. Interpolate the maxima and minima using the same number of points of the PPG, so as to generate the upper *M(t)* and lower *m(t)* envelopes, respectively;
iii. Compute the average envelope as $e(t) = \frac{M(t)+m(t)}{2}$;
iv. Subtract the average envelope to the PPG signal, $x(t) \coloneqq x(t) - e(t)$;
v. The steps (i)-(iv) should be repeated until the new *x(t)* does not vary from the *x(t)* at the previous iteration.

CHAPTER 3

DESIGN AND REALIZATION OF THE RING-SHAPED WEARABLE DEVICE

3.1 OVERVIEW AND STRUCTURE OF THE CHAPTER

In this chapter, the wearable biomedical device developed throughout the research journey is presented, providing details on the design and development stages, in terms of hardware, firmware, and, finally, software perspectives.

The objective is to provide the reader with a thorough presentation of the choices made in terms of biosensors selection and layout design to realize a non-invasive multiparametric ring-shaped wearable devices capable of discriminating changes in physiological states, in response to the needs described in Chapter 1.

This is firstly addressed by providing an overview of the device's hardware, describing the system architecture, and then focusing on all the various composing blocks, which consist in digital sensors, analog sensors, power management system, and finally, the Bluetooth Low Energy (BLE) communication module.

For the same reason, the discussion includes the development of firmware that led to the programming of the system (i.e., microcontroller, digital sensors, and BLE module).

To complete the picture, an introduction to the software used is provided, which encompasses a graphic-user interface (GUI) specifically designed for communication between the device and a personal computer. Additionally, a description of the offline post-processing algorithms and procedures relying on the MATLAB environment, is given.

3.2 HARDWARE: SYSTEM ARCHITECTURE

The device proposed in this work has been designed to perform acquisitions of various physiological parameters of interest in a single body district in order to expand the kind of biomedical devices by introducing a solution fully exploiting the potential of wearable technologies. Specifically, herein is presented a novel ring-shaped wearable device capable to perform fingertips synchronous acquisitions of ECG, PPG, GSR, and motion signals, powered by a lithium battery and transferring data using BLE communication protocol.

Since the device aims to perform high-quality multiparametric acquisitions on the fingers of the hand, during the design phase most of the efforts were focused on developing a compact and comfortable device that employs miniaturized highly integrated components without compromising the lightweight and compactness, which are the typical characteristics of a wearable device.

Figure 3.1 depicts the system architecture of the device. It consists of a microcontroller-based device, wherein the microcontroller serves as the core of the system, overseeing and managing both analog and digital modules, the acquisition of physiological parameters, and ultimately, data exchange over BLE communication protocol.

The choice of microcontroller fell on the use of the ultra-low power STM32L4 series [144], manufactured by STMicroelectronics, which allows achieving the best trade-off between power consumption and a wide range of different interfaces for the parallel management of multiple analog and digital input/output peripherals, features needed for a multiparametric acquisition. In fact, the L4 series hosts the most commonly used communication protocols in the field of biomedical sensing, such as the Inter-Integrated Circuit (I^2C) and the Universal-Asynchronous Receiver Transmitter (U-ART) digital communication protocols. Additionally, it includes a high-performance analog-to-digital converter (ADC) that enables the acquisition and management of measurements from the analog sensors integrated in the system.

On the other hand, low power consumption is an essential requirement that a wearable device must satisfy and, for this reason, particular attention has been paid to the choice of all the remaining components in the system, favoring compact sensors and components capable of providing the same performance but with lower energy costs.

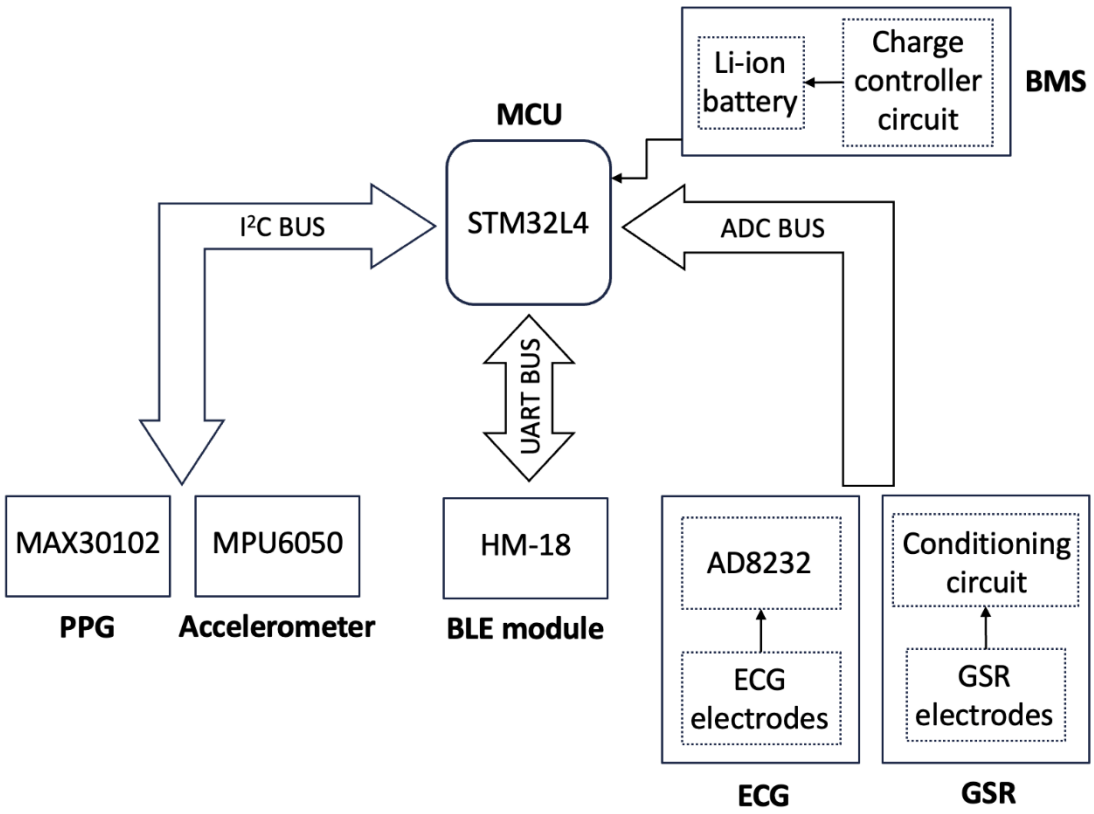

Figure 3.1 *– Schematic block representing the architecture of the system. The ultra-low power microcontroller (MCU) manages all the peripheral connected by using three different buses: I^2C BUS, which allows communications between MCU and digital sensors (PPG and inertial measurement unit); ADC BUS, used to connect analog signals output (ECG and GSR) to the MCU ADC; UART BUS, which is employed to communicate with BLE module in order to exchange the data collected by the MCU. Lastly, the battery management system (BMS) provides energy to the entire system.*

The management of peripherals is carried out through three distinct data BUS lines that have been specifically activated respectively to ensure communications with digital sensors, which occurs through the I^2C protocol (I^2C BUS), with the BLE module using U-ART serial protocol (UART BUS), and, finally, the reading of raw data originating from analog sensors (ADC BUS). The MAX30102 PPG sensor and the motion detection module MPU6050 (capable of gyroscopic and accelerometric measurements) together constitute the digital sensor system within the device. Although the BLE module also constitutes a digital system, since it does not detect any biometric data but simply handles the communication between the system and the computer, it is not considered within the biomedical sensing and is therefore treated and represented as a separate block.

The analog sensors block connected to the ADC BUS line consists of ECG and GSR sensors. As can be observed in the bottom right corner of Figure 3.1, each sensor can be divided into two main parts: the electrodes, which allow for the detection of electrical signals in specific areas of the fingers, and their respective conditioning circuits, which enable the generation of a high-quality signal for the subsequent sampling process performed by the MCU's internal ADC. In detail, the ECG signal is acquired through three electrodes and, unlike all the other extracted signals, it requires the use of fingers from both hands (specifically, the thumb of the left hand and the index and middle fingers of the right hand): the first captures the electrical potential on the phalanx of the left thumb (the same hand in which the device is intended to be worn); the second one serves the same purpose but operates on the right-hand index finger; finally, the third electrode is placed in contact with the right-hand middle finger and can optionally be used to exploit the right leg drive (RLD) circuit, which reduces electrical noise and enhances the quality of the recorded ECG signal. With this spatial arrangement due to the ECG configuration, the electrodes follow the geometry of the Einthoven's Triangle, avoiding the electrical potentials measurements from both the right and left body regions, thus enabling the acquisition of a single-lead ECG [145]. The signal detected by the electrodes is then sent as input into the AD8232 chip, an integrated analog front-end appositely designed for the measurement of biopotentials, directly allowing the extraction, amplification, and filtering of the small biopotentials detected by the electrodes. The AD8232 output is then connected to the ADC BUS line, where the high-quality ECG signal can be accurately sampled.

The GSR signal is acquired through two electrodes placed in contact with two diametrically opposite areas of the index finger of the left hand. From a methodological perspective, the measurement of this signal relies on the volt-amperometric method for acquiring skin resistance measurements. By applying an electrical potential to one electrode and measuring the remaining potential in the other one (called sensing electrode) while also monitoring the current passing through the electrodes, it becomes possible to determine the resistance value provided by the epidermal tissue [51]. The signal detected by the sensing electrode is once again routed to a dedicated conditioning circuit that, through amplification and filtering operations, improves the signal quality. Finally, the output of the conditioning circuit is connected to the ADC BUS line. The acquisition of both analog signals output from their respective conditioning circuits is carried out by the internal ADC of the MCU.

For the wireless communication of the biosignals recordings, the choice has fallen on the BLE communication protocol, which, with an excellent trade-off between transmission speed and energy consumption, is among the most commonly used wireless communication protocols in the field of wearable technologies [34], [146].

For the implementation of BLE communication, the HM-18 module based on Texas Instruments CC2640R2F IC has been utilized, which is controlled by the MCU through the UART BUS line and, once paired, enables data exchange with other nearby BLE devices. Finally, as depicted in the top right corner of Figure 3.1, the entire system is powered by the Battery Management System (BMS), which provides the voltage levels required by the other components (i.e., MCU and sensors).

Beyond the architecture of the system, the shape of the device has been appositely designed in order to assure the flexibility in terms of acquiring the signals acquiring high quality signals without compromising the compactness and adaptability of the product. A ring-shaped device can satisfy both needs with the drawback of a slightly more expensive production process and more complex assembly procedure, due to the use of flexible printed circuits.

Figure 3.2a shows both the top and bottom views of the printed circuit board (PCB) designed for the realization of our device. In detail, the rigid PCB (in green) houses all the above-described components except for the MAX30102 sensor, which is instead integrated into the flexible PCB (in yellow) to acquire the PPG signal on the underside of the finger. The yellow areas in the top view of the rigid PCB (highlighted by the red squares) represent the first two ECG electrodes, while the third electrode is indicated by the red rectangle in the bottom view of the flexible PCB. The PCB integrates two GSR electrodes as well, denoted by the two blue rectangles in the top view. The dimensions of these two conductive pads are 20x8 mm and 17x8 mm respectively for the two GSR electrodes and the ECG electrode on the finger, whose dimensions have been made long enough to guarantee a proper contact with the skin. Moreover, in order to improve the ECG electrodes usability, two hot air solder leveling (HASL) finished pads are positioned in the forward part of the PCB, which also avoid undesirable contacts between the fingers and other parts of the PCB. The potential problem with the reliability of ECG measures is solved with a proper choice of the electrode positions. Similarly, from preliminary tests, it has been observed that an 8 mm diameter allows for an adequate contact between the skin and electrodes and reduces inter-subject variability.

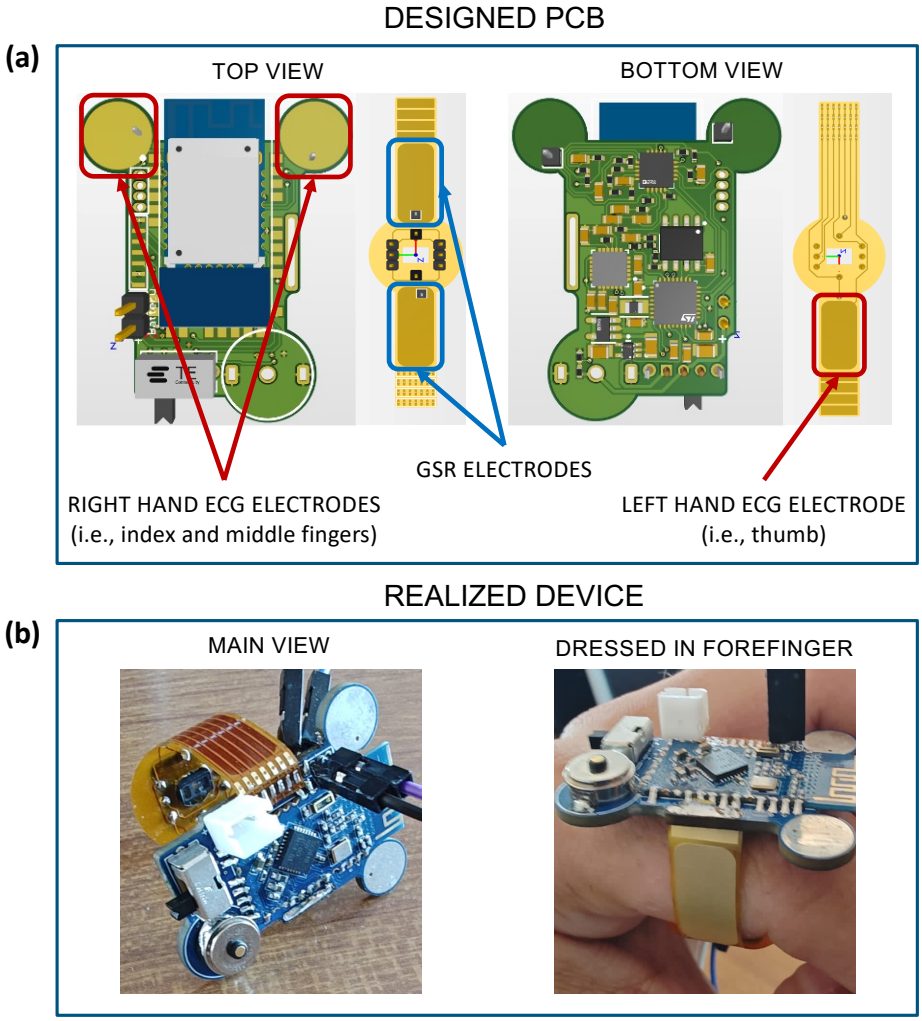

Figure 3.2 *– **(a)** Top and bottom views of the rigid PCB (in green) and flexible PCB (in yellow), the latter hosting the PPG MAX30102 sensor for acquiring the PPG waveform on the underside of the finger. The ECG and GSR electrodes are highlighted with red and blue rectangles, respectively; the fingers used for the acquisition of the ECG signals are indicated in parentheses. **(b)** The realized ring-shaped device, in its main view (left) and while being dressed in the forefinger (right).*

The last design constraint imposes to avoid the placement of components on the top side of the PCB, in such a way to leave the whole space for Bluetooth module. Particular care has been put for BLE antenna positioning, that has been placed outside the PCB to maximize irradiation performances. The final circuit has been carefully designed to reduce mutual interferences between analogue highly sensitive traces and digital paths; for this reason, a multi-layer routing technique has been applied. The PCB is thought to be produced in factory with pick'n place machines and reflow soldering techniques only. In this way it has been possible to shrink components with tenths of millimeters tolerance.

The whole work has been done by using the CAE software Altium Designer 22.
In Figure 3.2b the realized wearable device is depicted. The left panel represents the ring-shaped device in its final form. Here, the main rigid PCB can be seen, encompassing all the electronic components besides the ones used for PPG acquisition. In the figure it is possible to distinguish a switch to turn on the device, the Bluetooth module used for wireless communications, the battery connector, the two circles-shaped ECG electrodes on the upper part, and a magnetic two pole connector used for battery charging. Compared to standard USB-C charging solutions, a magnetic connector significantly helps ensuring compactness on the device, however a dedicated charger for the device is needed. The black connectors have been used only for programming purpose during testing phases, and they are not an integral part of the circuit, in fact they can be easily removed once the final version of the firmware has been uploaded on the microcontroller. The yellow part is the flexible PCB, which is realized using a 0.2 mm polyimide film. It performs three functions, i.e. guaranteeing a proper wearing of the device around the finger (as shown in the right panel of Figure 3.2b), hosting the integrated circuit for PPG acquisition in reflection mode, and providing conductive surfaces usable as electrodes for ECG and GSR acquisition. For these measurements, the proper and good contact between skin and electrodes is essential. Therefore, the flexible PCBs have been realized with the electroless nickel immersion gold (ENIG) surface finish process, so as to avoid the oxidation problem.

3.2.1 MICROCONTROLLER UNIT: STM32-L432KC

The STM32L4 microcontroller family includes several solutions that offer different features and specifications and can thus be used for various applicative contexts. In this case, the STM32-L432KC (depicted in Figure 3.3a) has been chosen, which consists in a ultra-low power microcontroller based on the high-performance Arm Cortex M4 32-bit RISC core operating at frequencies up to 80 MHz, which hosts a 12-bit ADC, along with numerous communication interfaces, including USB 2.0 full speed, low-power U-ART, and two separate I^2C channels [144]. Its characteristics enable efficient management of the data reading and exchange processes without latency issues while ensuring ultra-low-power capabilities, essential for a battery-powered device.

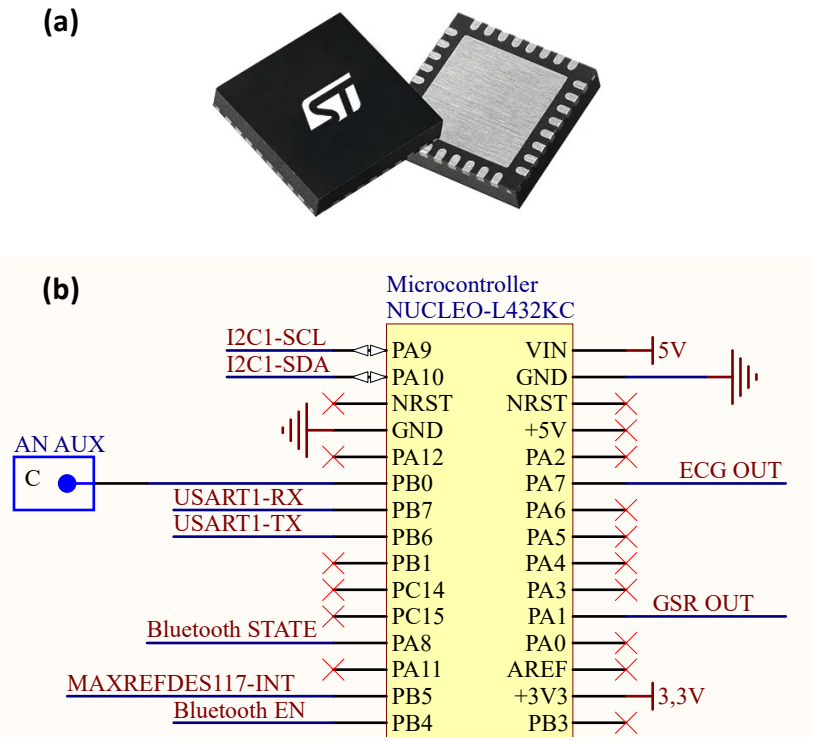

Figure 3.3 *– **(a)** Image of the STM32-L432KC microcontroller chip in both top and bottom views. **(b)** Electrical schematic displaying the pinout of the microcontroller pinout and its assignment to other peripherals in the system.*

Figure 3.3b depicts a detail of the device electrical schematic on the MCU pinout and its interfacing with other modules and peripherals. Indeed, it can be observed how both I^2C and U-ART data lines have been enabled, respectively for managing digital sensors and the BLE module, along with its status signal (named Bluetooth EN) and the interrupt from the PPG sensor (MAXREFDES117-INT), which, as will be explained later, identifies the synchronization signal among all the biometric measurements carried out by the system. Finally, there are lines dedicated to acquiring the output signal from the analog sensors (ECG OUT, GSR OUT) by the ADC, and power supply lines, respectively for input (5V) from the BMS and supplied (3.3V) by the MCU.

3.2.2 PPG SENSOR: MAX30102

The MAX30102 (manufactured by Analog Devices) is an integrated sensor designed for acquiring the PPG waveform using a reflective LED solution, which is achieved through the use of a photodetector and two light sources emitting at wavelengths in the red spectrum (660 nm) and in the infrared spectrum (880 nm), transferring data via I^2C protocol [147]. The MAX30102 features a high-resolution (up to 18 bit) internal ADC with low noise characteristics, complemented by an ambient light rejection circuit. Both elements contribute to obtaining high-quality PPG signals under typical usage conditions, including situations with significant ambient light presence. In particular, the immunity of the front-end to the ambient light was checked through different measurements carried out, firstly, in dark ambient conditions and then by simulating the sunlight with an Oriel Sol3A solar simulator (manufactured by Newport), with the output set at 0.8 sun, i.e., a typical value in a sunny day condition. The measurement results showed the excellent behavior of the MAX30102, detecting only a slight percentage increase in the DC components of the PPG red (0.17%) and infrared (0.5%) waveforms. No changes were reported for the AC components, thus validating our probe for acquiring PPG signals even in the presence of a strong ambient light [64].

Figure 3.4 depicts the chip used for integrating the MAX30102 sensor within the system. Being a very small component, it was utilized in the form of a development board using the shield named MAXREFDES117, which enables an easier use of the above-mentioned PPG sensor.

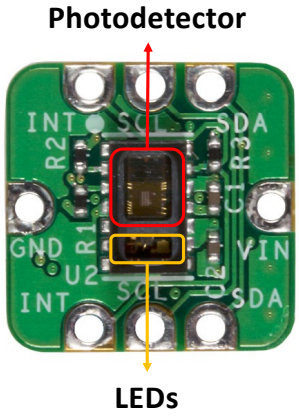

Figure 3.4 *– MAXREFDES117 development board. The rectangles in red and orange highlight, respectively, the photodetector and both the red and infrared LEDs that are located in the MAX30102 sensor.*

An important feature consists in the possibility to increase the sampling frequency of the PPG signal without reducing the resolution of the internal ADC.
In this application, the MAX30102 has been configured to acquire both wavelengths at a sampling frequency of 1 kHz, corresponding to a 16-bit ADC resolution. This sampling rate allows to carry out various analyses that necessitate high temporal resolution of the processed signals, such as HRV analyses and PAT computation, the latter enabling the detection of time delays on the order of milliseconds between ECG and PPG waveforms.

3.2.3 ECG ANALOG FRONT-END: AD8232

The acquisition of the ECG signal is entrusted to an analog front-end that stands out as a leading solution in the wearable device market: the AD8232. This component, manufactured by Analog Devices, is specifically designed for single-lead ECG measurements, making it widely applicable in fitness and activity heart rate monitors, remote health monitors, and other types of biopotential signal acquisition [148].
The AD8232 is designed to extract, amplify and filter very low biopotential signals, also in the presence of noisy conditions, elevating the signal initially detected by the electrodes to a higher level, and providing an output signal that can be adequately sampled by the ADC placed at its output.
Among its main features, first and foremost, there is an excellent trade-off between the quality of the acquired signal and energy cost, making it a perfect component for integration into the wearable device. Another important feature is the ability to easily modify the type of filtering applied to the detected signal. For instance, the AD8232 can implement a two-pole high-pass filter to eliminate motion artifacts and the electrode half-cell potential. This filter is coupled and integrated with the amplifier's instrumentation architecture, allowing both a large gain and high-pass filtering in a single stage, thus saving space and cost. Furthermore, it is also possible to create a three-pole low-pass filter to remove additional noise, and the user can always select the frequency cutoff of all the filters to suit different types of applications.
The schematic diagram is presented in Figure 3.5, appropriately sized to integrate the AD8232 into the wearable device. The inputs LA, RA, and RL correspond to the 3 electrodes that come into contact with the fingers through the different pads used by the system for ECG signal acquisition, as previously explained.

The resistive-capacitive network serves as a filtering circuit and has been specifically sized to operate the AD8232 in the cardiac monitor configuration.

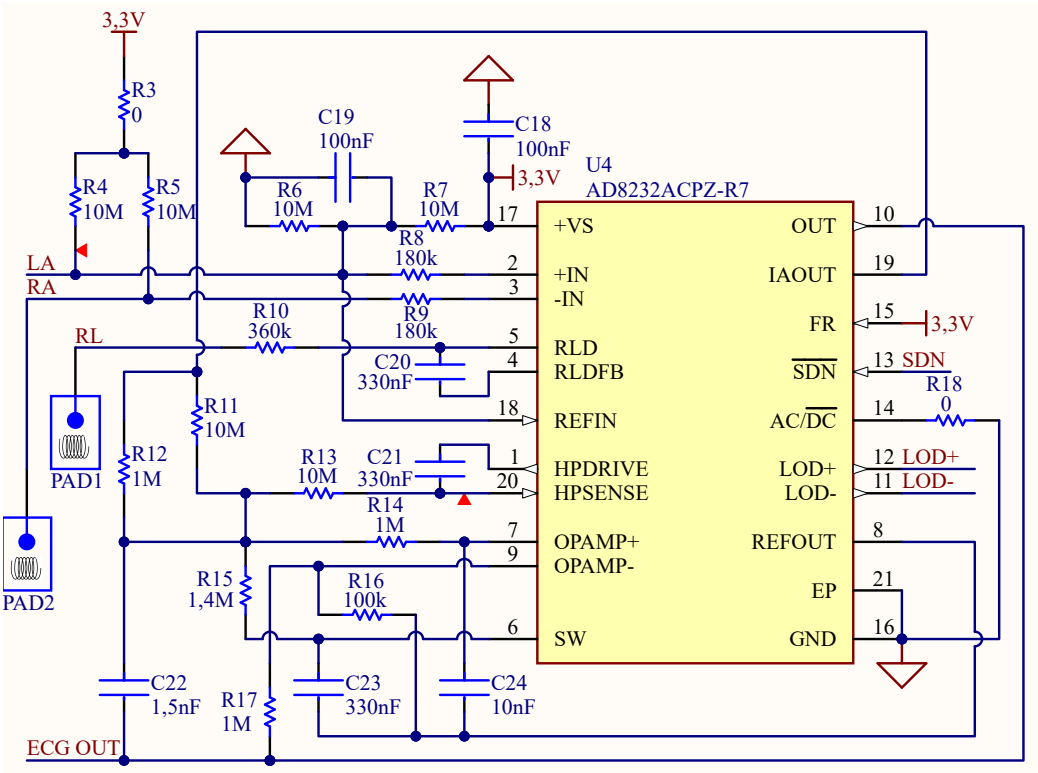

Figure 3.5 *– Schematic diagram of the AD8232 and the external resistive-capacitive network implemented on the PCB in accordance with the manufacturer's datasheet instructions related to the cardiac monitor configuration.*

This configuration is designed for monitoring the shape of the ECG waveform. It assumes that the patient remains relatively still during the measurement, and therefore, motion artifacts are less of an issue. Indeed, the AD8232 is configured as a second order bandpass filter, with respectively lower and higher cutoff frequencies of 0.5 Hz and 40 Hz. Moreover, the third electrode could be used for optimizing the commode-mode rejection following the working principle of the RLD circuit. In addition to 40 Hz filtering, operational amplifier stage is configured for a gain of 11, resulting in a total system gain of 1100. To optimize the dynamic range of the system, the gain level is adjustable, depending on the input signal amplitude (which may vary with electrode placement) and ADC input range.

3.2.4 GSR ANALOG FRONT-END

The acquisition of the GSR signal is also carried out by the internal ADC of the microcontroller, which is placed at the output of a fully analog conditioning circuit designed specifically for skin conductance measurements. The circuit is suitable for the MIKROE-2860 GSR module, produced by MikroElektronika, which allows GSR measurements based on the detection made by two electrodes applied to a specific body area [87]. For design reasons, the circuit has been modified and reproduced on a PCB, allowing for space optimization suitable for use in wearable devices like the one under consideration.

Figure 3.6 depicts the schematic of the analog front-end for GSR implemented on the PCB.

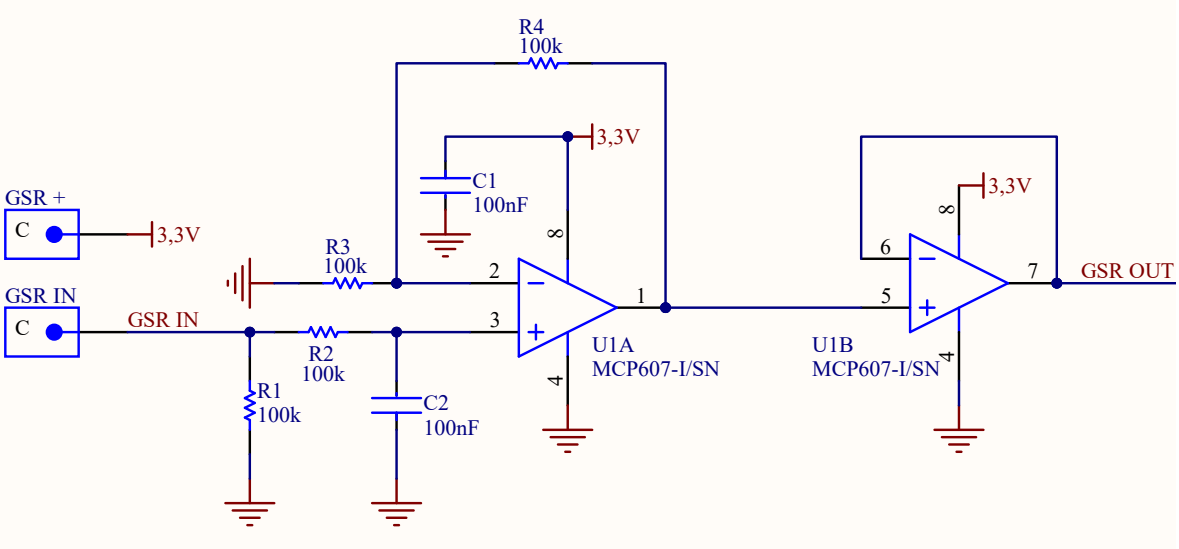

Figure 3.6 *– Electric schematic of the analog front-end for the acquisition of the GSR signal, integrated in the PCB of the realized system.*

It is possible to describe the working principle of the circuit by tracing the path that the signal (GSR IN) takes step by step from the input to the output of the circuit. A constant voltage is applied to the electrode located on one side of the finger (GSR +), resulting in a current flowing from the second one (GSR IN). Knowing the residual potential at this second electrode (i.e. voltage on resistor R1 terminals) it is possible to calculate the current flowing on it which is the same flowing on the skin resistance. A passive first order low-pass filter composed by resistor R2 and capacitor C2 limits the signal response with a cut-off frequency of 15.9 Hz.

The detected and filtered potential on R1 is therefore doubled by the non-inverting op amp amplifier circuit which, thanks to R4 and R3 resistors of equal value present in the feedback loop, has a fixed gain of 2, and decoupled from the rest of the front-end by a final buffer stage. Finally, the output of the circuit (i.e. the buffer output) is connected to the internal ADC of the microcontroller, which is able to properly sample the GSR signal.

3.2.5 GYROSCOPE AND ACCELEROMETER SIGNALS: MPU6050 MODULE

The MPU6050 is a complete inertial measurement unit, known for its solid performance in capturing acceleration and angular velocity data [149].

In Figure 3.7 the electrical schematic of the MPU6050 is shown, which has been interfaced on the PCB according to the manufacturer's specifications. These specifications correspond to the configuration present on the development board of the component, commonly known as the GY-521 module.

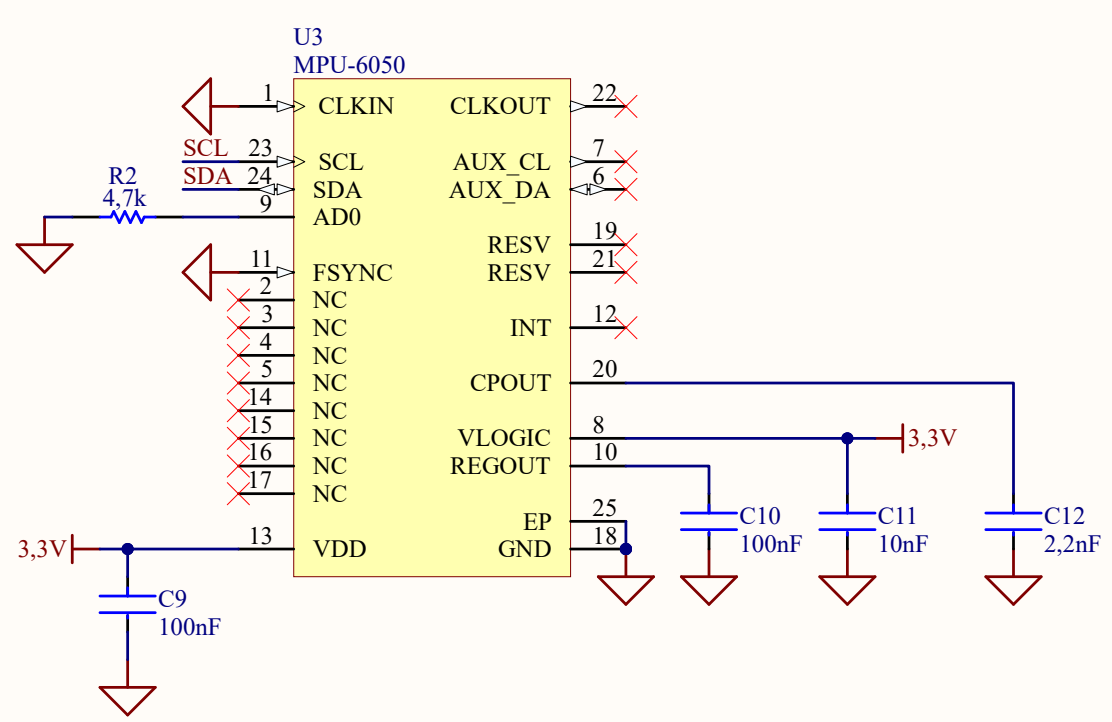

***Figure 3.7** – Detail of the electrical schematic of the MPU-6050 module implemented on the PCB of the wearable device, sized according to the manufacturer's datasheet provisions.*

This compact module integrates both a 3-axis accelerometer and a 3-axis gyroscope, making it an invaluable tool to be integrated into the realized device. In this work, the MPU6050 has been implemented in the system to acquire reliable acceleration signals along the three orthogonal axes (i.e., x, y, and z directions).

The communication and data transfer are carried out, as in the case of the MAX30102, via the I^2C protocol. Furthermore, the PCB implementation has significantly reduced the footprint of the sensor, effectively occupying a much smaller portion of the entire wearable device. Lastly, in order to align the sampling frequency with that of the PPG sensor and to ensure the highest fidelity in data capture, this module has been set with a sampling frequency of 1 kHz, so that motion data can be ready to acquire whenever the interrupt of the MAX30102 occurs.

3.2.6 BLUETOOTH LOW ENERGY: HM-18 MODULE

The BLE is a wireless communication protocol designed for short-range communication with low power consumption. One of its main advantages is the energy efficiency, making it ideal for battery-powered devices and applications where power consumption is a critical factor. Furthermore, the latest versions of the BLE protocol (i.e. BLE 5.0 or higher) allow for a significant increase in data transmission speed, reaching theoretical values of up to 2 Mbps, reason for which BLE is widely used in various fields, including healthcare, fitness, home automation, and wearables [146].

The HM-18 module, for instance, is a Bluetooth Low Energy module which integrates BLE 5.0 version and facilitates the integration of BLE capabilities into electronic devices, thanks to its low cost, reduced size, ease of use, and wide availability on the market [150]. It is based on the CC2640 IC chip, which is a microcontroller developed by Texas Instrument appositely designed to manage the BLE radio frequency transceiver, optimizing performance in terms of data rate and energy cost and supporting U-ART communication.

In Figure 3.8, the top and bottom views of the HM-18 module (Figure 3.8a) and the electrical schematic (Figure 3.8b) illustrating the interconnection of the component on the PCB are shown. As observed from the pinout, the integration of the module proved to be extremely straightforward, as most of pins, following the manufacturer's instructions, are set by default to remain unconnected.

The lines for communication via the U-ART protocol are enabled, allowing the BLE module to receive processed data from the wearable system and send it to the PC (and vice versa).

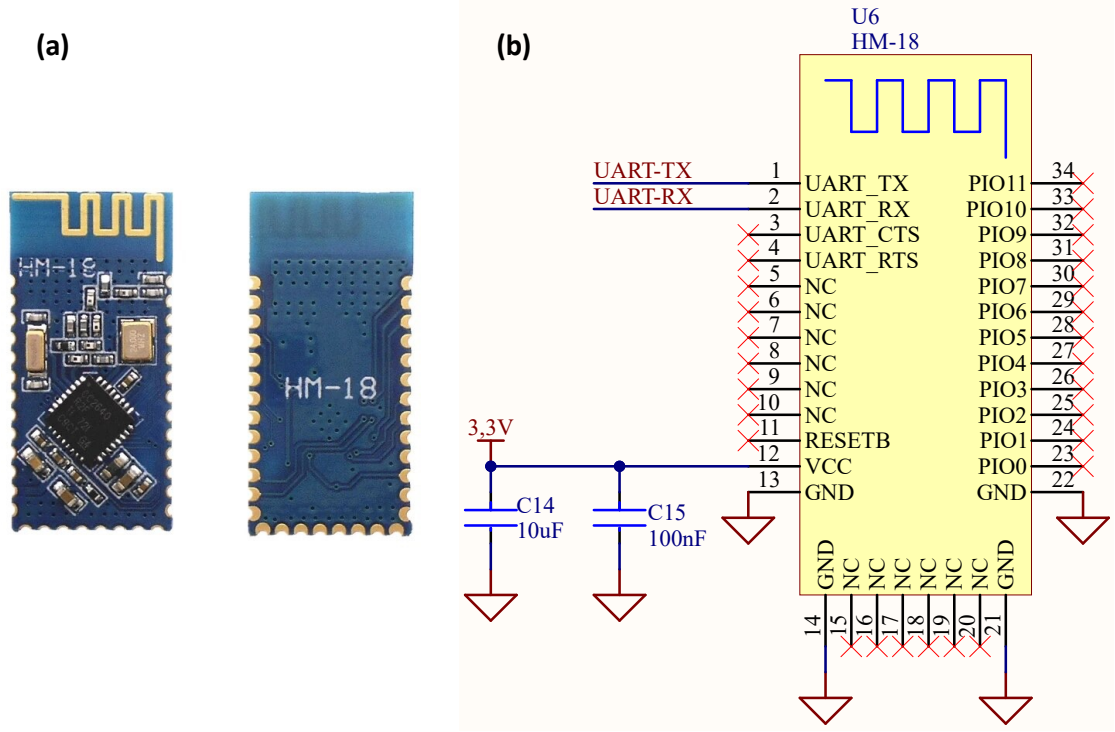

Figure 3.8 *– **(a)** Top and bottom views of the BLE module HM-18 in its chip version, integrated into the wearable system. **(b)** Electrical schematic of the same module arranged on the PCB of the developed system.*

3.2.7 BATTERY MANAGEMENT SYSTEM

The hardware discussion related to the design and development of the wearable system is completed by the presentation of the last electronic sub-block, BMS. As evident from Figure 3.1, the BMS essentially consists of two blocks: the charge controller circuit and the Li-ion battery. The charge controller manages the lithium battery in terms of charging, regulating the current based on the charge level and indicating through two LED status indicators whether the battery is in the charging phase or currently discharging. The lithium battery, for instance, ensures high-performance and long-lasting operation of the device. However, there is the need to adjust the voltage levels provided when charged, which usually hover around 3.7V (e.g., when the battery begins to significantly discharge and therefore needs to be recharged), to those required by the implemented system.

For this reason, there is an additional small electronic circuit that interfaces the battery with the microcontroller, allowing the voltage levels to be adjusted to those required by the latter, and thus from 3.7V to 5V. Finally, as it was important to optimize space on the PCB of the wearable device, the BMS has been divided into two boards, in order to obtain an external circuit that is responsible for charging the battery, and an internal circuit which handles the voltage level interfacing, along with the power state (on or off) of the device, managed by a switch.

The electric schematics of both circuits are shown in Figure 3.9. The charger control circuit is TC4056 IC [151], an electronic component that manages the charging process using the power supplied by the USB-C connector and providing a constant charge through a pogo connector (POGO-1). This connector magnetically connects to the lithium-ion battery (POGO2) present in the wearable device and directly links the outputs of the charger circuit (Battery+ and Battery-) to the terminals of the battery.

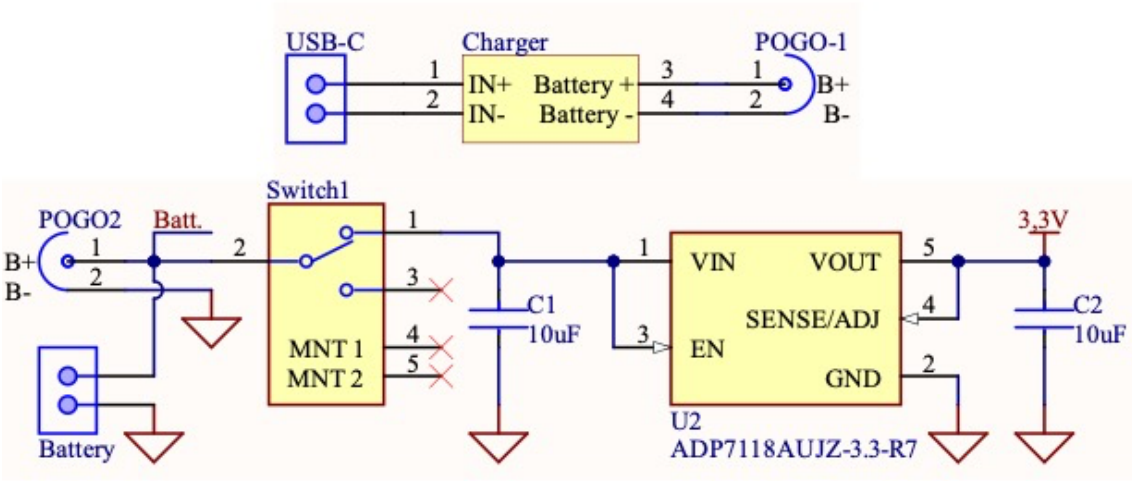

Figure 3.9 *– Electrical diagram of the BMS of the system. In the top panel, the charge controller circuit, implemented on an external board. At the bottom, the charge reception circuit, including the voltage regulator and the power-on switch, implemented on the wearable device.*

In the bottom panel of Figure 3.9, the BMS section realized within the wearable device is shown. There is a switch located to the positive of the battery that allows for system activation. Specifically, if the switch is in position 1, it connects the positive terminal of the battery directly to the input terminal of the ADP7118AUJZ-3-3R7 component, a voltage regulator that stabilizes the battery voltage level at 3.3V [152]. All other switch positions disconnect the power, leading to the shutdown of the device.

3.3 FIRMWARE: STM32 AND OVERALL SYSTEM PROGRAMMING

The system programming was carried out programming the firmware of the STM32 microcontroller, which includes code snippets to initialize and program the rest of digital sensor and components, such as the MAX30102 PPG sensor, the MPU6050 inertial module, and the HM-18 BLE module. The rest of the sensor components, being purely analog, are managed by the internal ADC converter of the microcontroller, which samples the outputs of both GSR and ECG signal analog front-ends.

The programming of the STM32 has been carried out using two proprietary development environments from STMicroelectronics, namely STM32CubeMX and STM32Cube IDE [153], [154]. The first allows interfacing with the microcontroller by setting the pinout, enabling peripherals, and configuring the features (e.g., timers, connectivity, computing, security and system core). Furthermore, a second panel allows the clock configuration, enabling the setting of the operating frequency for individual data buses, which in this case involve the I^2C and U-ART protocols, along with the sampling frequency of the internal ADC and the microcontroller frequency. This permits a more thorough programming approach, taking into account the energy cost of the system as well. The STM32Cube IDE environment, on the other hand, allows writing the firmware related to the routine that has to be performed by the system, which will be loaded onto the microcontroller, automatically preloading the code segments defined earlier in STM32CubeMX.

Finally, once the firmware generation is completed in both development environments, the code is loaded directly from STM32CubeIDE using a simple USB cable for programming the microcontroller on the development board. However, it is as well possible to directly program the microcontroller, by loading the firmware using the ST-LINK, a debugger and programmer circuit produced by STMicroelectronics.

Figure 3.10 displays the main screen of the STM32CubeMX development environment with a detailed view of the pinout for the STM32-L432KC and the enabled functionalities. The I/O peripherals have been configured to interface the microcontroller with digital sensors by enabling I^2C (I2C1) and U-ART (USART1) communication lines, setting the maximum transmission speed, and so 400 kbit/s and 230400 bit/s, respectively. Additionally, to capture the synchronization signal from the PPG sensor, the interrupt features (NVIC) of pin PB5 were enabled, directly connected to the interrupt of the MAX30102, along with the timer register (TIM7) to maintain proper event timing.

In addition, the interrupt of the U-ART reception pin (PB7) is also enabled so that, as will be explained later, it is possible to start and stop the acquisition at any desired moment, regardless of the interrupt from the PPG sensor. The internal ADC was also enabled in continuous mode with a conversion count of 2 to adequately acquire analog signals from the GSR and ECG analog front-ends (ADC1_IN2 and ADC1_IN6, respectively). The ADC was set to 10-bit resolution, applicable to both signals, and a sampling frequency of 1 kHz. After multiple tests, it has been necessary to activate the direct memory access (DMA) on both the ADC and U-ART lines to allow quick access to ADC samples and facilitate data transmission via BLE.

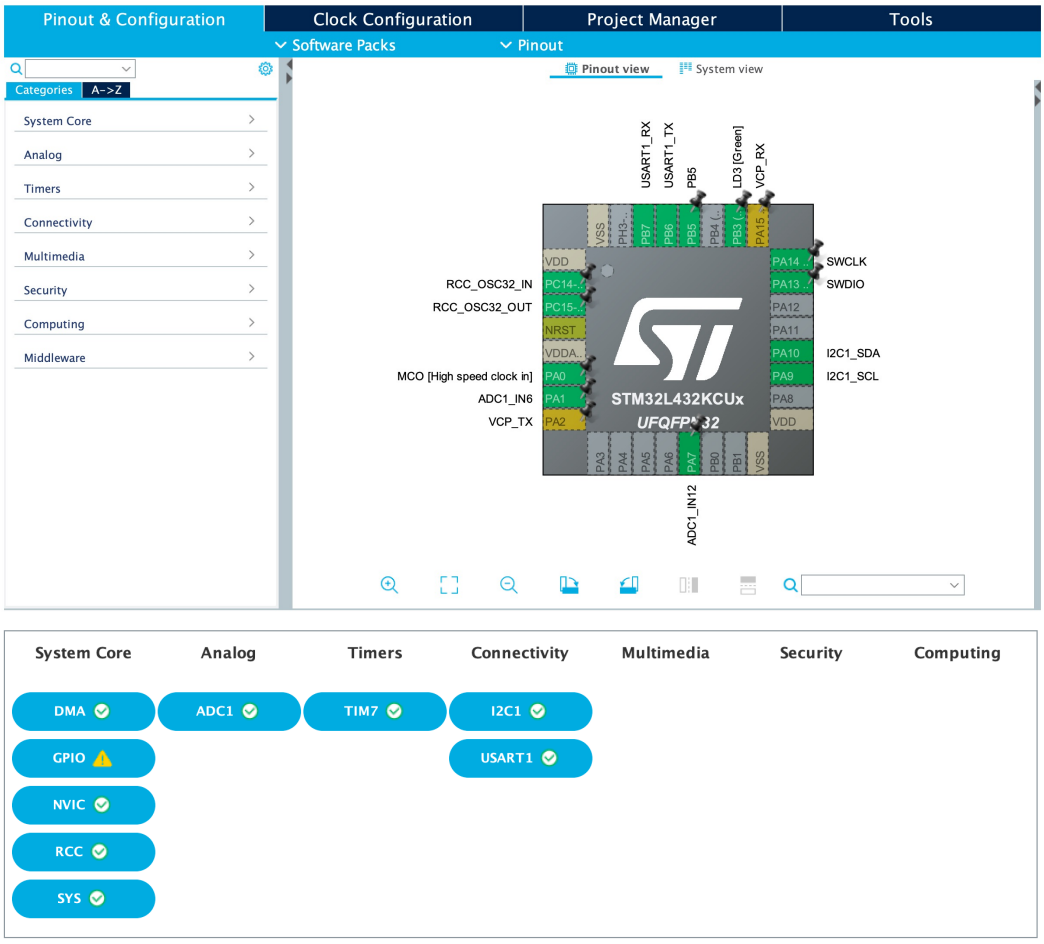

Figure 3.10 *– At the top, the main view of the STM32CubeMX development environment displaying the pinout and configuration of the STM32-L432KC microcontroller programmed for the system. At the bottom, a detailed view of the enabled microcontroller functionalities.*

Finally, the clock frequency of the microcontroller has been set to 80 MHz, which is the maximum operative frequency, in order to ensure high performance in managing peripherals and executing tasks within the system.

Once the microcontroller configuration is complete, STM32CubeMX generates the code, which consists of parts intended for compilation by the programmer (i.e., the user code), along with pre-compiled parts related to the microcontroller settings. Successively, the user code can be compiled in the STM32CubeIDE environment.

For this application, the code has been written using the Hardware Abstraction Layer (HAL) functions, derived from the corresponding proprietary libraries by STMicroelectronics, that are specifically developed to optimize operations for STM32 microcontrollers in terms of computational costs and power consumption [155]. Additionally, the “string.h” and “stdio.h” libraries were employed for string operations and to optimize the management of I/O peripherals, respectively.

The code is designed to define a finite state machine, starting from a default state, waiting for instructions from the U-ART port (i.e., the BLE module) to switch to the operational state, in which signal acquisition and data exchange occurs.

The default state is the one the system enters as soon as it is powered on, and a series of operations occur sequentially to initialize the two I^2C sensors and the BLE module. The initialization process has been designed starting from the programming of the digital devices, thus considering the register structure of the MAX30102 and MPU6050, and the exchange of AT commands for setting up the BLE module. In particular, the initialization routine of the MAX30102 involves setting the registers to enter the defined SpO_2 mode, where the dual acquisition of the PPG waveform with both red and infrared wavelengths occurs, also setting a sampling frequency of 1 kHz, and enabling the signaling of the completed acquisition through the interrupt pin. Similarly, the MPU6050 is programmed to provide gyroscope signals (G_x, G_y, and G_z) and accelerometer signals (A_x, A_y, and A_z) at a sampling rate of 1 kHz, in order to have information regarding the subject's movement at the same temporal resolution as the previous signals. Finally, the BLE is initialized by sending an AT command on the U-ART port to set the bitrate to its maximum, i.e., 230400 bits/s, making it compatible with the same speed set on the corresponding U-ART lines of the microcontroller.

The operational state is enabled by sending a keyword from the GUI, which is transmitted to the BLE module in the system. Specifically, the arrival of a message via U-ART triggers corresponding interrupt routine of the system, where the message is decoded and interpreted.

There can be two messages which indicate the start and the end of acquisition, respectively. In the case of the start instruction, the system immediately transitions to the operational state; otherwise, it returns to the default state and waits for a new message from the BLE.

The operational state is characterized by a series of tasks, which can be summarized in the sequential execution of the following subpoints:

I. Enable the interrupt pin of the microcontroller connected to the corresponding pin of the MAX30102 and send an I^2C instruction to initiate acquisition by the MAX30102;
II. Start continuous mode acquisition by the ADC for GSR and ECG signals;
III. Send an I^2C instruction to initiate acquisition by the MPU6050;
IV. Wait for the interrupt signal from the MAX30102;
V. Save the measurements obtained by each module in a buffer with a size of 248 bytes, matching the maximum size of data packets handled by the BLE HM-18;
VI. Upon completing the buffer, send the data packet via U-ART to the HM-18 module, which sends the entire packet to the GUI;
VII. The routine restarts from point IV.

Once in the operational state, the system executes the above-described tasks for an indefinite period until the stop signal is received. The presence of two interrupts enabled simultaneously (i.e., MAX30102 and U-ART reception channel) led to the need to mask the interrupts to avoid putting the system in an indefinite state in the event of the concurrent presence of both signals. For this reason, the U-ART interrupt was assigned a higher priority level and can therefore interrupt the acquisition routine at any time, returning the system to the default mode.

3.4 SOFTWARE

Once the electronic device development phase, together the definition of the operating modes and data exchange type, have been completed, it has been necessary to consider the part related to the software implementation for the device control and management, as well as the processing and analysis of the measurements made by the device. To perform all these operations, two distinct software solutions have been implemented. These solutions enable the management of the remote device through the development of an ad-hoc realized GUI for the wearable system and the generation of code capable of analyzing measurements within a specific time window, extracting physiological indices from the examined parameters. Both solutions, described in the following subsections, have been developed in the MATLAB development environment.

3.4.1 MATLAB BASED GRAPHIC-USER INTERFACE

The MATLAB GUI has been designed with the aim to be used as a stand-alone application, allowing an easy installation and use directly on the user's computer. For data transfer, it exploits BLE communication between the computer and the wearable system, enabling remote device management, which is achieved through the transmission of keywords that facilitate the transition between the different states, as previously described. Once the acquisition is started, the interface allows real-time visualization of all the acquired biosignals. Additionally, leveraging the existing MATLAB libraries for biomedical data processing and analysis, it also allows various real-time operations that can be performed with reduced computational costs, such as biosignal filtering and extraction of key physiological indices.

The starting window of the application is depicted in Figure 3.11. The application screen features three mains button, namely "Connect BLE," "Start acquisition," and "Stop acquisition," used for system connection and management. Specifically, pressing the "Connect BLE" button the application initiates the search and pairing routine to the device, which ends when the BLE connection is established, indicated by the dedicated green indicator labeled "Status."

Before starting the acquisition process, it is necessary to set the sampling frequency of the device by selecting the desired frequency from the dropdown menu at the top right of the application screen (default set to 500 Hz but adjustable up to 1 kHz). Afterwards, it is possible to start the acquisition by pressing the “Start acquisition" button, which sends the keyword to enter the operational mode. Then, the windows showing in real-time the acquired signals, updated every second. Moreover, if the two checkboxes in the top right corner, named Gyro/Acc data and PPG/ECG peaks, are also checked, it is possible to show as well the signals from the inertial module and indicate in real time the markers for the peaks of PPG and ECG signals, respectively.

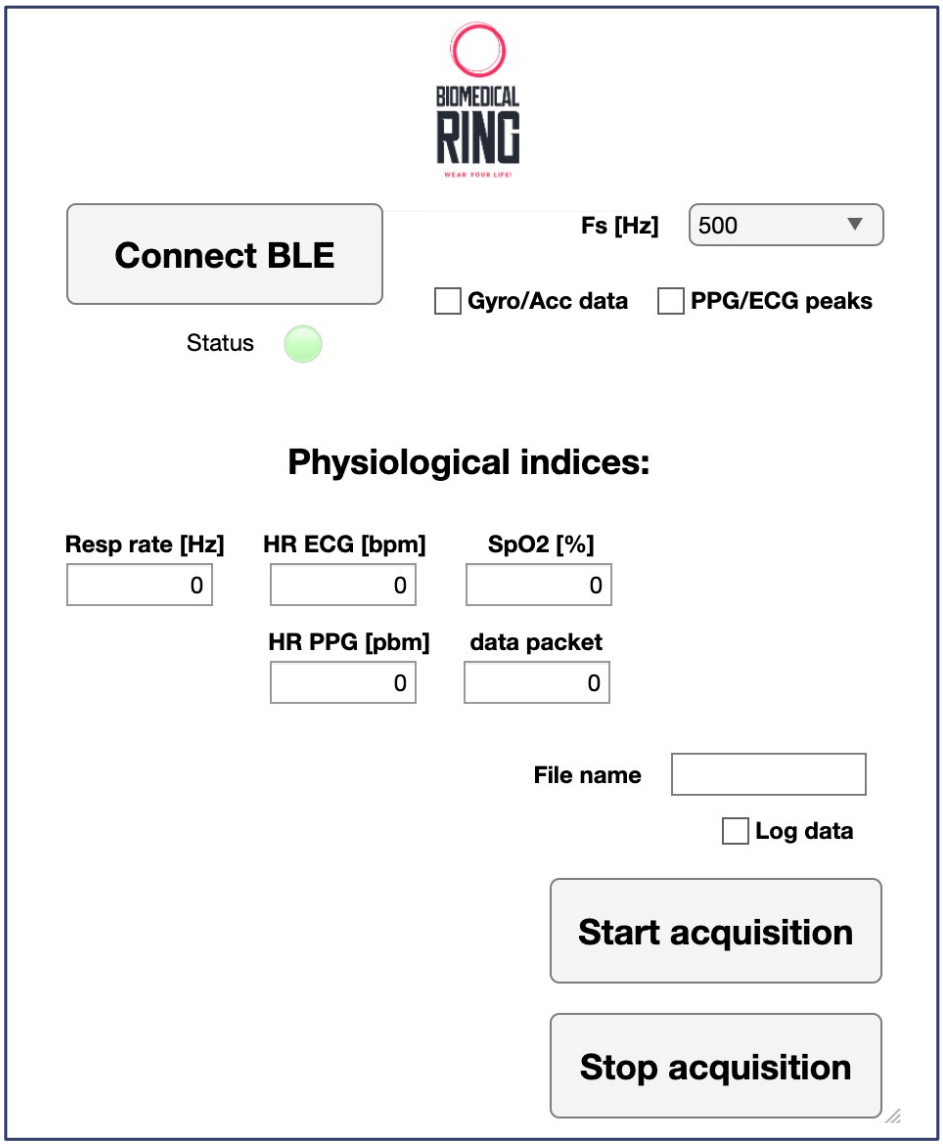

Figure 3.11 *– Graphical user interface created for the control and management of the wearable device, implemented using the MATLAB App Designer development environment.*

In the "Physiological Indices" section, output boxes have been set up to provide the user with key physiological indices extracted in real-time (i.e., respiration rate, ECG and PPG HR, and SpO_2 levels). The application features are completed by the possibility to save the acquired data in comma-separated values (CSV) file.

3.4.2 OFFLINE DATA PROCESSING

As previously described, the acquired data are saved by the GUI in a CSV file consisting of a matrix composed of 10 columns, containing the infrared PPG, red PPG, ECG, GSR, A_x, A_y, A_z, G_x, G_y, and G_z signals, respectively. The examined data are stored in raw format to allow the implementation of different filtering and processing techniques, depending on the types of data analysis to be performed on the signals. The CSV files can be directly opened using the MATLAB code developed for offline data processed. In detail, the filtering, processing, and analysis of the biomedical data are carried out separately depending on the considered biosignal. Due to the distinct characteristics in terms of shape and content, each biosignal needs to be treated with specific filtering techniques. In particular, the raw ECG signal was processed using a zero-phase fourth-order bandpass Butterworth digital filter, with lower and upper cutoff frequencies set at 0.1 Hz and 20 Hz, respectively. Subsequently, a Pan-Tompkins based simplified algorithm was employed to detect the R-peaks in the ECG trace [156]. The PPG signals (both red and infrared) were processed using a zero-phase fourth-order lowpass Butterworth digital filter, with a lower cutoff frequency of 8 Hz. A peak detection algorithm was implemented to identify the maxima and minima of the two signals. Lastly, the same filter, but with a cutoff frequency of 4 Hz, was also utilized for the GSR signal.

Starting from the ECG signal, RR time series were extracted by considering the temporal distance between two consecutive R-peaks of the QRS complex. Similarly, PP time series were extracted by considering the temporal distance between two consecutive minima of the PPG waveform, detected using both red and infrared wavelengths [103].

Before performing frequency domain analysis, physiological time series were preprocessed applying a high-pass AR filter (cut-off frequency of 0.0156 Hz) and normalizing to zero mean and unit variance. In this work, the non-parametric Blackman-Tukey method has been implemented to obtain the power spectrum of the time series [157], and the LF and high-frequency HF power contents were evaluated by integrating the distribution in the ranges 0.04-0.15 Hz and 0.15-0.4 Hz, respectively. These power values have been used to obtain the ratio between the LF and HF contents. The algorithms and methods described in Chapter 2 were implemented in the form of code snippets and dedicated functions so that, once the filtering procedures are completed, the analysis of the signals and the extraction of the corresponding physiological indices can be performed.

CHAPTER 4

RESULTS AND DISCUSSION

4.1 OVERVIEW AND STRUCTURE OF THE CHAPTER

In this chapter, the results of the research conducted within the scope described by the thesis are collected and presented. This is done by dividing the chapter into four sections that discuss the results obtained using the methods introduced in the Chapter 2, implementing data analysis algorithms on biosignals recorded employing commercial biomedical devices, portable devices developed in the laboratory during the Ph.D. research period and, finally, the realized ring-shaped wearable system herein presented. In detail, it will be discussed: the implementation of ST and UST analyses on cardiovascular series, the extraction of the respiratory signal from the PPG signal, the acquisition of the GSR signal and its use for discriminating stressful situations, and finally, the use of the realized wearable device for detecting changes in physiological states.

Each subsection follows a predefined structure, consisting of an initial part where the aim is defined and the work is briefly described. Subsequently, an experimental protocol section clarifies to the reader the type of biomedical data acquired and the methods (i.e., the measurement protocol used, together with the instrumentation used, if different from the already described wearable device). This is followed by the results section, where the findings of the conducted analyses are presented, and finally, the discussion of the results. If not specified, the processing data analyses are carried out using the same methodology described in the Methods section of Chapter 2 and in the offline data processing paragraph of Chapter 3.

As the UST analysis proves to be of fundamental importance in the application context of wearable devices, it was deemed appropriate to dedicate a significant portion of the research to its implementation.

For this reason, a significant effort was made to compare the HRV indices computed through UST analysis to those achieved through ST standard reference, using an existing database that also includes levels of arterial BP, which, although not thoroughly described as a signal in this work, has proven to be very useful to analyze and is therefore presented alongside the analysis of other physiological signals of interest. Once the UST analysis for the detection of physiological states was validated, it was implemented again on the data acquired by the developed wearable device to confirm the previously obtained results.

4.2 FEASIBILITY OF ST AND UST ANALYSIS ON CARDIOVASCULAR VARIABILITY SERIES FOR ASSESSING PHYSIOLOGICAL STATES

Herein, a comparison between UST and ST indices extracted in the time and information domains is performed on a dataset composed of systolic arterial pressure (SAP) and RR time series acquired on a population of healthy subjects in rest and when undergoing orthostatic and mental stress. In this case, the acquisitions of both signals were made using commercial biomedical instrumentation, the same type typically found in hospital environments and used by specialized personnel for patient monitoring and vital function assessment. While such instrumentation offers the significant advantage of having been widely used and certified for biomedical and clinical measurements, it still poses the major limitation of the invasiveness of measurements (as in the case of the ECG signal) and the overall bulkiness (i.e., weight and size) of all the equipment, such as electrodes, sensors, cables, and central computers for signal analysis and display. On the other hand, this is precisely one of the main themes addressed in this thesis. For this reason, it was deemed important to firstly implement the data analysis algorithms on biosignals extracted from commercial biomedical equipment, in order to subsequently use the obtained results as a reference to confirm the same findings on the data analyses performed from the acquisitions of the wearable device, as will be reported later in this chapter.

Standard cardiovascular variability time-domain indices are computed, together with entropy-based measures able to assess the regularity and complexity of cardiovascular dynamics, employing either a faster linear parametric estimator or a more reliable but time-consuming model-free method based on nearest neighbor estimates, which from now on are called *lin* and *knn* estimators, respectively.

Indeed, the present work aims at evaluating the extent to which the loss of physiological information due to UST reduced time series length can represent a good tradeoff for extracting physiological indices with lower real-time processing and storage costs, suitably for wearable devices. Moreover, while several works have focused on ultra-short-term HRV [57], [119], [158], [159], there are no previous studies performing a UST blood pressure variability analysis.

The analysis has been carried out by reducing the time series length from 300 (short-term, ≈5 min) to 60 samples (≈1 min), in steps of 60, to assess the loss of information at decreasing window length and to verify whether the shortest length is still able to discriminate the transition from rest to stress.

4.2.1 EXPERIMENTAL PROTOCOL

Analyses were carried out on a historical dataset belonging to Comenius University and previously employed for assessing the effects of orthostatic and mental stress on cardiovascular dynamics. Data have been acquired from 61 healthy young volunteers (24 males, 37 females) aged 17.5 years ±2.4 years, normotensive, and with a normal body mass index (BMI = 19 ÷ 25 kg m^{-2}) [160], [161]. All participants signed a written informed consent form before taking part in the study, also requiring a parental or legal guardian permission to participate in the study when the subject was a minor (i.e., less than 18 years of age). All procedures were approved by the Ethical Committee of the Jessenius Faculty of Medicine, Comenius University, Martin, Slovakia.

Subjects were asked not to take substances influencing the autonomic nervous system and cardiovascular system activities [160], [161]. Physiological signals recorded on the volunteers consisted of (i) ECG signal acquired through a horizontal bipolar thoracic lead (CardioFax ECG-9620, NihonKohden, Tokyo, Japan), (ii) continuous arterial blood pressure recorded on the finger through the volume-clamp method (Finometer PRO, FMS, Amsterdam, The Netherlands). The first device, indeed, allows for ECG signal acquisitions using wired electrodes, which are placed in contact with the skin by means of clips (peripheral ECG) and adhesive electrodes (precordial ECG). The second one, on the other hand, enables non-invasive acquisition of arterial pressure using a clip worn on the subject's index finger.

Both instruments are then connected via cables to a central computer, which facilitates data processing and real-time display of biosignals waveforms and main extractable indices. All signals were acquired synchronously with a sampling frequency of 1 kHz.
Subjects were positioned on a motorized tilt table and a restraining strap was placed at the thigh level to ensure the safety and stability of the subject during the movement of the tilt table. Signals were acquired during a measurement protocol consisting of the following four phases, schematically represented in Figure 4.1a:

- A resting condition (R1) with the subject laying in the supine position for 15 min, in order to stabilize the physiological signals on a baseline level;
- A head-up tilt (T) test aimed at evoking mild orthostatic stress by inclining the motorized table by 45 degrees for 8 min;
- Another resting condition (R2) with the subject laying in the supine position for 10 min, in order to restore the physiological parameters to their baseline values;
- A 6 min long mental arithmetic (M) task aimed to evoke cognitive load (i.e., mental stress), during which subjects were asked to mentally calculate the sum of three digits in the shortest possible time, indicating whether the result was an even or odd number.

During the whole measurement protocol, the subjects were asked to avoid any movement or speaking, to decrease artifacts occurrence and minimize the non-stationarities during recording of the signals.
Initially, time series of 300 heartbeats were extracted according to the standard of short-term analysis. The time series duration varied in the different conditions according to the heart rate, being on average $\approx$4.5 min during rest conditions, 3.5 min at T, and 4 min during M. Afterwards, in order to perform UST analysis of cardiovascular parameters, shortened time series were obtained by reducing the series length each time of 60 samples down to a minimum of 60 heartbeats. The resulting UST time series were composed of 240, 180, 120, and 60 samples, selected starting from the beginning of the reference ST series, as schematized in Figure 4.1b.

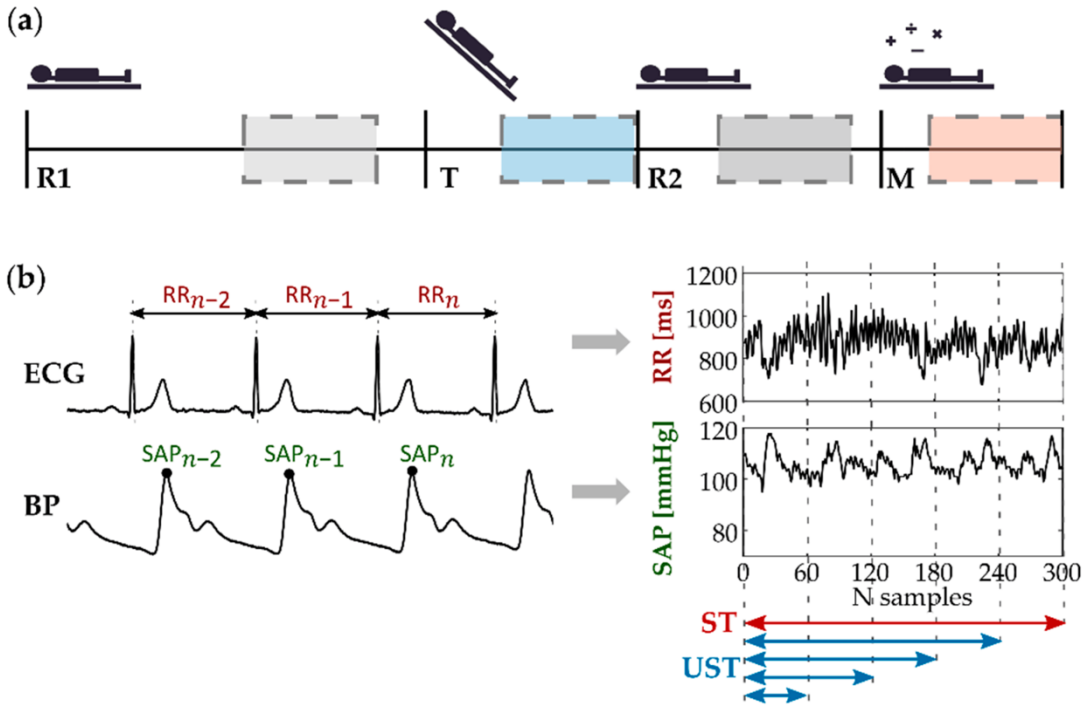

Figure 4.1 *– **(a)** Schematic illustration of the experimental protocol, including baseline resting (R1), orthostatic stress (T), second resting (R2) and mental stress (M). Dashed boxes indicate the windows taken into account with regard to short-term (ST, 300 points) analysis. **(b)** Representative RR and SAP time series, extracted respectively from ECG and BP recordings, which have been investigated through univariate analysis performed after ST (red arrow) and ultra-short-term (UST, 240 to 60 points, blue arrows) time window segmentation.*

4.2.2 STATISTICAL ANALYSIS

Sstatistical analyses have been carried out on distributions of time–domain and entropy measures obtained in the four phases (R1, T, R2, M) on both RR and SAP time series. Given that the normality of distributions for the analyzed indexes was verified according to the Kolmogorov–Smirnov test, the parametric Student's *t*-test was used to perform the pairwise comparisons, with a significance threshold set to $p<0.05$. Specifically, the statistical tests were carried out to compare (i) orthostatic and mental stress conditions with the preceding resting states (i.e., T vs. R1 and M vs. R2) and (ii) ultra-short-term and short-term distributions (i.e., UST vs. ST).

However, the mere use of statistical tests has often been considered not sufficient for assessing the feasibility of the use of HRV indices evaluated through different techniques in studies where statistical tests have been complemented by other approaches, e.g., correlation analysis, Bland-Altman plots, or effect size [31], [119], [162], [163]. In this work, correlation analysis was carried out through the computation of the squared Pearson correlation coefficient r^2 [164] to evaluate the strength of the linear relationship between each UST and the ST reference distribution, in order to quantify to what extent their agreement decreases when reducing the time series length. According to Shaffer et al. [118], [158], who selected a conservative criterion for the Pearson correlation coefficient ($r \geq 0.90$), herein is set a threshold for the squared coefficient equal to $r^2 = 0.81$ to establish the presence of a strong agreement between indexes derived from UST and ST analysis.

Moreover, for all the time and information domain indices and time series length, it has been assessed the difference between the distributions during stress and during rest by computing the effect size. Measures of effect size represent a widely employed and useful tool to describe the strength of the association between two distributions, providing a description of the size of observed effects possibly independent of misleading influences on sample size, and thus can complement statistical tests that instead assess significance [165]. Large but nonsignificant effect sizes may indeed suggest that other statistical tests with greater discriminatory power should be employed, while small but significant effects due to large sample sizes can be indicative of overvaluing the observed effect. In this thesis, the effect size has been evaluated through the Cohen's *d* measure as the difference between the means of the two distributions divided by the pooled standard deviation [166].

Generally, the effect size is deemed as small, medium, and large, if the absolute value of d is lower than 0.2, between 0.2 and 0.5, or higher than 0.8, respectively. The Cohen's d has been computed between stress and rest conditions (i.e., T vs. R1 and M vs. R2) for each time series length, in order to quantify whether and to what extent the strength of the relationship between the two distributions changes if compared to the ST reference.

4.2.3 RESULTS

Figure 4.2 shows the comparison of ST (N = 300) and UST (N < 300) analyses performed for the time-domain indexes (MEAN, SDNN, RMSSD) computed over the RR time series across the 61 subjects in the four considered phases. For each panel, the top row subplot shows the boxplot distributions of the indices, the central one being the Cohen's *d* measure (in absolute value), and the bottom one being the Pearson squared correlation coefficient. Results show a statistically significant decrease of all the three indexes during T vs. R1 and during M vs. R2 phases for the ST and for all the UST time window lengths taken into account. With regard to MEAN, statistically significant differences between UST and ST distributions are reported only for R2 already from N = 240 and for shorter time series (Figure 4.2(a2), top subplot). As regards SDNN, statistically significant differences have been detected comparing all the UST distributions to ST reference during head-up tilt (Figure 4.2(b1), top subplot).

On the contrary, statistically significant differences have been reported only in the shortest UST distribution (N = 60) for both R2 and M (Figure 4.2(b2), top subplot). No statistically significant differences have been reported for RMSSD. Cohen's *d* measures (central subplots in Figure 4.2) computed between stress and rest reported a medium-to-high effect size ($|d| \geqslant 0.7$) for all the three indices, but lower for RMSSD during mental stress ($|d| \approx 0.5$). Moreover, in all the cases the Cohen's d showed higher values with regard to postural stress discrimination rather than mental stress. Furthermore, d remains almost constant at decreasing time series length, except for SDNN assessed during mental stress (Figure 4.2(b2)), in which it decreases with N. The squared Pearson correlation coefficient (bottom panels in Figure 4.2) computed between ST and UST distributions is very high and almost always above the threshold (r^2>0.81) for MEAN and RMSSD indices for all the time window lengths, except for RMSSD during T for N = 60.

A considerable decrease in the correlation is reported for the SDNN index, going below threshold for T when N = 120 (Figure 4.2(b1), bottom panel), and for both R2 and M when N = 60 (Figure 4.2(b2), bottom panel).

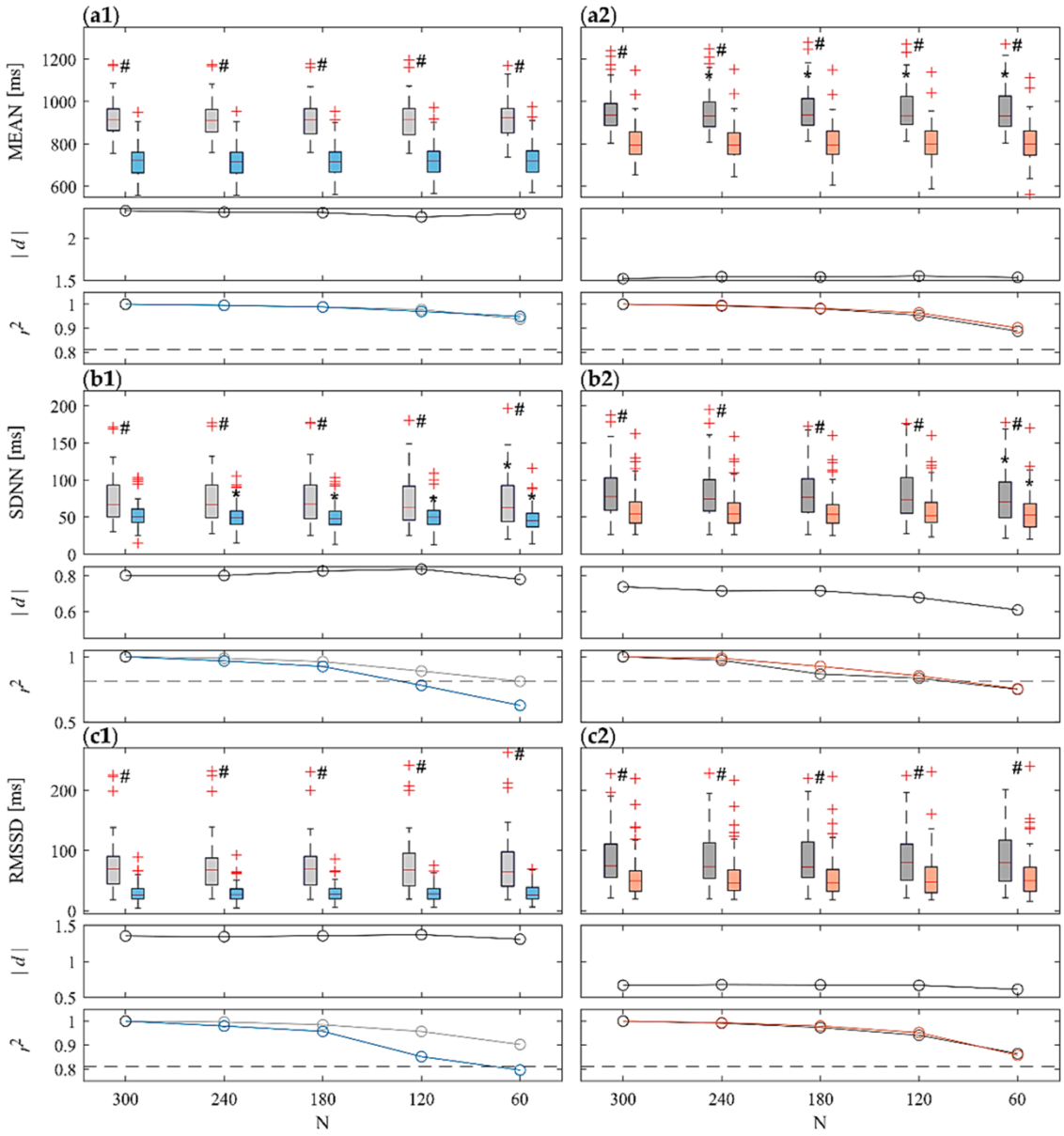

Figure 4.2 *– Boxplot distributions (top subplots) of time-domain indexes, i.e.,* ***(a)*** *MEAN,* ***(b)*** *SDNN and* ***(c)*** *RMSSD calculated from RR time series during R1 (light gray) and T (light blue), (.1 panels), and during R2 (dark gray) and M (orange) (.2 panels) phases. Statistical tests: #, $p < 0.05$, T vs. R1 or M vs. R2; *, $p < 0.05$, ST vs. UST. Central subplots: Cohen's d (in absolute value) evaluated between each stress condition and the previous rest phase (i.e., R1-T and R2-M) for all the considered time series lengths. Bottom subplots: squared Pearson correlation coefficients computed between a given UST distribution and the ST reference, with a threshold of $r^2=0.81$ (dotted gray line).*

Figure 4.3 shows the comparison of ST (N = 300) and UST (N < 300) analyses regarding time-domain indexes (MEAN, STD) of SAP time series across the 61 subjects in the four considered phases.

With regard to ST, MEAN decreases significantly during T if compared to R1 (Figure 4.3(a1), top subplot), while it increases significantly during M if compared to R2 (Figure 4.3(a2), top subplot); opposite trends are reported with regard to STD (Figure 4.3(b1,b2), top subplots). For both indexes, results show statistically significant differences for T vs. R1 and for M vs. R2 phases for all the UST time window lengths taken into account, except for T vs. R1 with regard to the shortest series length (N = 60) only for STD (Figure 4.3(b1), top subplot).

Regarding MEAN, statistically significant differences have been reported comparing UST vs. ST distributions during head-up tilt condition for N = 240 and shorter (Figure 4.3(a1), top subplot); on the other hand, no statistically significant differences have been reported with regard to R1 and to both M and R2 conditions (Figure 4.3(a2), top subplot)). As regards STD, statistically significant differences have been reported comparing UST vs. ST distributions for $N \leq 120$ and $N \leq 180$, respectively, for R1 and T (Figure 4.3(b1), top subplot)), for $N \leq 240$ for R2, and for just N = 60 for M (Figure 4.3(b2), top subplot)). Cohen's d values evidence a high effect size ($|d| > 0.8$), except for STD index during R1-T transition (Figure 4.3(b1), central subplot)) in which there is a medium-low effect size ($|d| \approx 0.5$). An overall decrease in effect size is observed with the sample size N, especially for STD.

The correlation analysis between UST and ST distributions reported a high squared correlation coefficient ($r^2 > 0.81$) with regard to MEAN distributions (Figure 4.3(a1,a2), bottom subplots). On the other hand, with regard to STD, the correlation coefficient strongly decreases when shortening N, going below the threshold for N = 120 for R1, R2 and M and for N = 60 for T (Figure 4.3(b1,b2), bottom subplots)).

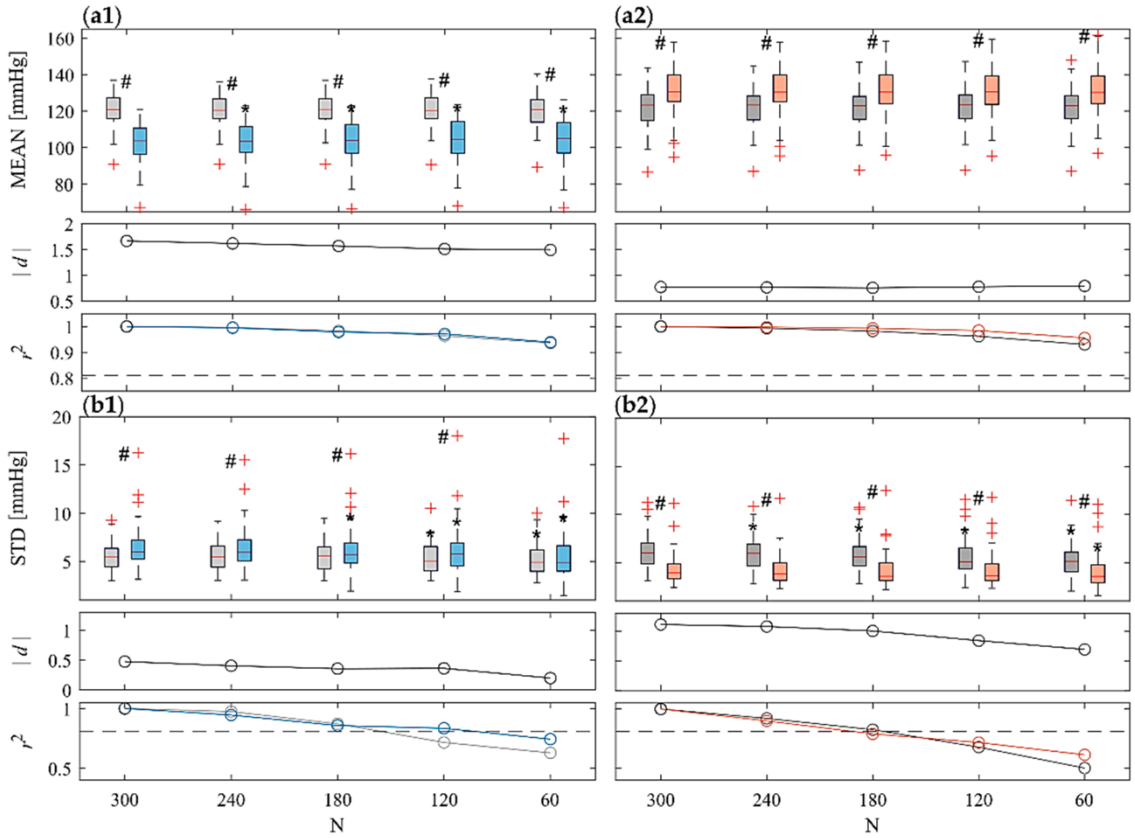

Figure 4.3 *– Boxplot distributions (top subplots) of time-domain indexes, i.e.,* ***(a)*** *MEAN and* ***(b)*** *STD calculated from SAP time series during R1 (light gray) and T (light blue), (.1 panels), and during R2 (dark gray) and M (orange) (.2 panels) phases. Statistical tests: #, $p < 0.05$, R1 vs. T and R2 vs. M; *, $p < 0.05$, ST vs. UST. Statistical tests: #, $p < 0.05$, T vs. R1 or M vs. R2; *, $p < 0.05$, ST vs. UST. Central subplots: Cohen's d (in absolute value) evaluated between each stress condition and the previous rest phase (i.e., R1-T and R2-M) for all the considered time series lengths. Bottom subplots: squared Pearson correlation coefficients computed between a given UST distribution and the ST reference, with a threshold of $r^2=0.81$ (dotted gray line).*

Figure 4.4 and Figure 4.5 depict the results of the information domain analysis carried out by computing SE, DE, and CE indices through both *lin* and *knn* estimators for RR and SAP time series, respectively, across the 61 subjects for each of the four physiological conditions (R1, T, R2 and M). For each panel, the top row subplot shows the boxplot distributions of the indices, the central one the Cohen's d measure (in absolute value), and the bottom one the Pearson squared correlation coefficient.

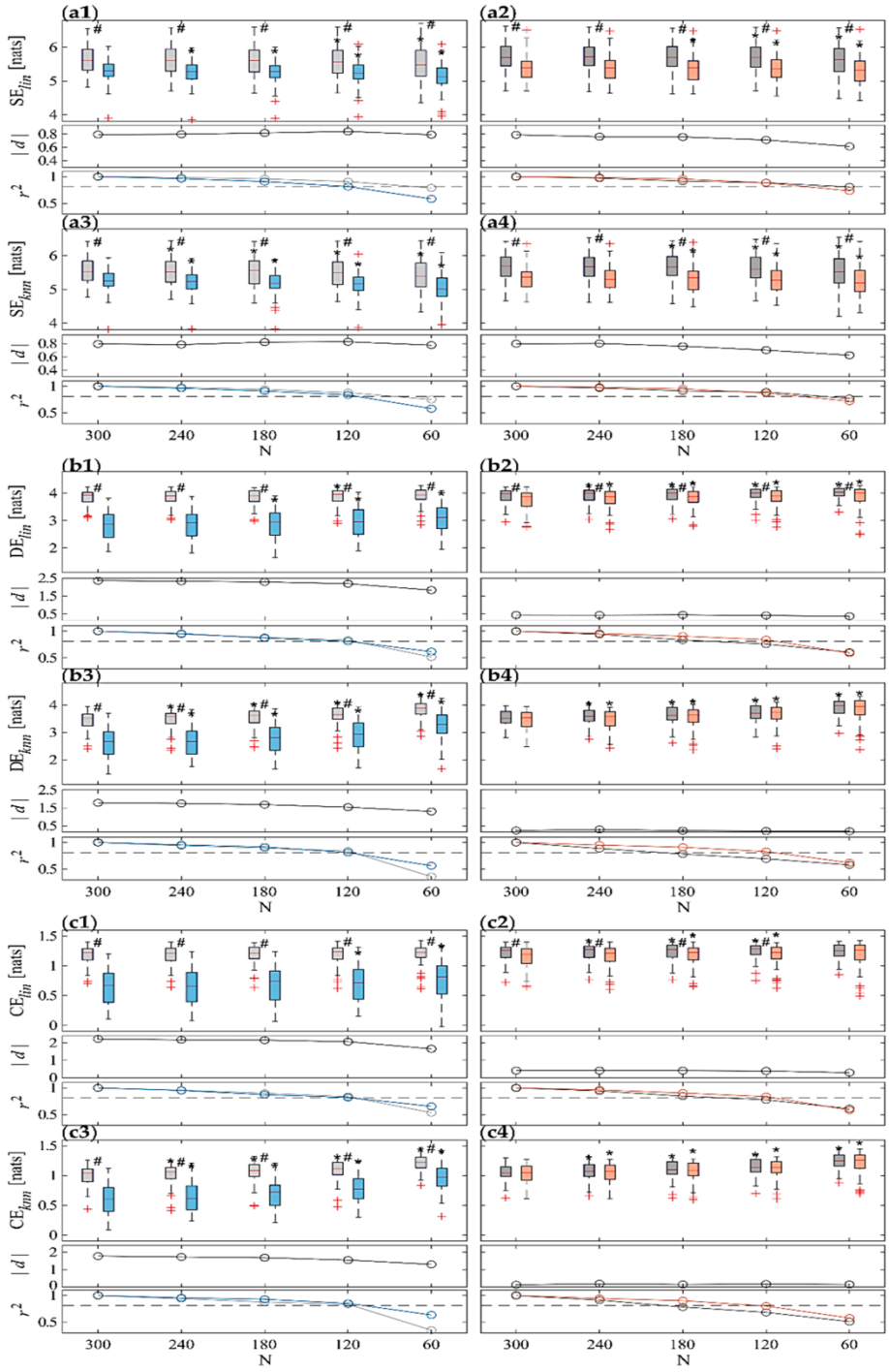

Figure 4.4 *– Results of information domain analysis on RR time series. Boxplot distributions (top subplots) of ST and UST indices of* ***(a)*** *SE,* ***(b)*** *DE and* ***(c)*** *CE calculated using both lin (.1 and .2) and knn (.3 and .4) estimators during R1 (light gray) and T (light blue) (.1 and .3), and during R2 (dark gray) and T (orange) (.2 and .4) phases. Statistical tests: #, $p < 0.05$, T vs. R1 or M vs. R2; *, $p < 0.05$ ST vs. UST. Central subplots: Cohen's d (in absolute value) evaluated between each stress condition and the previous rest phase (i.e., R1-T and R2-M) for all the considered time series lengths. Bottom subplots: squared Pearson correlation coefficients computed between a given UST distribution and the ST reference, with a threshold of $r^2=0.81$ (dotted gray line).*

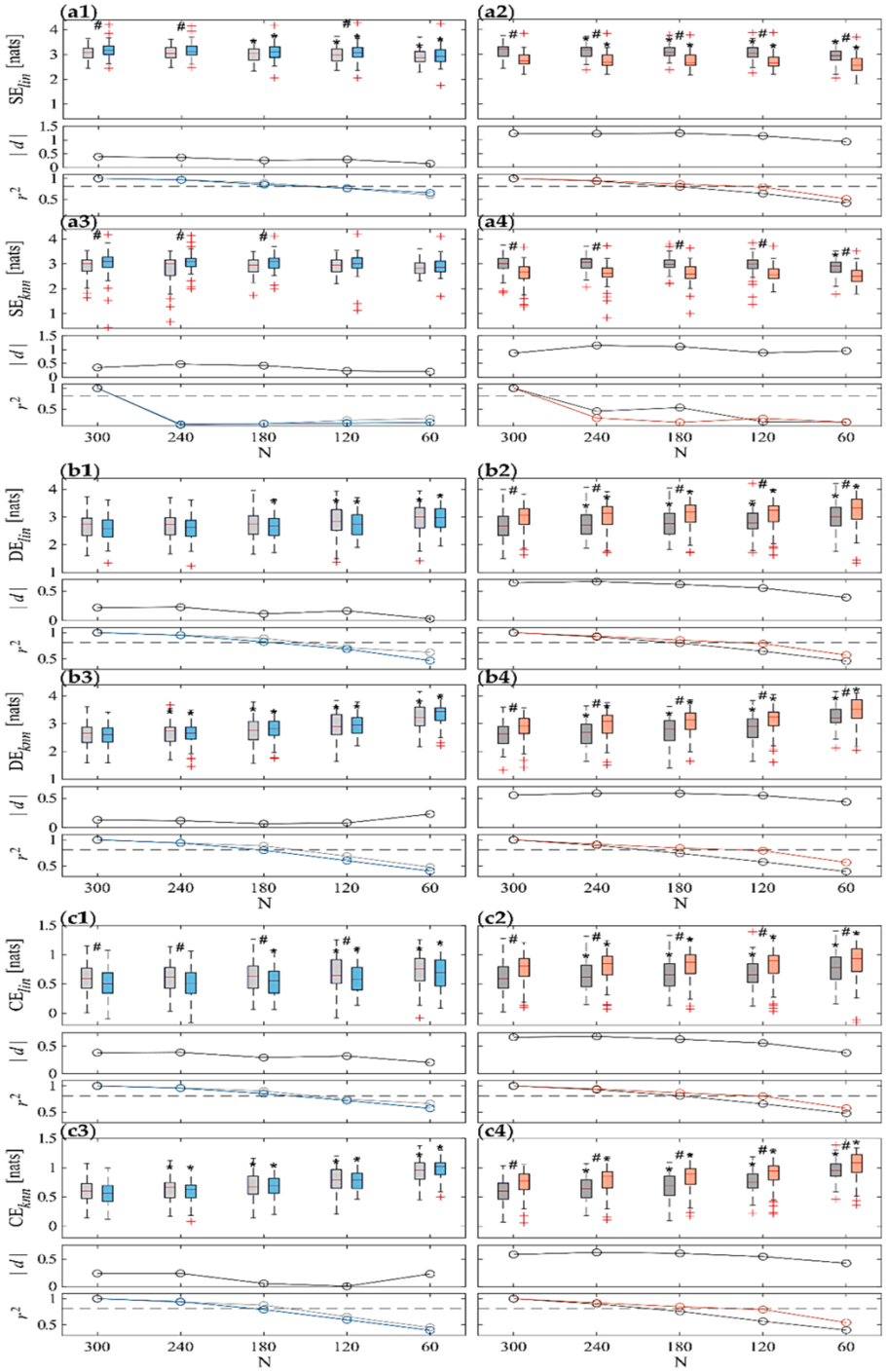

Figure 4.5 *– Results of information domain analysis on SAP time series. Boxplot distributions (top subplots) of ST and UST indices of* ***(a)*** *SE,* ***(b)*** *DE, and* ***(c)*** *CE calculated using both lin (.1 and .2) and knn (.3 and .4) estimators during R1 (light gray) and T (light blue) (.1 and .3), and during R2 (dark gray) and T (orange) (.2 and .4) phases. Statistical tests: #, $p < 0.05$, T vs. R1 or M vs. R2; *, $p < 0.05$ ST vs. UST. Central subplots: Cohen's d (in absolute value) evaluated between each stress condition and the previous rest phase (i.e., R1-T and R2-M) for all the considered time series lengths. Bottom subplots: squared Pearson correlation coefficients computed between a given UST distribution and the ST reference, with a threshold of $r^2=0.81$ (dotted gray line).*

The results of the analyses carried out on RR time series are shown in Figure 4.4. For both orthostatic and mental arithmetic conditions, the shift from rest to stress highlights significant decrease of SE, DE and CE measures computed with both *lin* and *knn* estimators. This variation is most appreciable under the postural stress, in fact statistically significant variations are always reported comparing T vs. R1, for both ST and all the UST distributions and for both estimators. On the other hand, using the *lin* estimator statistically significant variations are reported comparing M vs. R2, for both ST and almost all the UST distributions for all measures (except with regard to CE for N = 60), but only for SE (Figure 4.4(a4)) using the *knn* approach. SE appears to decrease while CE and DE tend to increase when decreasing the time series length N. This result is more evident using the *knn* estimator, in fact statistical analysis carried out between UST and ST distributions highlighted significant differences starting from time series of length N = 240 for almost any measure computed through the model-free approach. For DE and CE computed through *lin* estimator, the statistically significant differences between UST and ST at T occur only for $N \leqslant 180$ and $N \leqslant 120$, respectively.

The Cohen's d values obtained for *lin* estimator are higher than for the *knn* one (see central subplots in each panel in Figure 4.4). High effect sizes are reported for CE and DE during T, but medium values instead during M; with regard to the SE index, a medium-high effect size is assessed for both physiological state changes and for both estimators. In any case, d appears almost constant at decreasing N (down to N = 120), while a more marked decrease is observed when going to N = 60. Finally, the squared Pearson correlation coefficient (see bottom subplots in each panel in Figure 4.4) decreases, shortening the time series length N, and still largely shows a high degree of correlation (above the threshold) down to N = 120.

As regards entropy measures computed on the SAP time series reported in Figure 4.5, both estimators (i.e., *lin* and *knn*) and analysis approaches (i.e., ST and UST) show an increase in SE (Figure 4.5(a1,a3), top subplots) as well as a decrease in DE (Figure 4.5(b1,b3), top subplots) and CE (Figure 4.5(c1,c3), top subplots) from R1 to T, and, conversely, a decrease in SE (Figure 4.5(a2,a4), top subplots) and an increase in DE (Figure 4.5(b2,b4), top subplots) and CE (Figure 4.5(c2,c4), top subplots) from R2 to M.

Nevertheless, while differences between M and R2 distributions are always statistically significant, the comparison between T and R1 evidenced statistical significance only for *lin* estimation of CE using time series no shorter than 120 samples, and for SE obtained with both estimators and N $\leqslant$ 240. Regarding the comparison between ST and UST analyses, for both estimators and physiological state changes, CE and DE values increase as the time series length decreases, whereas the SE decreases more slowly. Statistical analysis highlighted significant differences already from the first window length (N = 240) for almost all the information indices obtained with both estimators during R2 and M, while overall this is true for T vs. R1 in any cases only for shorter time series (N < 180). The only exception is the *knn* estimation of SE, for which no significant differences are found between ST and UST analysis. The effect size assessed through Cohen's d (Figure 4.5, central subplots in each panel) is always medium-low, except for SE index for M vs. R2, and overall decreases in absolute value when shortening the series length. The correlation analysis between UST and ST distributions (Figure 4.5, bottom subplots in each panel) shows that the squared Pearson's correlation coefficient decreases when reducing time series length, still reporting values higher than the threshold (r^2=0.81) for almost all indices for N $\geqslant$ 180 (often even for N = 120), except for the SE estimated with the *knn* approach, for which r^2 severely drops already for N = 240 (Figure 4.5(a3,a4), bottom subplots).

Finally, it has been reported the results relevant to the computational times required for the calculation of the entropy-based measures, performed using both estimators. In order to compare ST and UST analysis times, we have selected N = 120 samples as UST time series length, since the previous results highlighted that this is the minimum length which overall guarantees a very good agreement between ST and UST distributions. The average computation time of all the entropy measures on 488 iterations (two time series in four different physiological conditions for 61 subjects) was 0.24 ms and 5.87 ms for *lin* and *knn* on ST 300-samples time series, respectively, and 0.17 ms and 1.90 ms on UST 120-samples time series. Such computational times were obtained on a computer equipped with an Intel Core i7-11700K CPU (3.60 GHz), 64 GB RAM, 512 GB SSD, Windows 11, MATLAB R2021b. The computational times are similar for RR and SAP series and do not vary as well with the protocol phase. Moreover, while computational times remain almost constant as time series length decreases with regard to *lin*, they strongly decrease at shortening N with regard to model-free estimation.

4.2.4 DISCUSSION

Time-domain HRV results (Figure 4.2) are in agreement with widely recognized findings in the literature which evidence an increased heart rate and a decrease of variability (SDNN) and RMSSD during stress conditions, in particular after head-up tilt [31], [167], [168]. In both stress conditions, but less markedly during mental stress, these trends are related to an enhanced sympathetic and reduced parasympathetic activity, resulting from an SNS activation and a PNS withdrawal which cause a shift in the sympathovagal balance [168], [169], [170]. In particular, the reduced parasympathetic contribution is evidenced by the decreased RMSSD (Figure 4.2(c1,c2)) which has been usually related to PNS activity [49], [106]. Nevertheless, physiological mechanisms involved during orthostatic and arithmetical stress are different, as demonstrated by the different SAP MEAN and STD trends in these two stress conditions (cf. Figure 4.3(a2) vs. Figure 4.3(a1) and Figure 4.3(b2) vs. Figure 4.3(b1)). This is in agreement with previous studies highlighting the presence of a closed-loop regulatory mechanism between RR and SAP [105], [171], [172]. The decrease of the mean SAP together with the increase of its variability during postural stress (Figure 4.3(a1,b1)) have been related to the decreased venous return [173], [174], [175]. The resulting cardiac filling associated with SAP decrease leads to baroreflex activation and to vasoconstriction during postural stress, which in turn produce an increased heart rate [173], [174], [175], [176]. The opposite trends reported for mental stress (cf. Figure 4.3(a2) vs. Figure 4.3(b2) can be related to cortical mechanisms eliciting vasomotor reactions and are reflected by SAP changes [168], [177], [178].

The shift of the autonomic balance to the sympathetic branch caused by orthostatic and cognitive challenges produces a simplification of the cardiac dynamics, with reduced information contained in the RR time series (Figure 4.4(a1-a4)), which has been linked to the emergence of oscillations at the frequency of the Mayer waves [31], [161]. The elicited stress conditions lead also to a decrease in complexity, and thus lower CE and DE values using both linear and non-linear estimators (Figure 4.4(b1-c4)). Physiologically, this indicates a regularizing effect on the cardiac dynamics produced by sympathetic activation and vagal withdrawal already demonstrated in several previous works also on the same dataset [31], [110], [125], [179], [180].

The entropy-based SAP analysis revealed opposite trends for T and M compared to the preceding resting condition (cf. Figure 4.5 right vs. left panels), confirming the different response to postural and mental stress. Mental challenge produced an SE decrease and increased complexity, while opposite trends have been observed for postural stress. These findings evidence that SAP dynamics are less affected by orthostatic stress than by cognitive load. Physiologically, this can be ascribed to the larger involvement of upper brain centers in controlling the vascular dynamics and resistance associated with sympathetic activation. A relatively complex pattern of vascular resistance changes results in an augmented SAP dynamical complexity, as demonstrated by previous works [125], [161], [177], [180], [181]. The trend towards lower SAP complexity values during tilt may be related to the synchronization of peripheral vascular activity due to sympathetic activation, contributing to regularizing the fluctuations of SAP [182].

Comparing the entropy measures obtained through the two estimators, it has been found lower values using *knn* than using the *lin* approach, especially with regard to RR and under rest and mental stress conditions. The reasons of such a difference are difficult to explain and may be related to several factors, ranging from local nonlinearities or nonstationarities to bias effects evident especially for the *knn* estimator and due to the difficulty of working on high-dimensional spaces [183]. Nevertheless, for the majority of measures both estimators exhibit concordant changes and are equally able to distinguish between rest and stress conditions. There are three exceptions, in which the *knn* is unable to detect differences, while *lin* does, i.e., CE for RR comparing M vs. R2 (Figure 4.4(c4) vs. Figure 4.4(c2)), DE for RR comparing M vs. R2 (cf. Figure 4.4(b4) vs. Figure 4.4(b2)), and CE for SAP comparing T vs. R1 (cf. Figure 4.5(c3) vs. Figure 4.5(c1)). The augmented discriminative capability of the linear estimator, even if possibly related to the presence of non-linear dynamics [184], [185] which are not properly taken into account, may be a perspective used in practical applications for a more accurate and fast differentiation between rest and stress conditions [159], [180]. This is also reinforced by the very low computational times required for the *lin* estimator to compute the entropy-based measures on 300-sample series length (ST standard), which is 24 times lower if compared to *knn*.

Regarding the reliability of using UST RR time series to discriminate between stress and rest conditions, the obtained time-domain results (Figure 4.2) demonstrate that, overall, it is possible to make use of 60-sample recordings to detect the presence of either postural or mental stress compared to a rest condition.

This is true despite the fact that statistically significant differences between UST and ST series are detected in R2 with regard to MEAN, and in T with regard to SDNN even for 240-sample time series (Figure 4.2(a2,b1)). Therefore, the results suggest that, while UST analysis implies a significant deviation of the analyzed metrics from their ST level, such deviation does not significantly impair the capability to detect the response to stress even when working with shorter time series.

The above-discussed results are reinforced by correlation analysis, which reported squared Pearson correlation coefficient always above the adopted threshold for strong correlation, with the only exception being SDNN computed for N = 60. Analogous remarks can be made starting from Cohen's d analysis between stress and rest conditions, with similar values for all-time series lengths, with only a noticeable decrease for N = 60. Such results are in agreement with previous studies in the literature on RR series reporting a good agreement between UST and ST both under physical stress [115], [186] and mental stress [57], [187] conditions. However, the agreement decreases during the execution of a task or in the presence of a stressful event that carries dynamicity in the control mechanisms [58], [118], [162], similar to the trends reported in our results with regard to squared Pearson correlation coefficient. A number of studies applying UST analysis to physical stress conditions focus on the following recovery phase, showing that the dynamics are strongly influenced by the intensity of the task and the response time of SNS and PNS [115], [188]; this may explain the statistically significant differences found in R2 with regard to MEAN, being R2 a post-postural stress rest.

A quite common finding in previous works is that the SDNN index exhibits a lower agreement if computed through UST RR series [162], [189], and this is confirmed by my results analyzing the trend of the correlation coefficient (Figure 4.2(b1,b2), bottom subplots). On the other hand, the agreement is higher with regard to RMSSD index (Figure 4.2(c1,c2), bottom subplots). This finding appears to be directly related to the definition of metrics, since whereas SDNN reflects RR total power, the RMSSD is instead related only to the fastest variations (i.e., vagally-mediated ones) observable even from shorter time series [106]. Although it is not possible to refer to previous studies, the results obtained with regard to SAP (Figure 4.3) can be discussed similarly to RR. In particular, results highlight the capability of using UST SAP time series to discriminate between stress and rest conditions down to N = 60 (with the exception of STD for postural stress), even if statistically significant differences are reported between UST and ST distributions for MEAN during T and for most conditions for STD.

Similarly to RR, a very high squared Pearson correlation coefficient is reported between UST and ST distributions, decreasing with N and going below threshold for N $\leqslant$ 120 for STD. Likewise to RR, the agreement of the STD measure is lower for UST series, which is also confirmed by the lower effect size between the rest and stress conditions.

Our results confirmed the feasibility of employing UST series to carry out computation of regularity and complexity measures (Figure 4.4 and Figure 4.5), already previously reported for CE and Approximate Entropy [57], [159], [190]. Results of statistical tests evidence that, apart from a couple of exceptions, the significant differences between the stressful and the preceding rest conditions reported using 300-sample recordings are also retained for all the analyzed metrics (SE, DE, CE) with shorter series down to a 60-sample duration. However, the results of correlation analysis have evidenced that the agreement between UST and ST distributions is overall very good (i.e., above threshold) only for N $\geqslant$ 120 for RR and for N $\geqslant$ 180 for SAP, except for non-parametric SE that already exhibits a severe decrease of r^2 from 4 min length recordings. The results of RR analyses are in agreement with some previous studies employing other non-linear measures for the analysis of predictability (e.g., Shannon Entropy [57], [118]), dynamics (e.g., Permutation Entropy [191]), and complexity (e.g., Approximate Entropy and Sample Entropy [57], [118], [191]), overall reporting that recordings of at least 2-3 min are necessary in order to have good consistency with respect to ST standard. The obtained results complement these findings, supporting the hypothesis that the variation in cardiovascular dynamics and the complexity produced by a physiological state change can be properly assessed using even shorter recordings (60 samples), but at the cost of a lower correlation with ST reference. Moreover, the lower correlation found for SAP in my analyses suggests that slightly longer recordings may be instead envisaged when performing UST blood pressure variability if compared to HRV.

The Cohen's d analysis on entropy measures evaluated on RR evidenced a better discrimination of postural stress than mental stress with a higher effect size (Figure 4.4, central subplots), in contrast to what is evidenced instead with regard to SAP (Figure 4.5, central subplots). In any case, the effect size decreases when shortening the time window length, thus suggesting a lower discriminative capability between stress and rest states caused by the information loss about slower dynamics due to the shorter time series.

Finally, regarding the comparison of estimation methods for entropy-based measures, the same considerations previously made also hold for the UST analysis. For the majority of measures, both estimators are similarly capable of distinguishing between rest and stress conditions. There are the same three exceptions discussed with regard to ST series, in which the *knn* is unable to detect differences while *lin* can, i.e., CE for RR comparing M vs. R2 (Figure 4.4(c4) vs. Figure 4.4(c2)), DE for RR comparing M vs. R2 (Figure 4.4(b4) vs. Figure 4.4(b2)), and CE for SAP comparing T vs. R1 (Figure 4.5(c3) vs. Figure 4.5(c1)). This may be due again to the significant proportion of nonlinear dynamics also contributing to UST HRV and cardiovascular variability [161], [185], [192] that are detected by *knn* estimator but neglected by the model-based parametric approach. Also in this case, the increased discriminative capability of the linear estimator and its lower computational costs may be exploited for discrimination between rest and stress conditions [180]. Furthermore, these results demonstrate that using shorter time series also requires reduced computational costs for both estimators, with a decrease of ~1.7 times for *lin* and ~3.1 times for *knn* when shortening the time series length from 300 to 120 samples. Computing all the information indices exploiting time series of 120 samples through the parametric estimator is ~11 times less computationally expensive than using the model-free estimator.

In conclusion, results indicate that both time-domain and entropy-based measures computed on RR and SAP series successfully distinguish between rest and stress, even with very short time series lengths, down to N = 120 or N = 60 samples in most cases. However, caution is advised when using very short UST segments, as a drop in correlation below the set threshold for the shortest windows ($N \leqslant 120$) raises concerns, especially when analyzing SAP variability. Furthermore, comparing a reliable but time-consuming model-free estimator with a linear model-based approach suggests that the latter can effectively detect changes in physiological conditions while reducing computational costs. At this regard, the combination of UST analysis with faster linear estimators for entropy-based measures holds promise for integration into wearable devices for real-time monitoring of cardiovascular parameters allowing, thus, to extract information about cardiovascular dynamics quickly and employing very short observation windows.

4.3 EXTRACTION OF THE RESPIRATION RATE FROM PPG SIGNAL AND ASSESSMENT OF CARDIORESPIRATORY INTERACTIONS

In this paragraph, the description and results of the work carried out on estimating and extracting respiratory frequency from the PPG signal are reported, using data extracted from a multiparametric biomedical system developed during the whole research period, along with the realization of the wearable device. Indeed, the path taken during these intense years of research for the development of the wearable device addressed in this thesis has been marked by the simultaneous design and implementation of other biomedical devices integrating the same sensor technology, with the aim of validating both the measurement methods and the electronic components to be subsequently integrated into the wearable device. Therefore, what has been said leads to considering the measurements taken by both devices (i.e., both portable and wearable) entirely equivalent, and consequently, the results of the analyses performed on the acquired data as well. The portable device under examination has been appropriately designed for synchronous, multiparametric, and non-invasive acquisition of ECG (both peripheral and, when necessary, also precordial), multi-channel PPG (thus facilitating multi-site acquisition such as finger and/or wrist), SC, and finally, the respiratory signal [87]. The ability to directly acquire this latter signal is of fundamental importance for understanding the reliability of algorithms for extracting the respiratory signal from the PPG signal, which will then be applied to the data acquired from the wearable device. Furthermore, the possibility of performing synchronous acquisitions of the respiratory signal and ECG also expands the horizons of biosignal analysis, allowing investigation into the joint dynamics linking the cardiovascular and respiratory systems, analyzing what are thus defined as cardiovascular interactions, reason for which it is also addressed in this work. Indeed, cardiorespiratory interactions encompass the complex relationship between the cardiovascular and respiratory systems, where each system influences and modulates the function of the other [193]. One notable aspect of this interaction is respiratory sinus arrhythmia (RSA) process, a phenomenon characterized by cyclic variations in heart rate synchronized with the respiratory cycle [50]. In particular, during inhalation, sympathetic activity increases, leading to a rise in heart rate, while during exhalation, parasympathetic activity dominates, causing a decrease in heart rate.

The synchronous acquisition of cardiac and respiratory signals in non-clinical contexts would allow to assess RSA process, to detect changes in the cardiorespiratory coupling in real-life scenarios, such as during mental stress or apneic events during sleep [193], and to predict clinically risky situations so as to avoid severe complications. Specifically, the continuous monitoring of cardiac and respiratory parameters is essential in assessing physiological control mechanisms and for an early detection of potentially pathological conditions driven by altered cardiorespiratory regulation.

Starting from the time series extracted from the signals, the strength of the causal interactions directed from the respiratory process to the heart period (HP) is assessed through Granger Causality measures [131], [132]. The final aim of this study is to prove whether and to what extent the non-invasive and cost-effective PPG technique can be used alone to assess cardiorespiratory interactions without acquiring the ECG or breathing signals.

4.3.1 EXPERIMENTAL PROTOCOL AND DATA ANALYSIS

The portable biomedical device has been employed to synchronously acquire three different signals, i.e. a two-lead ECG, the PPG signal and the respiratory signal. The four ECG electrodes were positioned according to the Einthoven's triangle on the wrists and legs; the PPG probe was positioned on the left wrist; the breath probe was placed on the nose. In particular, the breathing signal was recorded using a 10 kΩ negative thermistor (NTC) capable of detecting a voltage signal related to airflow that increases during the exhalation phase and decreases during the inhalation phase. All signals were sampled with 500 Hz sampling frequency and 24-bit resolution.

An appositely developed GUI was used to show the acquired signals in real time and to send the recorded data wirelessly via Bluetooth to a personal computer, in order to save them for the subsequent offline analyses (refer to [194], [195] for further information).

Measurements were carried out on 6 healthy subjects (3 males and 3 females; 24.3 ± 1.9 years) monitored in a sitting position and undergoing a two-phase protocol consisting, respectively in a spontaneous (SB) and controlled breathing (CB, breathing rate: 20 breaths/min, i.e. 0.33 Hz).

In order to ensure a correct execution of the paced breathing, the subjects were instructed to follow an appositely developed visual metronome application showing different colors according to the current breathing phase, i.e. inhalation/expiration (refer to [194] for further information).

Four different respiration time series were extracted and used to compute cardiorespiratory interaction measures:

(i) R_RRI: series extracted as the values of the respiration signal sampled at the times of ECG R peaks;

(ii) R_PPI: series extracted as the values of the respiration signal sampled at the times of PPG peak minima;

(iii) R_PPG_filter: series extracted as the values of the respiration signal reconstructed through the filtering approach sampled at the times of PPG peak minima;

(iv) R_PPG_EMD: series extracted as the values of the respiration signal reconstructed through the EMD technique sampled at the times of PPG peak minima.

The analysis was performed considering both lagged and instantaneous (i.e., not delayed) effects from respiration (driver process, labelled as R) to the heart period (target process, labelled as H), as the common adopted measurement convention assumes that $R(n)$, sampled at the onset of the n^{th} RRI, could have a role in determining $H(n)$ variability [196]. The time series were first pre-processed using a high-pass autoregressive (AR) filter with cut-off frequency of 0.0156 times the sampling rate f_s, the latter computed for each subject assuming the series as uniformly sampled with sampling period equal to the mean heart period ⟨HP⟩. Identification of the full and restricted models was performed via the vector least-squares approach, setting the model order p according to the multivariate version of the Akaike Information Criterion (AIC) for each subject (with maximum scanned model order equal to 8) [197].

The PSD of the respiratory process in the HF band was computed as the integral of the auto-spectrum within the HF band, normalized with respect to the total power (i.e., the integral of the spectrum alongside the whole frequency axis) and labelled as $P_2(HF)$.

To study the causal effect from respiration to the heart period, it has been computed the equation (15) of the Chapter 2 from $Y_2(n)$ to $Y_1(n)$, and labelled it as $f_{2\to1}(\bar{f})$, then integrated this spectral distribution alongside the whole frequency axis to obtain $F_{2\to1}$, and within the HF band of the spectrum, thus obtaining the value $f_{2\to1}(HF)$. The width of the HF band was determined individually for each subject by first locating the respiratory peak and then selecting the band with a width of ±0.06 Hz around such peak.

4.3.2 RESULTS AND DISCUSSION

Figure 4.6 shows an example of ECG, PPG and breathing signals synchronously acquired during the measurement protocol.

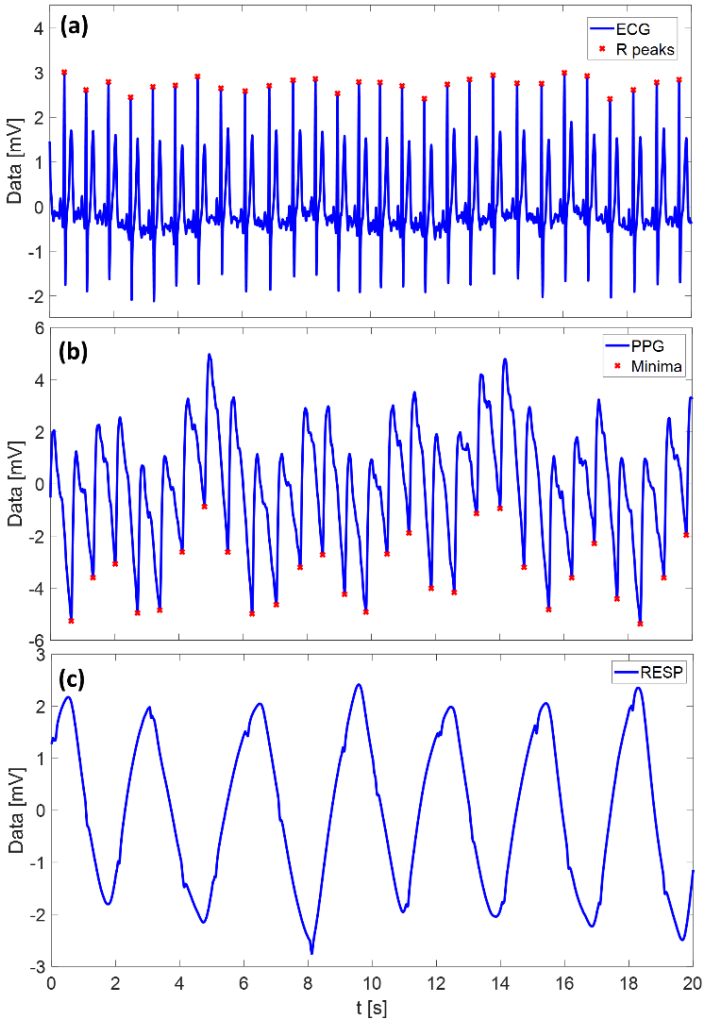

Figure 4.6 *– Examples of* ***(a)*** *ECG,* ***(b)*** *PPG and* ***(c)*** *airflow breathing signals synchronously acquired using the portable system. In* ***(a)*** *the ECG R peaks are indicated with red cross markers. In* ***(b)*** *the minima peaks are indicated with red cross markers.*

Figure 4.7(a) depicts the extraction of the breathing signal (in black) as the average of maxima and minima envelopes of PPG signal through the EMD algorithm. Figures 4.7(b) and (c) depict the breathing signals obtained after EMD and using the HF-band filtering procedure, respectively, compared to the reference airflow breathing signal acquired using the NTC (Fig. 4.7(d)).

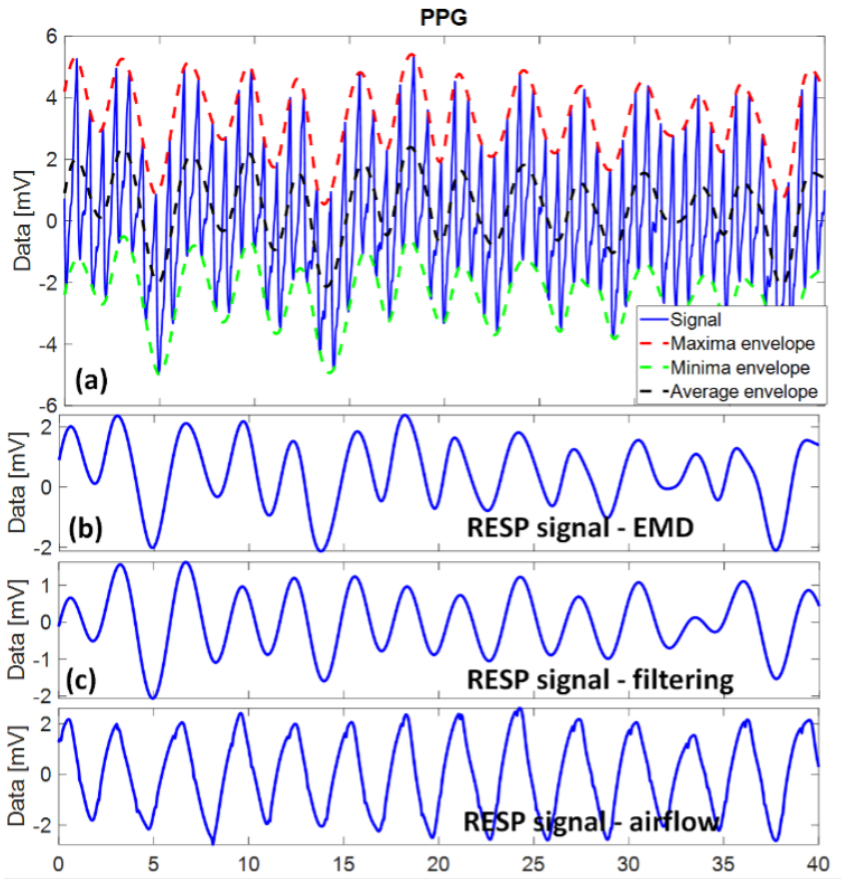

Figure 4.7 *– Reconstruction of respiration signals from the PPG waveform: **(a)** Illustration of extraction procedure through the EMD algorithm: starting from the PPG signal (blue line), the maxima (red dotted line) and minima (green dotted line) envelopes are obtained, and their average (black dotted line) represents the reconstructed breathing signal, shown in **(b)**. **(c)** Reconstructed respiration signal through band-pass filtering [cut off frequencies: 0.15-0.4 Hz]. **(d)** "True" airflow breathing signal acquired through NTC.*

Figure 4.8 shows an example of the four respiration time series extracted according to the approaches previously described, from both the acquired and reconstructed respiration signal. In detail, it has been considered as the reference the series obtained as the points in the acquired breathing signal corresponding to the timing of ECG R peaks (R_RRI), shown in Fig. 4.8(a)), while the corresponding R_PPI series is depicted in Fig. 4.8(b).

The two respiration series reconstructed only using PPG through filtering and through EMD are shown in Fig. 4.8(c) and Fig. 4.8(d), respectively. It is possible to note that the respiration series obtained sampling the airflow signal (Fig. 4.8a,b) are very similar to each other, and small differences can be observed from those obtained sampling the PPG-derived respiration signal (Fig. 4.8c,d).

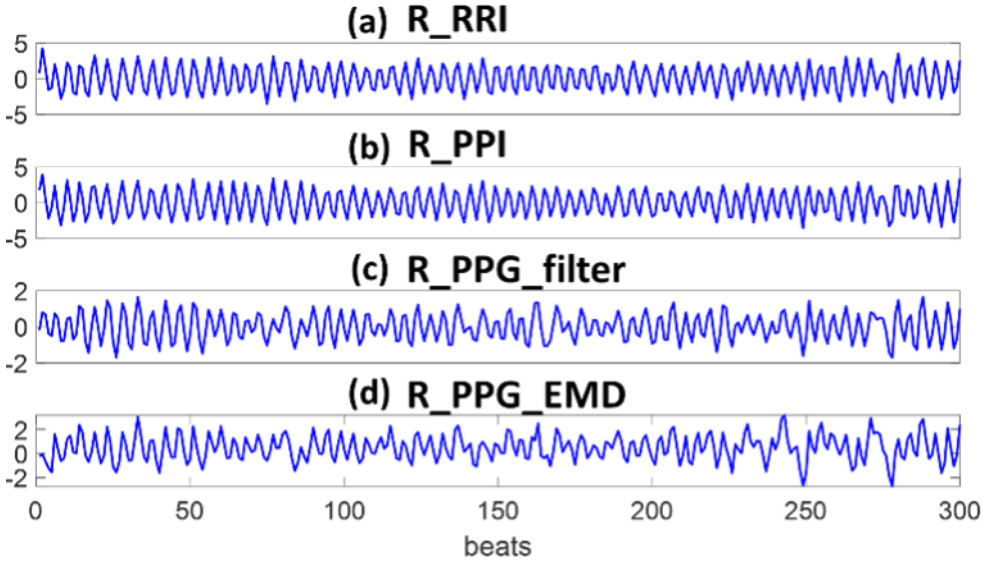

Figure 4.8 *– Example of four respiration time series extracted as the points in the acquired breathing signal corresponding to the timing of ECG R peaks (R_RRI, panel (**a**)) and of PPG peaks (R_PPI, panel (**b**)), and as the samples of the respiration signal reconstructed using the filtering approach (R_PPG_filter, panel (**c**)) and the EMD algorithm (R_PPG_EMD, panel (**d**))) also corresponding to the timing of PPG minima peaks.*

Figure 4.9 shows the subject-specific results of time domain and spectral analysis. The computed measures were the normalized PSD of the respiratory process (Fig. 4.9(a)), the time domain Granger causality (Fig. 4.9(b)) and the spectral Granger causality integrated within the HF band of the spectrum (Fig. 4.9(c)), in both phases of the protocol (panels above: SB; panels below: CB). The following combinations of respiratory and heart period time series have been analyzed:

(i) heart period: RRI time series extracted from ECG; respiratory time series: R_RRI;

(ii) heart period: PPI time series extracted from PPG; respiratory time series: R_PPI;

(iii) heart period: PPI time series extracted from PPG; respiratory time series: R_PPG_filt;

(iv) heart period: PPI time series extracted from PPG; respiratory time series: R_PPG_EMD.

Two subjects presented spontaneous breathing rates higher or lower than usual (respectively, ~0.45 Hz and ~0.1 Hz), falling out of the frequency band commonly referred to as respiratory band [0.15-0.4 Hz]. Surprisingly, it has been previously found that, in many healthy subjects, breathing frequency slows down to the LF band and entrainment of the cardiovascular rhythm around 0.1 Hz often occurs [198]. Slow breathing was found in one of the six subjects who performed the experimental protocol. This put a constraint in the selection of the HF band for the computation of spectral measures, as it has been chosen subject-specific HF ranges to take into account possible outliers.

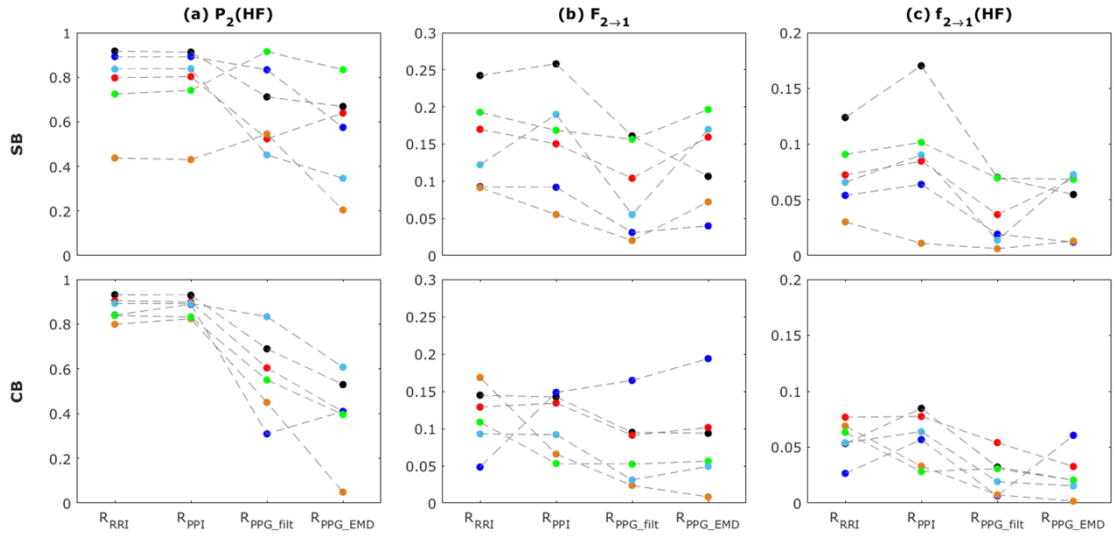

Figure 4.9 *– Results of time domain and spectral analysis on the available time series H (process 1) and R (process 2).* ***(a)*** *Normalized power spectral density (PSD) of R in the HF band of the spectrum, computed as the ratio of the PSD in HF to the total PSD.* ***(b)*** *Time domain logarithmic Granger causality from the driver process (R) to the target (H), computed as the integral of (4) alongside the whole frequency spectrum.* ***(c)*** *Spectral measure of Granger causality from the driver process (R) to the target (H), computed as the integral of (4) within the HF band of the spectrum. Measures are computed in the two phases of the protocol (spontaneous breathing, SB, panels above; controlled breathing, CB, panels below) considering the four respiration time series described in section II.B (R_RRI, R_PPI, R_PPG_filter, R_PPG_EMD) for all 6 subjects (each subject is represented by a different color).*

However, this approach may cause to fail detecting the whole power in HF band. Indeed, it has been noticed that the bandwidth around the peak is larger when reconstructing the respiration signals from PPG (i.e. R_PPI_filter and R_PPI_EMD) for both experimental conditions (SB, CB), probably due to "spurious" spectral content related to autonomic system activity not present in the "true" respiration-only signal. This may be the reason of the unexpected sudden decrease of respiratory PSD in HF when extracting RESP from PPG, both with filtering and EMD approaches, mostly visible in one of the subjects (e.g. orange point in Fig. 4.9(a)) but generally occurring for all of them in both experimental conditions. On the contrary, PSD values computed for the first two settings (R_RRI and R_PPI) are comparable between each other and expectedly slightly increase with controlled breathing, since all the respiratory variability is centered around the respiration peak (~0.33 Hz) and spectral leakage was observed to be negligible.

As regards Granger causality measures, the results suggest that their overall behaviour is characterized by a decrease when these values are computed using respiratory time series reconstructed from the PPG, especially with regard to the spectral measure (see values in Table I). Generally, in the presence of bigger databases, statistical analysis is performed to detect significant changes of the investigated measures between experimental conditions or settings.

Table 4.1 *– Time and frequency domain Granger Causality values for each of the six analyzed subjects.*

	$F_{2\to1}$								$f_{2\to1}(HF)$							
	R_RRI		**R_PPI**		**R_PPG_filter**		**R_PPG_EMD**		**R_RRI**		**R_PPI**		**R_PPG_filter**		**R_PPG_EMD**	
	SB	**CB**	**SB**	**CB**	**SB**	**CB**	**SB**	**CB**	**SB**	**CB**	**SB**	**CB**	**SB**	**CB**	**SB**	**CB**
S1	0.24	0.14	0.26	0.14	0.16	0.09	0.11	0.09	0.12	0.05	0.17	0.08	0.07	0.03	0.05	0.02
S2	0.17	0.13	0.15	0.13	0.10	0.09	0.16	0.10	0.07	0.08	0.08	0.08	0.04	0.05	0.07	0.03
S3	0.09	0.05	0.09	0.15	0.03	0.16	0.04	0.19	0.05	0.03	0.06	0.06	0.02	0.01	0.01	0.06
S4	0.09	0.17	0.06	0.07	0.02	0.02	0.07	0.01	0.03	0.07	0.01	0.03	0.01	0.01	0.01	$<10^{-2}$
S5	0.19	0.11	0.17	0.05	0.16	0.05	0.20	0.06	0.09	0.06	0.10	0.03	0.07	0.03	0.07	0.02
S6	0.12	0.09	0.19	0.09	0.06	0.03	0.17	0.05	0.07	0.05	0.09	0.06	0.01	0.02	0.07	0.02

In previous works, this has allowed to characterize the possibly different behaviours of time domain measures and frequency-specific measures, which have been found to be more precise and informative than overall indices, especially when the observed processes exhibit frequency-specific oscillations [199], [200].

Several studies have documented that the magnitude of respiratory-related fluctuations of RRI (i.e., respiratory sinus arrhythmia) dramatically changes according to breathing rate [201]. Moreover, it has been demonstrated that paced breathing at ~0.25 Hz does not alter efferent vagal and sympathetic modulations in the frequency range from 0.04 Hz to 0.15 Hz in healthy subjects [202], [203]. A decrease of both time and spectral measures in CB with respect to SB in 3 subjects (50%) was observed, while increased or unchanged values were detected in the remaining samples (Table I). These findings must be further investigated according to the subject-specific spontaneous breathing rate and with bigger datasets. The possibility to enroll a larger number of subjects and carry out statistical analyses represents one of the future extensions of this study, that will enable a clearer assessment of the feasibility of the proposed approaches for the extraction of respiration from the PPG. Nonetheless, these preliminary findings suggest that causality measures behave similarly if the PPG is used in place of the ECG for the detection of heart period and the sampling of respiration. On the other hand, the filtering and EMD approaches for the extraction of respiration from the PPG may be less accurate in the quantification of time domain and spectral measures, and especially of respiratory PSD. Indeed, applying a PPG bandpass filter to identify respiratory dynamics may cause misdetection of power content if other oscillatory components are present within the selected HF range or if the peak bandwidth is too large. Conversely, the EMD extraction technique is based on how well the detection of PPG peaks is performed, and this may pose a problem when the acquired waveform is noisy, due e.g. to motion artifacts.

In conclusion, in this study were investigated two different techniques for extracting the respiratory signal from the PPG one introduced and discussed in Chapter 2 (i.e., the filtering-based and the EMD approaches), also leveraging the multiparametric nature of the acquired data to obtain insights into cardiorespiratory interactions on both PPG and ECG data. Specifically, the results highlight how the causality measures obtained considering both ECG and PPG signals are similar, suggesting the use of the latter, which are more easily accessible especially on wearable devices, as an alternative instead of the ECG to evaluate cardiorespiratory interactions. Furthermore, the results demonstrate how both the EMD and filtering-based approaches, although it emerged that for the latter one must pay attention to signal bandwidth variability, allowed for the extraction of a respiratory signal similar and comparable to that directly detected by the nasal probe, thus suggesting the implementation of these algorithms for extracting respiratory rate even on the realized wearable device.

4.4 STRESS DETECTION THROUGH GSR MEASUREMENTS

The work presented in this subsection continues the investigation about the implementation of the multiparametric biomedical device already discussed in the previous paragraph, this time with the aim of detecting changes in the individual's physiological states in response to stressful events. The feasibility of using the GSR signal, in conjunction with ECG and PPG signals, was evaluated to assess physiological states of stress related to the effect of spontaneous and controlled breathing. Furthermore, the GSR signal has been acquired employing the corresponding analog circuit developed and analyzed in Chapter 3, to confirm its suitability for detecting stressful situations for the individual. Furthermore, since stressful events lead to changes in cardiovascular parameters, PPG and ECG signals were simultaneously acquired to verify and justify from the physiological point of view any changes in sweating.

A controlled breathing measurement protocol was carried out to induce changes in ECG, PPG and GSR signals, thus showing the potential of integrating a GSR sensor in a synchronous multi-parametric acquisition system for detecting changes in physiological state related to stressful events.

4.4.1 EXPERIMENTAL PROTOCOL

Measurements were recorded on a normotensive healthy 22-years old female while sitting on a chair. Four ECG electrodes were positioned on the wrists and legs in accordance with Einthoven’s triangle for up to 3-lead electrocardiographic signal acquisition. The PPG probes were worn on the left wrist and forearm for pulse sphygmic detection, while breathing and GSR probes were worn respectively on the nose and on the index and middle fingers of the hand (according to [63]). All the signals were sampled at 24-bit resolution with a 500 Hz sampling frequency. Once again, data were transferred wirelessly via Bluetooth using the appositely developed GUI to a personal computer, plotting as well the signals in real-time, in order to visually detect any artifacts due to incorrect probes positioning (refer to [194], [195] for further information).

In order to evoke physiological changes both in cardiovascular parameters and sweat glands activity during the real-time acquisition, the following experimental protocol was implemented:

- Rest 1 (R1): 360 seconds in which the subject was breathing spontaneously in a resting condition;
- Controlled breathing (CB): a 360-s recording in which the subject was instructed to carry out a paced breathing with period of 6 seconds, in which each cycle consisted of 3-seconds inhale and 3-seconds exhale phases;
- Rest 2 (R2): another 360-s recording in which the subject breathes spontaneously analogously to R1.

An initial preparation procedure lasting around 150 seconds was carried out, recorded but not used for the analysis, in order to check the correct functioning of the system and installation of the probes and to allow acquiring data in stationary conditions. During all phases, the subject was instructed not to make any movement and to remain seated on a chair for the entire measurement protocol duration. During the paced breathing phase, the subject followed a visual metronome appositely developed to support the correct execution of controlled breathing (refer to [194] for further information).

4.4.2 RESULTS AND DISCUSSION

For data analysis, the ECG lead I and the PPG acquired on the left wrist were considered, in addition to the signals obtained by NTC and GSR sensors. Fig. 4.10(a) and (b) show the heart rate trend computed respectively from the RRI and pulse to pulse interval (PPI) time series extracted from ECG lead I signal and from the PPG signal. Fig.4.10(c) depicts the trend of the raw GSR signal during the measurement protocol from the R1 phase (0s-360s), followed by the CB phase (360s-720s) to the end of the R2 phase (720s-1080s).
Figure 4.11 reports a 25-seconds detail of recordings from second 150 to 175 s, i.e. across the transition between the spontaneous to the paced breathing conditions occurring at the second 150. The low values of the GSR signal (Fig. 4.11(c)) together with lower values of heart rate (see Fig. 4.10(a) and (b)) (typical for resting conditions [204]) suggest that the subject is relaxed during the R1 phase. GSR in the first phase moreover gradually decreases, indicating that the subject under test becomes more and more relaxed.
A sudden change in the GSR signal occurs from the beginning to about the middle of the CB phase, indicating an increase of the skin conductance which may be due to a shift of the sympathovagal balance towards the sympathetic side.

Although a slower breathing rate typically induces a relaxation response [205], [206] the transient sympathetic activation reported during the transition from R1 to CB may be related to the temporary response of the organism to the different and non-spontaneous breathing pattern, possibly misinterpreted as a stressor or anyway as an external trigger.

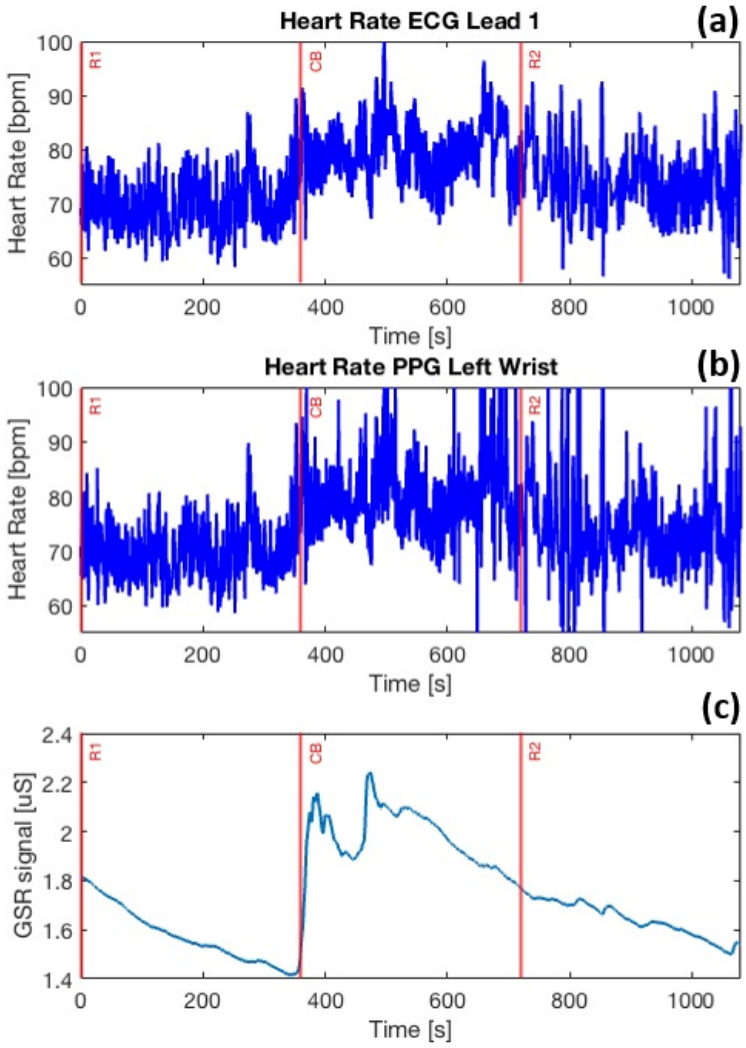

Figure 4.10 *– Complete view of the whole acquisition time window;* ***(a)*** *heart rate ECG lead I,* ***(b)*** *left wrist PPG heart rate,* ***(c)*** *GSR signals during the execution of the measurement protocol. The vertical red lines denote the transition between different breathing conditions according to the adopted experimental protocol.*

During the CB phase, a slight increase of the heart rate can also be observed, which may be related to the fact that the subject was not used to breath in a non-spontaneous way and thus appeared a bit uncomfortable (or even troubled) at the beginning. Moreover, the change of the heart rate due to respiration could be related to the RSA phenomenon [50], [207].

The transition between controlled breathing and the second rest phase did not show any abrupt variations of GSR, which continues to gradually decrease towards the values observed during the first spontaneous breathing condition.

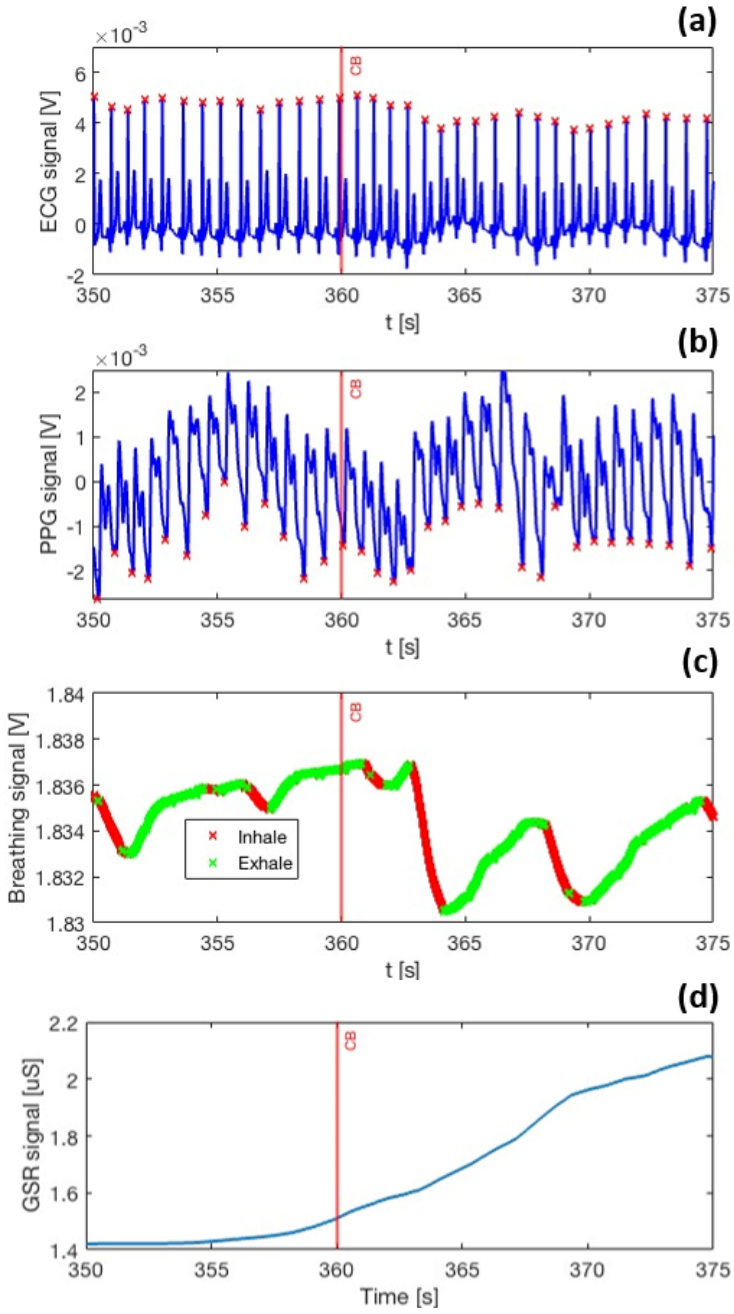

Figure 4.11 *– A 25-seconds recording detail of (**a**) ECG lead I, (**b**) left wrist PPG, (**c**) breathing and (**d**) GSR signals during transition from spontaneous to controlled breathing phases. In (**a**) red crosses indicate ECG R peaks; in (**b**) red crosses indicate PPG minima; in (**c**) the inhale period is indicated in red, while the exhale period in green. The vertical red line denotes the transition between spontaneous and controlled breathing.*

Fig. 4.12 shows the analysis carried out on the GSR signal by LEDALAB, which performs the decomposition of the signal in SCL and SCR activities, as discussed in the related section of the Chapter 2. This analysis evidences the phasic activity, whose trend is shown at the bottom of the figure, only during the transition between R1 and CB (up to the center of this phase), confirming the previous interpretation and remarks. In fact, while on one hand, the analysis of the tonic component alone provides important information about the level of rest and any potential stress the subject is undergoing, on the other hand, extracting the phasic component, being much more reactive, allows obtaining information about the SNS response immediately after the occurrence of the stressor, thus completing the physiological interpretation related to GSR.

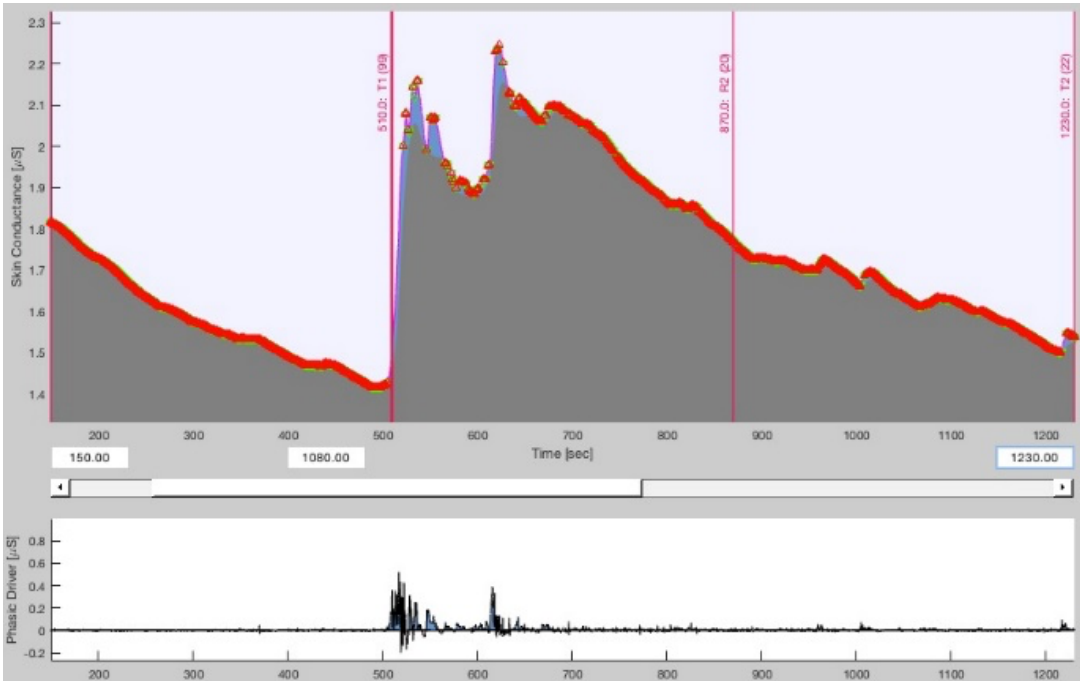

Figure 4.12 *– Analysis of GSR signal carried out using LEDALAB: At the top, GSR signal with both tonic and phasic (in blue) components. In red the peaks of the signal are highlighted. At the bottom, phasic component of GSR signal.*

In conclusion, thanks to this work it was possible to investigate the variations in physiological parameters affecting the cardiovascular system, as well as the sweating of the epidermal tissue, caused by the activation of the ANS following a stressful event, such as the transition from a resting state to paced breathing as in this case.

In particular, it was observed how the GSR signal undergoes sudden changes precisely at the beginning of the paced breathing phase, after which a consistent phasic activity occurs, thus confirming the potential of this signal in discriminating SNS activity and consequently identifying the presence or absence of stress on the individual involved in the measurement. Furthermore, the use of the portable device already developed in the laboratory allowed for the employment and verification of the behavior of the analog circuit developed for GSR signal acquisition, thus confirming its integration even on the wearable device.

4.5 PRELIMINARY VALIDATION OF THE WEARABLE RING-SHAPED BIOMEDICAL DEVICE FOR PHYSIOLOGICAL MONITORING

In the previous subsections, the results of the research on the use of the portable multiparametric device for the non-invasive acquisition of biosignals were presented. Simultaneously, data analysis algorithms were implemented to extract relevant physiological indices, with the aim of enabling discrimination between physiological states and, prospectively, assessing individual health status. The findings obtained from these studies are now collected and implemented to validate, in the final activity herein presented, the wearable biomedical device developed during the research, where the aim is to investigate its use and the feasibility of employing it for the detection of physiological states.

As extensively discussed in Chapter 3, it consists in a wearable ring-shaped device performing non-invasive finger-based measurements of ECG, PPG (red and infrared), GSR, and motion signals. To evoke physiological changes, a measurement protocol was carried out on multiple subjects, involving the performance of different tasks characterized by alternating conditions of rest and physical activity. Subsequently, the data analysis algorithms discussed in Chapter 2 and already investigated by the works introduced in the previous sections, were applied to the measurements, i.e. the implementation of time domain, frequency domain and information-theoretic measures, also performing an UST analysis, which is of crucial importance in the context of WHDs, the extraction of respiratory parameters, finally monitoring the SNS activity considering the SCL component of the SC signal.

Furthermore, since the ring-shaped device is able to synchronously acquire PPG and ECG signals, it has been considered another important parameter known as Pulse Arrival Time (PAT), which is defined as the temporal interval between the R-peak extracted from the ECG and the peak of the pulse wave obtained from the PPG signal [208].

The PAT holds great potential in the assessment of cardiovascular physiology: by reflecting the time taken for the pulse wave to travel through the circulatory system, PAT can be utilized for estimating important parameters such as blood pressure and arterial stiffness [30], [209]. Moreover, it offers a non-invasive approach to monitoring vascular health and could provide valuable insights into overall cardiovascular function and dynamics.

4.5.1 EXPERIMENTAL PROTOCOL AND DATA ANALYSIS

With the aim of validating the use of the wearable device in everyday life scenarios, six healthy subjects of both sexes within the age range of 25-35 years (3 males and 3 females, age 27.3±2.9 years) were recruited and subjected to two different measurement protocols designed to simulate key activities typically performed in daily scenarios. Each protocol lasts for 12 minutes and consists of two phases that differentiate between a resting and stress conditions. The first measurement protocol comprises a resting phase, during which the subject lies on a bed in a supine position (SUPINE) for 6 minutes, followed by a standing phase (STAND) in which the subject remains immobile in an upright position for 6 minutes. The second measurement protocol, on the other hand, requires the subject to remain seated on a chair for 6 minutes, followed by a walking phase (WALK) lasting 6 minutes with the subject instead moving at a normal walking speed. In order to standardize the walking speed, a sports treadmill set to a speed of 4 km/h was utilized. This speed was also chosen to minimize as much as possible any small movements of the wearable device, given by the fact that it might tend to slip during walking in case of not perfect adherence to the subject's finger. The device was worn by all subjects on the index finger of the left hand, the body region where recordings of PPG, GSR, and movement were taken. During SUPINE, STAND, and SIT phases, the ECG signal was also acquired by requiring the subjects to put their left-hand thumb and their index and middle fingers of the right hand on the corresponding ECG electrodes, as discussed in the Chapter 3.

The acquired data underwent a visual inspection to ensure suitability for subsequent processing and analysis. Accelerometer data were also visually analyzed to proactively identify any motion artifacts that could potentially corrupt the relevant signals. For each phase of the measurement protocol, according to the standard short-term HRV analysis approach, a temporal sub-window was selected to obtain 300 beat-long time series [103]. From the ECG signal, RR time series were extracted by considering the temporal distance between two consecutive R peaks. Similarly, PP time series were extracted by considering the temporal distance between two consecutive minima of the PPG waveform, for both the red (PP_{red}) and infrared (PP_{ir}) wavelengths.

From literature, it is well known that the infrared PPG signal exhibits better resolution compared to the red PPG one due to the ability of the infrared wavelengths to penetrate deeper into human tissues [210], [211]. This is reflected in a more reliable detection of the minima of the PPG waveform, resulting in the extraction of PP time series that are more similar to the RR time series. In this work, this aspect was investigated using the Bland-Altman analysis [212], a useful tool for evaluating the agreement between two measurements. Specifically, the agreement coefficient between the PP_{red} and PP_{ir} time series, as well as between each of them and the RR time series was obtained for each subject and acquisition phases by using the following formula:

$$Agreement = \frac{1.96 \cdot std(x_1 - x_2)}{mean((x_1 + x_2)/2)} \quad (1)$$

where x_1 and x_2 represent the two compared time series. Low and closer to zero values for this index are indicative of a good agreement between a measurement under investigation and a well-established reference gold standard. The agreement measures between PP_{ir} and PP_{red} time series were computed for all the four phases (i.e., SUPINE, STAND, SIT, and WALK phases). On the other hand, the agreement between RR and PP time series was computed only for SUPINE, STAND, and SIT phases and not for the WALK phase, since the ECG signal was not acquired in this last part of the experimental protocol. In light of worse quality of red PPG signals, PP_{red} time series have been discarded for further cardiovascular dynamic analysis. Similarly, the PAT time series, calculated by considering the time interval between the R-peak of the ECG and the peak of the PPG waveform within the same cardiac cycle [30], were obtained by using the infrared PPG signal.

The GSR time series were obtained by sampling the GSR signal at the peaks of the infrared PPG waveforms, and the analyses were focused on calculating the mean and standard deviation of the obtained GSR time series.

Starting from the minimum and maximum values extracted from the red and infrared PPG signals, it was possible to calculate the SpO_2 values using the methodology discussed in the Chapter 2 (i.e., by applying the empirical model and calibration process). In particular, the SpO_2 calibration for the ring-shaped wearable device was carried out using a commercial pulse oximeter, that has allowed for the acquisition of the heart rate from 25 to 250 bpm and SpO_2 from 35% to 100%. The calibration procedure of the device was carried out on preliminary measurements from the volunteers to extract the *a* and *b* constants present in the equation (21) of the Chapter 2 from a calibration curve obtained by curve fitting. The regression line between the R and SpO_2 values was computed using the least squares approximation method by curve fitting the data from volunteers [141], [213]. The obtained regression line was:

$$SpO_2 = 112.07 - 31.44 \cdot R \quad (1)$$

Lastly, following calibration, a comparison was made between the average values of SpO_2 samples obtained using the system and those recorded with the pulse oximeter. The findings revealed that the accuracy of the ring-shaped device is within a range of $\pm 2\%$, relative to the commercial device employed as the reference.

Finally, an estimation of respiratory rate was carried out from the PPG signal, by applying a bandpass filter to the infrared PPG waveforms, based on the knowledge that respiratory variability is typically contained in the HF band (0.15-0.4 Hz) [32], [214]. The respiratory time series were extracted by sampling the reconstructed breathing signal at the peaks of the infrared PPG signal, then estimating the power spectral density through the method discussed in the Chapter 2, thereby identifying the respiratory rate.

The RR, PP_{ir} and PAT time series were analyzed to extract indices reflecting physiological changes in response to the different phases of the acquisition protocol. The classical HRV time-domain indices were calculated, i.e. the average (MEAN), standard deviation (STD), and the RMSSD on RR and PP_{ir} time series (referring in the latter case to PRV) [49]. Analogously, the time-domain indices of MEAN and STD were computed on the PAT time series.

Before performing frequency-domain and information-theoretic analysis, physiological time series were preprocessed applying a high-pass autoregressive filter (cut-off frequency of 0.0156 Hz) and normalizing the filtered series to zero mean and unit variance. The non-parametric Blackman-Tukey method (Hamming window, bandwidth of 0.04 Hz) was applied to obtain the power spectrum for each subject and condition of RR, PP_{ir} and PAT time series [157]. The LF and high-frequency HF power contents were evaluated by integrating the distribution in the ranges 0.04-0.15 Hz and 0.15-0.4 Hz, respectively [49]. These power values are generally used to obtain the ratio between the LF and HF contents. Although still debated, this index gives insight on the sympatho-vagal balance in HRV analysis. Conversely, its role in the analysis of PAT variability is not clear and seems to be unrelated to the ANS regulatory activity [62].

Finally, the conditional entropy measure was computed to characterize the time series complexity in terms of its irregularity and unpredictability, quantifying the residual uncertainty about the current state of the process remaining when past dynamics are known [126]. Specifically, this index decreases as the predictability of the series increases and reaches zero for fully predictable dynamics. Under the hypothesis of Gaussianity and processes stationarity, this index was computed using the linear estimation method (i.e., equation (8) of the Chapter 2). The order of the AR model used to the describe the physiological processes was set to m=2, and the ordinary least squares method [215] was used to identify the variance starting from the regression coefficients.

4.5.2 STATISTICAL ANALYSIS

In order to assess the subject-specific feasibility of the computed indices in the identification of a position change during the acquisition, the activity foresee also a statistical validation. To this end, a statistical analysis was performed to assess the feasibility of using the above-described indices to discriminate changes between different physiological conditions. Bootstrap data analysis [216] was employed to assess the statistical significance of the results, generating a distribution of values for each subject, phase acquisition protocol, and feature computed on RR, PP_{ir} and PAT time series. Specifically, one-hundred data windows of 120 samples were randomly extracted from the original 300-points time series, and then time, frequency and information domain indices computed for each of the surrogate data.

This approach allows to obtain for each subject a distribution of the evaluated index in the different acquisition phases, thus becoming statistically comparable. Specifically, a parametric Student *t*-test for unpaired data was applied to compare the distributions of the indices evaluated on surrogates obtained in SUPINE and STAND positions, as well as in SIT and WALK conditions (in this case taking into account only the PP_{ir} time series indices). For all the comparisons, the significance level was set at $p < 0.05$.

4.5.3 RESULTS

In this section, the results of the acquisitions carried out using the ring-shaped device during the measurement protocols involving the six participants are reported.

Figure 4.13 shows the PPG waveforms (both red and infrared), ECG, GSR, and motion signals in terms of spatial acceleration across the three axes, acquired by the device during the SUPINE-STAND measurement protocol. In particular, Figures 4.13a and 4.13b show the detail of a 10-second acquisition window, allowing the visualization and qualitative appreciation of the high fidelity of the acquired biosignals. Both PPG waveforms exhibit the typical morphology reported in the literature [76], [217], with the dicrotic notch clearly visible, and the end of the systolic phase and the beginning of the diastolic phase (respectively indicated by maximum and minimum of the PPG signal) marked by red crosses. Both signals are well-defined, and it is noteworthy that the PPG infrared signal is consistently more resolved, because the infrared wavelengths have the feature to penetrate more deeply into the body skin and tissues [210], [211]. Similar remarks can be made with regard to the ECG signal being well-defined as well, with the R peaks (also marked by red crosses in Figure 4.13b) easily distinct from other points in the QRS complex. Figures 4.13c and 4.13d depict the waveforms of the skin conductance (or GSR) and motion signals over the entire duration of the first measurement protocol, which lasts approximately 12 minutes (more than 600 seconds, as visible on the t-axis of both graphs). Both signals remain stable during the acquisition, with the GSR signal showing a slight decrease over time, indicative of the subject being in a resting state during the measurement protocol. Furthermore, the trend and values of the GSR signal on the fingers align with those found in the reference literature [51], [63].

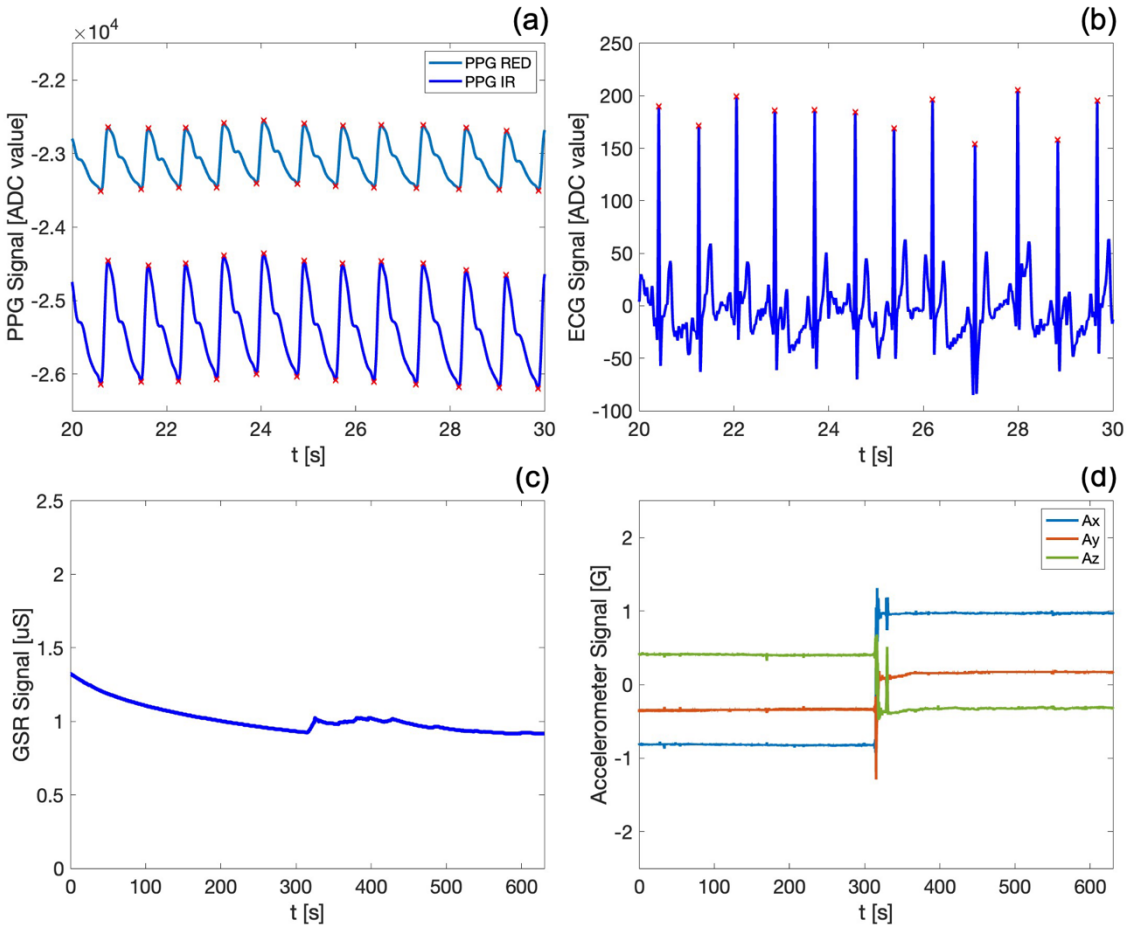

Figure 4.13 *– Exemplary signals acquired on a subject during the first measurement protocol: (**a**) PPG (both red and infrared) and (**b**) ECG signals on a 10-s time window; (**c**) GSR and (**d**) motion signals over the entire duration of the protocol. In (**a**) and (**b**), red crosses indicate PPG maxima/minima and ECG R peaks, respectively.*

A similar comment can be made for the accelerometric signals in the x, y, and z axes, whose variations allow for the identification of the subject's position and any voluntary or involuntary movements, substantially contributing to obtaining more information about the subject's motor activity during the measurement protocol. Indeed, a sudden change in the accelerometric data can be observed, indicating the actual change in the subject's position from supine to stand, which occurs precisely at the halfway point of the first protocol. At this regard, the GSR signal also identifies this transition, as evidenced by a sudden increase in sweating corresponding to the phase change.

The visualization of all the biosignals acquired by the system is of great assistance in highlighting the capabilities and functionalities of my device, especially considering that all these traces are acquired synchronously, on the same body district, and using a device that occupies the space of just one finger on a hand.

Figure 4.14 shows the results of agreement measurements computed using the Bland-Altman method between RR and PP time series extracted from the ECG trace and the two PPG signals. These analyses were conducted to assess the reliability of the interbeat interval time series extracted from the two PPG traces compared to those extracted from the ECG, which is used as the reference. Furthermore, this comparison is also crucial to assess the reliability of the time series during different phases of the protocol, aiming to understand whether motor activity might lead to corruption of the time series themselves. The agreement between PP_{ir} and PP_{red} extracted during the two measurement protocols is shown in Figure 4.14a.

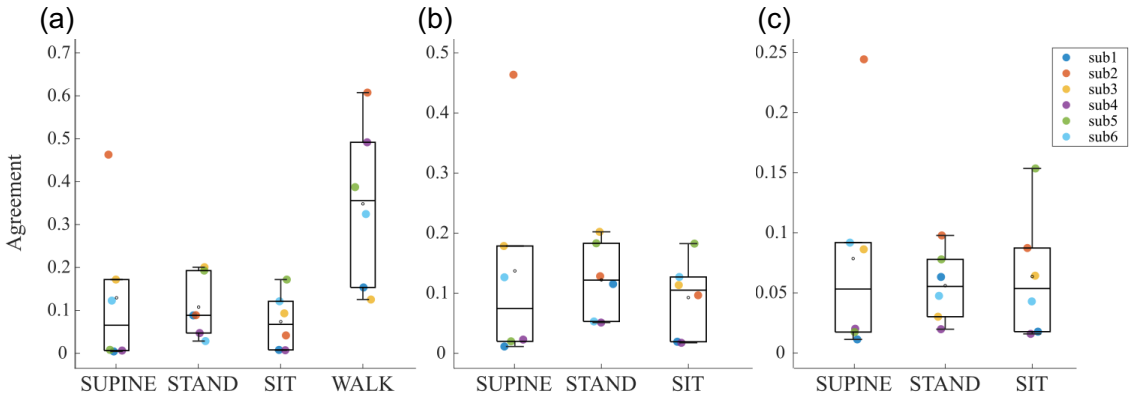

Figure 4.14 *– Boxplot distributions of agreement indices computed using computed using the Bland-Altman method between* ***(a)*** *PP_{ir} and PP_{red},* ***(b)*** *PP_{red} and RR, and* ***(c)*** *PP_{ir} and RR, evaluated across all six subjects during the four phases (i.e., SUPINE, STAND, SIT and WALK) of the two measurement protocols.*

A very good agreement is observed for almost all subjects in phases without motor activity (i.e., SUPINE, STAND, and SIT phases), with values ranging between 0 and 0.2, except for the subject 2 (*sub2)* during SUPINE phase. Conversely, in the presence of motor activity, there is a noticeable deterioration in the agreement, with an average value of 0.35 and an increased dispersion of values among subjects. This finding is expected, as physical activity leads to worsened measurement conditions, primarily due to the presence of motion artifacts resulting in a reduced quality of the acquired physiological signals, with the PPG signal being particularly affected. This leads us to consider less reliable the physiological indices extracted from PPG signals, e.g blood oxygen saturation and respiration rate, during this phase.

Figures 4.14b and 4.14c show the agreements obtained by comparing RR with PP_{red} and PP_{ir}, respectively. Even if similar distributions can be observed across the acquisition phases, it is interesting to note how agreement values range between 0 and 0.2 for PP_{red} and are halved for PP_{ir}, thus confirming once again the overall better quality of the infrared PPG signals.

Starting from the above-described results on the quality of the acquired signals, the subsequent analyses were focused on the extraction of most physiological indices from the PP_{ir} time series only. The evaluation of the blood oxygenation makes an exception, requiring both PPG waveforms. Besides, the same indices obtained on PP_{ir} time series have also been extracted for the RR time series in order to have reference levels to compare and assess the reliability of the PPG signal acquired by the device, thus allowing to consider it reliable even in situations where the ECG signal is not acquired, such as during the WALK phase in our case.

Table 4.2 presents the physiological indices (expressed as mean value ± standard deviation) extracted in the time, frequency, and information domains from 300-point PP_{ir}, RR, and PAT time series, obtained from the six subjects during the two measurement protocols. The reported values during the SUPINE, STAND, and SIT phases, and for some of the time series even during the WALK phase, are consistently in line with what is typically reported in the literature, both for resting situations which are followed by the transition to a more stressful physiological condition [63], [218], [219]. In detail, the heart rate is lower in resting phases and increases during the following two physiological conditions. This response reflects the level of activation of the ANS as also indicated by an average decrease of the SDNN and RMSSD indices with STAND, and contrarily an increase during SIT (except for $RMSSD_{PPir}$). Moreover, as expected, the LF/HF ratio increases during the other phases of the protocol if compared to REST. CE values are lower during STAND phase, indicating higher regularity and predictability of cardiac dynamics. All these results reflect the well-known prevalence of the parasympathetic branch activity in a resting condition, and the sympathetic activation occurring during stress states. In general, different considerations can be made for the measurements obtained during the WALK phase. Indeed, the consistent presence of motion artifacts leads to a degradation of the PPG signal and, consequently, of the PP_{ir} time series. This results in a loss of reliability in the extracted indices, since it is possible to observe an unexpected increase in SDNN, RMSSD, and LF/HF values, accompanied by an increase in CE, indicating an augmentation in the complexity of the PP_{ir} time series.

The worsening of the quality of the PPG waveform during WALK is also evidenced by a relevant increase in the variability of SDNN and RMSSD across subjects.

Table 4.2 *– Results of short-term analysis of PRV, HRV, PAT, GSR, blood oxygen saturation levels, and respiration rate (RESP), during the different phases of the measurement protocol and averaged across the six subjects. The values are expressed as mean ± standard deviation.*

Measure/Phase	SUPINE	STAND	SIT	WALK
HR_{PPir} [bpm]	73±12	87±16	77±8	100±10
$SDNN_{PPir}$ [ms]	55.55±20.94	51.10±21.26	58.65±25.05	85.22±42.08
$RMSSD_{PPir}$ [ms]	57.47±37.57	38.46±17.95	47.16±25.19	109.94±72.57
LF/HF_{PPir}	0.68±0.30	2.12±1.94	1.30±0.44	1.17±1.10
CE_{PPir} [nats]	1.20±0.12	0.94±0.31	1.07±0.10	1.27±0.23
HR_{RR} [bpm]	74±12	87±16	77±8	-
$SDNN_{RR}$ [ms]	51.53±20.14	48.68±21.91	59.48±24.96	-
$RMSSD_{RR}$ [ms]	44.55±19.79	31.31±21.63	50.14±26.06	-
LF/HF_{RR}	1.05±0.54	3.41±3.55	1.46±0.93	-
CE_{RR}	1.13±0.12	0.76±0.34	1.08±0.21	-
$MEAN_{PAT}$ [ms]	372.60±51.01	349.92±26.47	396.31±60.71	-
STD_{PAT} [ms]	14.49±9.26	17.25±9.57	19.66±12.38	-
LF/HF_{PAT}	0.39±0.14	1.03±0.44	1.08±0.24	-
CE_{PAT} [nats]	3.92±0.80	4.15±0.51	4.07±0.59	-
GSR [μS]	0.80±0.21	0.86±0.14	1.11±0.39	3.17±1.04
SpO_2 [%]	97.8±1.6	98.7±1.7	99.9±0.19	88.05±21.11
RESP [Hz]	0.27±0.04	0.23±0.06	0.25±0.07	0.32±0.03

The achieved results on PAT time series are also supported by previous works [62], reporting a decrease of the time of arrival of the pressure wave at the body periphery and an increase of its variability during physical stress. Contrarily, no supporting results have been achieved in literature about the reported findings in the frequency domain, which show an increase of LF/HF ratio during STAND and SIT.

The modification in the ANS activity is also confirmed by the GSR values computed from GSR time series, which are lower during resting conditions and higher during stress, especially during the transition from SIT to WALK when the GSR triples its value. Similarly, respiration rate particularly increases during WALK, as expected.

The SpO_2 index is in line with the expected values (97-99%) during resting conditions, while the presence of artifacts degrades the PPG signal up to severely limiting its use for calculating blood oxygenation levels during non-static measurement conditions, given that the agreement between the two PPG signals worsens excessively (cf. Figure 4.14a).

Figures 4.15, 4.16 and 4.17 depict the results of the bootstrap analysis performed on the time, frequency and information domains indices computed for PP_{ir}, RR and PAT time series, evaluated individually for each subject. Statistical analyses were performed on the distributions obtained in the SUPINE and STAND positions, as well as SIT and WALK positions for the PP_{ir} time series, in order to prove on a single-subject basis the capability of using the device for discriminating physiological changes.

The results of the analyses conducted on PP_{ir} during the SUPINE and STAND phases are shown in Figure 4.15a. Both time-domain indices (i.e., MEAN and SDNN) decrease significantly from the first to the second phase for all the subjects except the fifth, showing instead a significant increase in SDNN. Frequency analysis reveals that in all subjects a significant increase in the LF/HF ratio is detected. Finally, CE measures undergo a significant decrease for all subjects except the first, for whom a significant increase is observed from the SUPINE to the STAND phase. In Figure 4.15b, the results obtained for the same time series during the SIT and WALK phases are reported. In this case, a significant decrease in MEAN values is observed for all subjects as well, while a statistical increase in SDNN values is observed for all subjects except the fifth, showing instead a significant decrease. The LF/HF ratio significantly decreases for four subjects, while a statistical increase is observed for the other two. Finally, CE significantly increases in all subjects except the first, for whom a statistical decrease is instead reported.

The results of the analyses conducted on RR time series during SUPINE and STAND are depicted in Figure 4.16. They confirm most of the findings obtained from the analysis of the PP_{ir} time series, as nearly identical trends in the indices are reported compared to those highlighted with regard of Figure 4.15a. Indeed, also in this case both MEAN and SDNN undergo a significant decrease for all subjects, with the only difference being that, in this instance, no statistical difference is detected in SDNN values for the second subject between the SUPINE and STAND phases. The trend is also confirmed for LF/HF ratio, where a significant increase is once again observed for all subjects. Finally, CE shows a statistically significant decrease in all subjects.

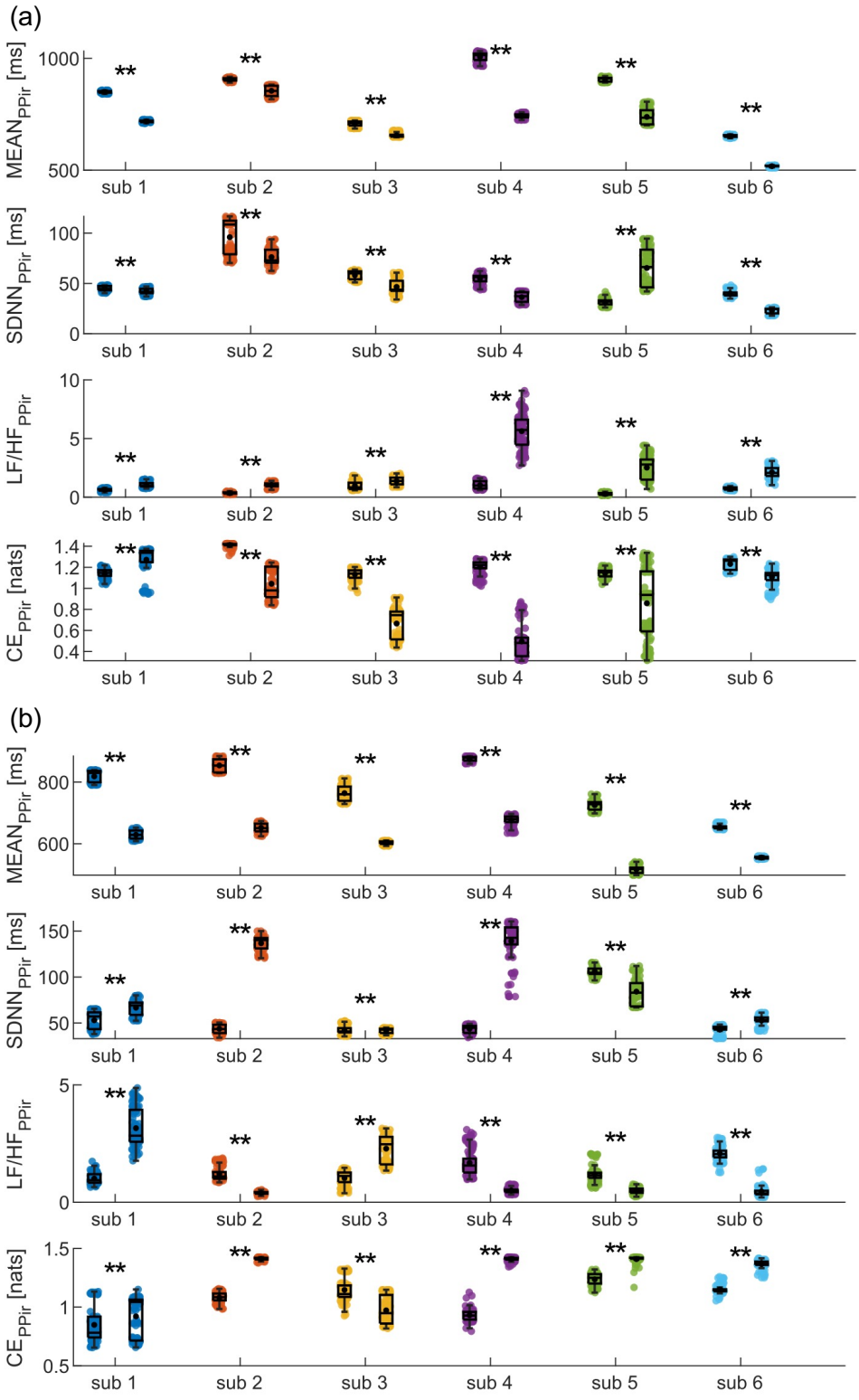

Figure 4.15 *– Results of PP_{ir} time series analysis in time, frequency, and information domains of MEAN, SDNN, LF/HF and CE evaluated on the six subjects during* ***(a)*** *the SUPINE-STAND and* ***(b)*** *the SIT-WALK measurement protocols. Statistical analyses were performed between the two different phases considering one hundred sub-windows of 120 points randomly extracted from PP_{ir} time series. Statistical test: Student's t-test; *, $p < 0.05$, **, $p < 0.001$, SUPINE vs. STAND.*

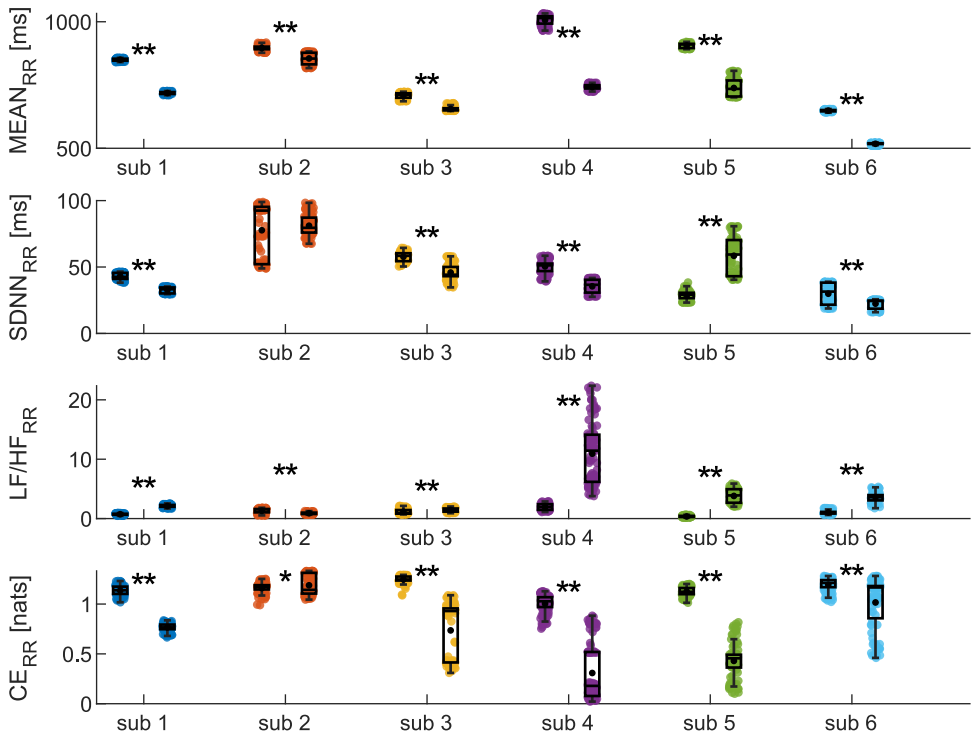

Figure 4.16 *– Results of time, frequency, and information domains analysis on RR time series, evaluated on the six subjects during the SUPINE-STAND measurement protocol. Statistical analyses were performed considering one hundred sub-windows of 120 points randomly extracted from RR time series. Statistical test: Student's t-test; *, $p < 0.05$, **, $p < 0.001$, SUPINE vs. STAND.*

Finally, the same analyses conducted on the PAT time series and depicted in Figure 4.17 yielding results highly dependent on the subject. Specifically, a significant increase and decrease in MEAN are observed for two and three subjects, respectively, while no difference is detected for the fourth subject. Similarly, CE measures indicate an increase between phases for three subjects and a decrease for the other three. The results of the frequency analysis, on the other hand, show a significant increase in LF/HF ratio values for all subjects.

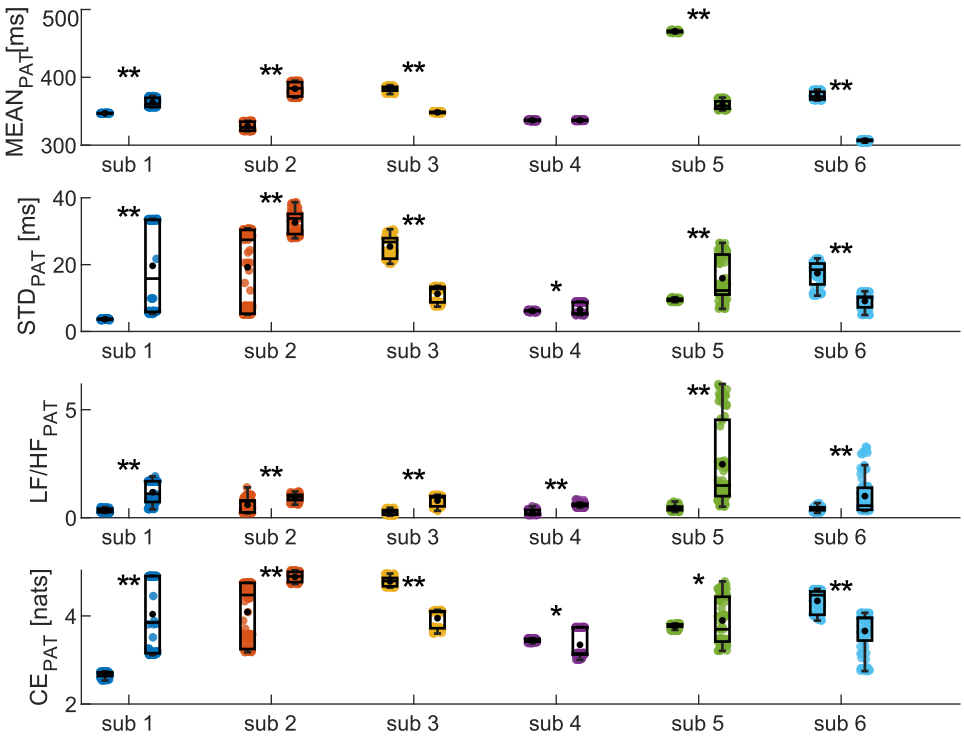

Figure 4.17 *– Results of the analysis of PAT time series in time, frequency, and information domains, evaluated on the six subjects during the SUPINE-STAND measurement protocol. Statistical analyses were performed considering one hundred sub-windows of 120 points randomly extracted from the starting PAT time series. Statistical test: Student's t-test; *, p < 0.05, **, p < 0.001, SUPINE vs. STAND.*

4.5.4 DISCUSSION

From Figure 4.13, it is evident how the device is able to acquire the biosignals of interest with high resolution, thus allowing the acquisition of key physiological parameters directly from the fingers, providing clear advantages in terms of usability and user comfort. Indeed, the biomedical sensors (i.e., the ECG and GSR electrodes) and the inertial module have been suitably placed to detect biosignals in strategic points on the fingers of the hand, enabling their acquisition in a simple and effective manner. The system architecture chosen during the design phase has proven to be crucial in enabling the synchronous high-resolution acquisition of all the recorded biosignals at a sampling frequency of 1 kHz. These characteristics effectively constitutes the main advantage of the device compared to currently available wearable technologies currently present in the market.

The results obtained from the agreement measurements between cardiovascular signals (i.e., PPG and ECG ones) have allowed considering PP time series as surrogates for RR ones during stationary physiological states (Figures 4.14b and 4.14c). This is a remarkably interesting result, given that, as well known in the literature, the ECG signal is more challenging to acquire due to its measurement methodology which, in the case of wearable devices, requires the use of both hands throughout the entire measurement duration [41], [75]. This paves the way for the deployment of PPG signal as a surrogate for ECG also in situations where it is impractical to require the user to engage both hands during recordings.

The findings of the short-term analyses performed on the biosignals acquired with the device and resumed in Table 4.2 highlight the feasibility of the indices of clinical and research interest to reflect physiological changes, thus confirming that the device is capable of detecting these changes as a result of human motion within a small range of values (i.e., considering a 120-point window). Moreover, the single-subject analysis performed using combined bootstrap method and ultra-short-term analysis show how results achieved using PP and RR time series are in agreement and almost consistent among subjects. Indeed, the results of PRV (Figure 4.15a) and HRV (Figure 4.16) analyses, evaluated during the supine-stand protocol, agree with the widely documented evidence in the literature regarding variations in physiological indices between rest and stress conditions [81], [220], [221], [222], [223]. Specifically, a decrease in MEAN and SDNN and an increase in LF/HF and CE can be observed, trends which have been widely put in relation to a shift in the sympathovagal balance in favor of the sympathetic branch, which is typical during transitions from resting to stress physiological conditions [224], [225]. The activity of the SNS also causes an augmented activity of sweat glands, resulting in an increase of epidermal sweat: this physiological mechanism is detected by the GSR signal, whose values are higher during stress conditions (Table 4.2). Additionally, as well-established, the increase in sympathetic activity caused by orthostatic stress leads to a reduction in cardiac dynamics, as evidenced by the significant decrease in CE from the rest to stress phase [56], [161], [226]. Regarding the ultra-short-term PRV analysis conducted during the sit-walk protocol (Figure 4.15b), it is possible to observe the same results highlighted by the indices extracted for the short-term analysis (Table 4.2). A decrease of the MEAN index is reported in all subjects, in line with typical trends of this parameter during stress situations. On the other hand, there are unexpected variations in SDNN and LF/HF, which show different trends between subjects.

Furthermore, there is a significant increase in CE in all subjects, indicating an increase in the complexity of the PP time series during the walk phase. The analyses conducted on the PAT time series (Figure 4.17) report average values of the extracted indices that align with those reported in the literature for healthy subjects in both resting and orthostatic stress conditions [62], [209], [219]. Lastly, findings highlight a strong deterioration of the agreement levels between the two PPG signals, especially during the walking phase (Figure 4.14a), confirming the well-known fact that the PPG signal is overly sensitive to motion artifacts typically encountered during physical activity.

While on the one hand these results underscore the potential of the multiparametric acquisition capabilities of the device, at the same time, they highlight the well-known limitations of the reliability of PPG signals extracted during non-stationary conditions like walk (Figure 4.14a) [78], [99], [100], which entails the deterioration of the signal and consequently of the extracted physiological indices, as previously discussed. These findings strongly encourage the future implementation of motion artifact correction algorithms to allow for a more accurate detection of physiological parameters even during physical activities [98], [227]. In this regard, the embedded inertial module, which has been integrated into the device to enable the detection of voluntary and involuntary movements, is fundamental for providing useful data for a future use by artifact correction algorithms. In this way, it will be possible to automatically correct the noisy PPG signal by exploiting accelerometer data, enhancing the reliability of physiological indices extracted during non-stationary conditions.

In conclusion, with the work herein discussed, the long but exhaustive presentation of the research results about the feasibility of the implementation of hardware solutions and biomedical algorithms on the wearable device is finally concluded. Indeed, these preliminary measurement results obtained during various physical activity conditions demonstrated that the wearable device can be successfully employed to monitor and discriminate among different physiological states. The combined analysis of cardiovascular variability indices in the time, frequency, and information domains and of the acquired GSR signals, allowed the assessment of the autonomic tone and especially the activation of the sympathetic branch of ANS, thereby providing insights into individual emotional arousal. Furthermore, the comparison of PRV indices with HRV indices, both extracted from the wearable device, yielded promising results that suggest the validation of PRV indices under stationary physical conditions (i.e., in absence of motor activity).

The results also confirmed the limitations, widely acknowledged in the literature, regarding the degradation of the PPG signal in the presence of motion artifacts. This finding encourages the implementation of algorithms for the removal and correction of motion artifacts in situations involving continuous physical activity. Finally, the features of the developed device, including its compact size, user-friendly simplicity, and the capability to continuously and non-invasively acquire key physiological parameters, alongside with the promising results from a first measurement campaign, position it as a potential tool for monitoring individuals during their daily routines.

CHAPTER 5

CONCLUSIONS

This thesis has been focused on the design and development of biomedical devices as well as on the implementation of data analysis algorithms aimed at providing non-invasive, simple, and comfortable monitoring of individual health and well-being. The main methods resulting from deep investigation on non-invasive measurement of key biosignals that provide crucial information about the subject's clinical condition have been presented. Data analysis methodologies related to the examined biosignals have been outlined, allowing for the effective extraction of physiological indices and information, enabling a detailed health assessment in a non-invasive manner. Finally, the ring-shaped wearable biomedical device has been designed and developed, encapsulating the research and reasoning on non-invasive acquisition and the implementation of effective data analysis, aiming to provide a solution to the need for innovative, simple, comfortable, and reliable methods for health assessment.

The research results have identified the potential of both non-invasive multiparametric devices and computationally-efficient biosignals processing methods, confirming their utility in the biomedical field. In fact, the ring-shaped wearable biomedical device realized and discussed in this thesis enables the synchronous acquisition of many of the main biosignals that can be monitored non-invasively and are capable of providing information about the health status, i.e., the PPG, ECG and GSR signals. The results obtained from the measurement campaign allow to assert that all the processed biosignals can be easily acquired directly from the fingers. This circumstance, together with other features of the device, including its compact size, its user-friendly simplicity, and the capability to continuously and non-invasively acquire key physiological parameters, position it as a potential tool for monitoring individuals during their daily routines.

Furthermore, thanks to an in-depth study of the biomedical components available on the market, the device boasts a frequency rate of all signals equal to 1 kHz, thus ensuring temporal resolutions of each biosignal in the order of milliseconds, thereby expanding the scenarios for biomedical data analysis.

From the biomedical data analysis standpoint, the synchronous acquisition of ECG and PPG signals, initially pursued using portable biomedical instrumentation and subsequently with the developed wearable device, has led to several important results. Foremost among these is the comparison between PRV and HRV analyses, the results of which have allowed considering the indices extracted from the first one as surrogates compared to those commonly extracted by performing HRV analysis, thus validating the use of the easier-to-employ PPG technique as an alternative to ECG signal acquisition for extracting such indices during stationary physical conditions (i.e., in absence of physical activity).

In a second instance, having both ECG and PPG signals with the millisecond resolution allowed for PAT computation, which has been obtained directly from the signals acquired by the wearable device; the results obtained aligned with the PAT values typically observed in healthy subjects and under steady physiological conditions. These findings confirm the feasibility of extracting of the PAT on wearable devices, expanding the scenarios for biomedical analysis, thus enabling estimations of blood pressure and evaluating vascular system functionalities.

The possibility of performing synchronous measurements has allowed also for multivariate analysis, investigating the joint dynamics between various systems, as demonstrated in the case of cardiorespiratory interactions, where the study of the causal effect from respiration to the heart period extracted from both PPG and ECG signals has been computed through Granger causality measures. The results have shown similar cardiorespiratory interactions, confirming once again the possibility of employing the PPG technique as an alternative to ECG.

Finally, starting from the acquisition of both red and infrared PPG signals, it was possible to calibrate the wearable device to perform SpO_2 measurements and, also, to estimate the respiration rate, thereby enabling the extraction of physiological information about the respiratory system.

The investigation relevant to the implementation of multiparametric devices has revealed their significant potential not only for real-time monitoring but also for multilevel stress assessment.

Indeed, our results confirm evidences in the literature showing that the GSR signal is a valuable tool for stress assessment, as it allows the detection of new physiological conditions following the occurrence of physical stress situations; the present work has evidenced those that characterize a change in posture (e.g., sitting, standing, lying down) or a transition from normal breathing to paced breathing.

In addition to device design, physiological indices extraction and parameter monitoring, it is also crucial to develop further robust analysis techniques that can effectively handle noise, artifacts, to align as closely as possible with the stationarity conditions of a process. Indeed, this is important since biomedical signals can be influenced by a variety of external and internal factors that generate disturbances or undesired variations in the data. With a decrease in the duration of the acquisition window, the number of motion artifacts detected potentially decreases as well. This is a very important point since, as it has been seen, motion artifacts are a major limitation in bio-signal measurements, especially for wearable devices. Finally, the ability to obtain physiological information in a short time would also avoid excessively stressing the user undergoing measurements, which is also one of the objectives set in this thesis. This has led to focusing the attention of this work also on the possibility of performing UST analysis, namely by considering very small acquisition time windows, thus reducing the possibility that the biosignal under examination may be affected by these factors. In this context, significant results have been obtained from the analysis of the use of UST indices for the detection of physiological states in the time, frequency, and information domains, where several findings obtained in the studies herein conducted highlight how physiological indices extracted from cardiovascular series in all three domains allow for discriminating physiological changes between resting and stress conditions, even considering time windows below 300 data points, particularly managing to go down to 120 points and sometimes as low as 60 points. These findings encourage the use of shorter time series, consequently enabling biomedical devices to consume fewer computational and energy resources during the measurement process.

While on the one hand this work has yielded several important results, on the other hand, it has brought to light some issues related to the use of wearable devices and biosignals processing techniques.

Indeed, although the results suggest the reliability of the wearable device under stationary conditions, they also confirm the main limitations shared by WHDs regarding the acquisition of biosignals under non-stationary conditions and, particularly, in the presence of motion artifacts. In this context, the possibility of utilizing data from inertial modules would enable the implementation of algorithms for artifact correction and elimination, thereby improving acquisition performance during non-stationary conditions (i.e., conditions involving subject movement).

Similar considerations can be applied in the biosignal processing techniques landscape, where there is a need to confirm the results of data analyses even for non-stationary conditions, which were not analyzed here. Furthermore, most of the reported results come from studies conducted on small sample sizes, which underscores the importance of continuing the implementation of the data analysis techniques discussed on a larger number of subjects, in order to confirm the findings of this study on a larger scale.

In conclusion, like all research endeavors, the one presented and discussed here cannot be considered concluded; rather, it can be viewed as a solid foundation for further research in the fields of wearable bioinstrumentation and biosignal processing, with the final aim to gain a deeper understanding of ongoing new biomedical studies, methodologies and technologies aimed at human well-being.

References

[1] World Health Organization, *Global diffusion of eHealth: making universal health coverage achievable: report of the third global survey on eHealth*. World Health Organization, 2017.

[2] Y. K. Scherer, S. A. Bruce, C. A. Montgomery, and L. S. Ball, 'A challenge in academia: Meeting the healthcare needs of the growing number of older adults', *J. Am. Acad. Nurse Pract.*, vol. 20, no. 9, pp. 471–476, 2008.

[3] Y. Wang *et al.*, 'Recent advancements in flexible and wearable sensors for biomedical and healthcare applications', *J. Phys. Appl. Phys.*, vol. 55, no. 13, p. 134001, 2021.

[4] A. Mohammad Mosadeghrad, 'Healthcare service quality: towards a broad definition', *Int. J. Health Care Qual. Assur.*, vol. 26, no. 3, pp. 203–219, 2013.

[5] G. L. Tortorella, F. S. Fogliatto, A. Mac Cawley Vergara, R. Vassolo, and R. Sawhney, 'Healthcare 4.0: trends, challenges and research directions', *Prod. Plan. Control*, vol. 31, no. 15, pp. 1245–1260, 2020.

[6] T. H. Nyrönen *et al.*, 'Delivering ICT infrastructure for biomedical research', in *Proceedings of the WICSA/ECSA 2012 Companion Volume*, 2012, pp. 37–44.

[7] J. Baker and A. Stanley, 'Telemedicine technology: a review of services, equipment, and other aspects', *Curr. Allergy Asthma Rep.*, vol. 18, pp. 1–8, 2018.

[8] A. Haleem, M. Javaid, R. P. Singh, and R. Suman, 'Telemedicine for healthcare: Capabilities, features, barriers, and applications', *Sens. Int.*, vol. 2, p. 100117, 2021.

[9] O. S. Albahri, A. Zaidan, B. Zaidan, M. Hashim, A. S. Albahri, and M. Alsalem, 'Real-time remote health-monitoring Systems in a Medical Centre: A review of the provision of healthcare services-based body sensor information, open challenges and methodological aspects', *J. Med. Syst.*, vol. 42, pp. 1–47, 2018.

[10] A. M. Ghosh, D. Halder, and S. A. Hossain, 'Remote health monitoring system through IoT', presented at the 2016 5th International Conference on Informatics, Electronics and Vision (ICIEV), IEEE, 2016, pp. 921–926.

[11] L. P. Malasinghe, N. Ramzan, and K. Dahal, 'Remote patient monitoring: a comprehensive study', *J. Ambient Intell. Humaniz. Comput.*, vol. 10, pp. 57–76, 2019.

[12] G. Aceto, V. Persico, and A. Pescapé, 'Industry 4.0 and health: Internet of things, big data, and cloud computing for healthcare 4.0', *J. Ind. Inf. Integr.*, vol. 18, p. 100129, 2020.

[13] B. Blobel, ‘Application of industry 4.0 concept to health care’, presented at the pHealth 2020: Proceedings of the 17th International Conference on Wearable Micro and Nano Technologies for Personalized Health, IOS Press, 2020, p. 23.

[14] C. Vincent, S. Burnett, and J. Carthey, ‘Safety measurement and monitoring in healthcare: a framework to guide clinical teams and healthcare organisations in maintaining safety’, *BMJ Qual. Saf.*, 2014.

[15] H. Prance, ‘Sensor developments for electrophysiological monitoring in healthcare’, *Appl. Biomed. Eng.*, pp. 265–286, 2011.

[16] T. Tamura, I. Mizukura, M. Sekine, and Y. Kimura, ‘Monitoring and evaluation of blood pressure changes with a home healthcare system’, *IEEE Trans. Inf. Technol. Biomed.*, vol. 15, no. 4, pp. 602–607, 2011.

[17] U. Gogate and J. Bakal, ‘Healthcare monitoring system based on wireless sensor network for cardiac patients’, *Biomed. Pharmacol. J.*, vol. 11, no. 3, p. 1681, 2018.

[18] M. E. Peterson, S. Docter, D. R. Ruiz-Betancourt, J. Alawa, S. Arimino, and T. G. Weiser, ‘Pulse oximetry training landscape for healthcare workers in low-and middle-income countries: A scoping review’, *J. Glob. Health*, vol. 13, 2023.

[19] P. M. Mohan, A. A. Nisha, V. Nagarajan, and E. S. J. Jothi, ‘Measurement of arterial oxygen saturation (SpO 2) using PPG optical sensor’, presented at the 2016 International Conference on Communication and Signal Processing (ICCSP), IEEE, 2016, pp. 1136–1140.

[20] A. Nicolò, C. Massaroni, E. Schena, and M. Sacchetti, ‘The importance of respiratory rate monitoring: From healthcare to sport and exercise’, *Sensors*, vol. 20, no. 21, p. 6396, 2020.

[21] W.-Y. Chung, Y.-D. Lee, and S.-J. Jung, ‘A wireless sensor network compatible wearable u-healthcare monitoring system using integrated ECG, accelerometer and SpO 2’, presented at the 2008 30th Annual international conference of the IEEE engineering in medicine and biology society, IEEE, 2008, pp. 1529–1532.

[22] R. Bhoja, O. T. Guttman, A. A. Fox, E. Melikman, M. Kosemund, and K. J. Gingrich, ‘Psychophysiological stress indicators of heart rate variability and electrodermal activity with application in healthcare simulation research’, *Simul. Healthc.*, vol. 15, no. 1, pp. 39–45, 2020.

[23] E. A. Wehrwein, H. S. Orer, and S. M. Barman, ‘Overview of the anatomy, physiology, and pharmacology of the autonomic nervous system.’, *regulation*, vol. 37, no. 69, p. 125, 2016.

[24] J. V. Freeman, F. E. Dewey, D. M. Hadley, J. Myers, and V. F. Froelicher, 'Autonomic nervous system interaction with the cardiovascular system during exercise', *Prog. Cardiovasc. Dis.*, vol. 48, no. 5, pp. 342–362, 2006.

[25] L. Gatzoulis and I. Iakovidis, 'Wearable and portable eHealth systems', *IEEE Eng. Med. Biol. Mag.*, vol. 26, no. 5, pp. 51–56, 2007.

[26] L. Gortzis, I. Bakettas, C. Makropoulos, G. Graschew, and G. Nikiforidis, 'Portable biomedical devices: a critical issue during telecare services design', *Inform. Health Soc. Care*, vol. 33, no. 2, pp. 91–98, 2008.

[27] S. Das and M. Pal, 'Non-invasive monitoring of human health by exhaled breath analysis: A comprehensive review', *J. Electrochem. Soc.*, vol. 167, no. 3, p. 037562, 2020.

[28] B. Sumathy, S. Kavimullai, S. Shushmithaa, and S. S. Anusha, 'Wearable Non-invasive Health Monitoring Device for Elderly using IOT', presented at the IOP Conference Series: Materials Science and Engineering, IOP Publishing, 2021, p. 012011.

[29] M. A. Almarshad, M. S. Islam, S. Al-Ahmadi, and A. S. BaHammam, 'Diagnostic features and potential applications of PPG signal in healthcare: A systematic review', presented at the Healthcare, MDPI, 2022, p. 547.

[30] E. Finnegan *et al.*, 'Pulse arrival time as a surrogate of blood pressure', *Sci. Rep.*, vol. 11, no. 1, p. 22767, 2021.

[31] R. Pernice *et al.*, 'Comparison of short-term heart rate variability indexes evaluated through electrocardiographic and continuous blood pressure monitoring', *Med. Biol. Eng. Comput.*, vol. 57, no. 6, pp. 1247–1263, 2019.

[32] P. H. Charlton *et al.*, 'Extraction of respiratory signals from the electrocardiogram and photoplethysmogram: technical and physiological determinants', *Physiol. Meas.*, vol. 38, no. 5, p. 669, 2017.

[33] N. Daimiwal, M. Sundhararajan, and R. Shriram, 'Respiratory rate, heart rate and continuous measurement of BP using PPG', in *2014 International Conference on Communication and Signal Processing*, Melmaruvathur, India: IEEE, Apr. 2014, pp. 999–1002. doi: 10.1109/ICCSP.2014.6949996.

[34] D. Dias and J. Paulo Silva Cunha, 'Wearable Health Devices—Vital Sign Monitoring, Systems and Technologies', *Sensors*, vol. 18, no. 8, p. 2414, Jul. 2018, doi: 10.3390/s18082414.

[35] T. Amin, R. J. Mobbs, N. Mostafa, L. W. Sy, and W. J. Choy, 'Wearable devices for patient monitoring in the early postoperative period: a literature review', *Mhealth*, vol. 7, 2021.

[36] A. Kos and A. Umek, 'Wearable Sensor Devices for Prevention and Rehabilitation in Healthcare: Swimming Exercise With Real-Time Therapist Feedback', *IEEE Internet Things J.*, vol. 6, no. 2, pp. 1331–1341, Apr. 2019, doi: 10.1109/JIOT.2018.2850664.

[37] A. Mahajan, G. Pottie, and W. Kaiser, 'Transformation in healthcare by wearable devices for diagnostics and guidance of treatment', *ACM Trans. Comput. Healthc.*, vol. 1, no. 1, pp. 1–12, 2020.

[38] T. Pancar and S. Ozkan Yildirim, 'Exploring factors affecting consumers' adoption of wearable devices to track health data', *Univers. Access Inf. Soc.*, vol. 22, no. 2, pp. 331–349, 2023.

[39] M. Nissen *et al.*, 'Heart rate measurement accuracy of fitbit charge 4 and samsung galaxy watch active2: Device evaluation study', *JMIR Form. Res.*, vol. 6, no. 3, p. e33635, 2022.

[40] E. D. Chinoy, J. A. Cuellar, J. T. Jameson, and R. R. Markwald, 'Performance of four commercial wearable sleep-tracking devices tested under unrestricted conditions at home in healthy young adults', *Nat. Sci. Sleep*, pp. 493–516, 2022.

[41] G. Y. Lui, D. Loughnane, C. Polley, T. Jayarathna, and P. P. Breen, 'The apple watch for monitoring mental health–related physiological symptoms: Literature review', *JMIR Ment. Health*, vol. 9, no. 9, p. e37354, 2022.

[42] M. Meira E Cruz, C. Zhou, M. H. Kryger, and H. Wang, 'Validation of a Smart Ring Oximeter in Individuals With Dark Skin Pigment', *Mayo Clin. Proc. Digit. Health*, vol. 1, no. 3, pp. 357–365, Sep. 2023, doi: 10.1016/j.mcpdig.2023.06.012.

[43] M. Ghobakhloo, 'Industry 4.0, digitization, and opportunities for sustainability', *J. Clean. Prod.*, vol. 252, p. 119869, 2020.

[44] R. Dwivedi, D. Mehrotra, and S. Chandra, 'Potential of Internet of Medical Things (IoMT) applications in building a smart healthcare system: A systematic review', *J. Oral Biol. Craniofacial Res.*, vol. 12, no. 2, pp. 302–318, 2022.

[45] P. P. Ray, D. Dash, and N. Kumar, 'Sensors for internet of medical things: State-of-the-art, security and privacy issues, challenges and future directions', *Comput. Commun.*, vol. 160, pp. 111–131, 2020.

[46] M. A. Habib *et al.*, 'Privacy-based medical data protection against internal security threats in heterogeneous Internet of Medical Things', *Int. J. Distrib. Sens. Netw.*, vol. 15, no. 9, p. 1550147719875653, 2019.

[47] A. J. Casson, A. Vazquez Galvez, and D. Jarchi, 'Gyroscope vs. accelerometer measurements of motion from wrist PPG during physical exercise', *ICT Express*, vol. 2, no. 4, pp. 175–179, Dec. 2016, doi: 10.1016/j.icte.2016.11.003.

[48] O. Such, 'Motion tolerance in wearable sensors-The challenge of motion artifact', presented at the 2007 29th Annual International Conference of the IEEE Engineering in Medicine and Biology Society, IEEE, 2007, pp. 1542–1545.

[49] F. Shaffer and J. P. Ginsberg, 'An Overview of Heart Rate Variability Metrics and Norms', *Front. Public Health*, vol. 5, p. 258, Sep. 2017, doi: 10.3389/fpubh.2017.00258.

[50] J. A. Hirsch and B. Bishop, 'Respiratory sinus arrhythmia in humans: how breathing pattern modulates heart rate', *Am. J. Physiol.-Heart Circ. Physiol.*, vol. 241, no. 4, pp. H620–H629, Oct. 1981, doi: 10.1152/ajpheart.1981.241.4.H620.

[51] Society for Psychophysiological Research Ad Hoc Committee on Electrodermal Measures, 'Publication recommendations for electrodermal measurements: Publication standards for EDA', *Psychophysiology*, vol. 49, no. 8, pp. 1017–1034, Aug. 2012, doi: 10.1111/j.1469-8986.2012.01384.x.

[52] S. Aghanavesi, F. Bergquist, D. Nyholm, M. Senek, and M. Memedi, 'Motion sensor-based assessment of Parkinson's disease motor symptoms during leg agility tests: results from levodopa challenge', *IEEE J. Biomed. Health Inform.*, vol. 24, no. 1, pp. 111–119, 2019.

[53] N. Montano *et al.*, 'Heart rate variability explored in the frequency domain: a tool to investigate the link between heart and behavior', *Neurosci. Biobehav. Rev.*, vol. 33, no. 2, pp. 71–80, 2009.

[54] R. Pernice *et al.*, 'Time, frequency and information domain analysis of short-term heart rate variability before and after focal and generalized seizures in epileptic children', *Physiol. Meas.*, vol. 40, no. 7, p. 074003, 2019.

[55] M. Benedek and C. Kaernbach, 'A continuous measure of phasic electrodermal activity', *J. Neurosci. Methods*, vol. 190, no. 1, pp. 80–91, Jun. 2010, doi: 10.1016/j.jneumeth.2010.04.028.

[56] P. Castiglioni, G. Parati, and A. Faini, 'Information-domain analysis of cardiovascular complexity: Night and day modulations of entropy and the effects of hypertension', *Entropy*, vol. 21, no. 6, p. 550, 2019.

[57] R. Castaldo, L. Montesinos, P. Melillo, C. James, and L. Pecchia, 'Ultra-short term HRV features as surrogates of short term HRV: A case study on mental stress detection in real life', *BMC Med. Inform. Decis. Mak.*, vol. 19, no. 1, pp. 1–13, 2019.

[58] H. J. Baek, C.-H. Cho, J. Cho, and J.-M. Woo, 'Reliability of ultra-short-term analysis as a surrogate of standard 5-min analysis of heart rate variability', *Telemed. E-Health*, vol. 21, no. 5, pp. 404–414, 2015.

[59] S. M. Yun *et al.*, 'Recent advances in wearable devices for non-invasive sensing', *Appl. Sci.*, vol. 11, no. 3, p. 1235, 2021.

[60] J. Matthews, J. Kim, and W. Yeo, 'Advances in Biosignal Sensing and Signal Processing Methods with Wearable Devices', *Anal. Sens.*, vol. 3, no. 2, p. e202200062, 2023.

[61] R. Pernice, G. Nollo, M. Zanetti, M. De Cecco, A. Busacca, and L. Faes, 'Minimally invasive assessment of mental stress based on wearable wireless physiological sensors and multivariate biosignal processing', presented at the IEEE EUROCON 2019-18th International Conference on Smart Technologies, IEEE, 2019, pp. 1–5.

[62] C. Barà, R. Pernice, L. Sparacino, Y. Antonacci, M. Javorka, and L. Faes, 'Analysis of Cardiac Pulse Arrival Time Series at Rest and during Physiological Stress', presented at the 2022 IEEE 21st Mediterranean Electrotechnical Conference (MELECON), IEEE, 2022, pp. 926–931.

[63] M. Van Dooren, J. J. G. (Gert-J. De Vries, and J. H. Janssen, 'Emotional sweating across the body: Comparing 16 different skin conductance measurement locations', *Physiol. Behav.*, vol. 106, no. 2, pp. 298–304, May 2012, doi: 10.1016/j.physbeh.2012.01.020.

[64] S. Valenti *et al.*, 'Wearable Multisensor Ring-Shaped Probe for Assessing Stress and Blood Oxygenation: Design and Preliminary Measurements', *Biosensors*, vol. 13, no. 4, p. 460, Apr. 2023, doi: 10.3390/bios13040460.

[65] M. AlGhatrif and J. Lindsay, 'A brief review: history to understand fundamentals of electrocardiography', *J. Community Hosp. Intern. Med. Perspect.*, vol. 2, no. 1, p. 14383, 2012.

[66] S. K. Berkaya, A. K. Uysal, E. S. Gunal, S. Ergin, S. Gunal, and M. B. Gulmezoglu, 'A survey on ECG analysis', *Biomed. Signal Process. Control*, vol. 43, pp. 216–235, 2018.

[67] T. B. Garcia, *12-lead ECG: The art of interpretation*. Jones & Bartlett Learning, 2015.

[68] S. McStay, 'Recording a 12-lead electrocardiogram (ECG)', *Br. J. Nurs.*, vol. 28, no. 12, pp. 756–760, 2019.

[69] Y.-C. Yeh and W.-J. Wang, 'QRS complexes detection for ECG signal: The Difference Operation Method', *Comput. Methods Programs Biomed.*, vol. 91, no. 3, pp. 245–254, 2008.

[70] A. K. Bhoi and K. S. Sherpa, 'QRS Complex Detection and Analysis of Cardiovascular Abnormalities: A Review.', *Int. J. Bioautomation*, vol. 18, no. 3, 2014.

[71] M. B. Simson, 'Use of signals in the terminal QRS complex to identify patients with ventricular tachycardia after myocardial infarction.', *Circulation*, vol. 64, no. 2, pp. 235–242, 1981.

[72] C. Varon, A. Caicedo, D. Testelmans, B. Buyse, and S. Van Huffel, 'A novel algorithm for the automatic detection of sleep apnea from single-lead ECG', *IEEE Trans. Biomed. Eng.*, vol. 62, no. 9, pp. 2269–2278, 2015.

[73] H. Y. Gu, J. Huang, X. Liu, S. Q. Qiao, and X. Cao, 'Effectiveness of single-lead ECG devices for detecting atrial fibrillation: An overview of systematic reviews', *Worldviews Evidence-Based Nurs.*, 2023.

[74] N. Isakadze and S. S. Martin, 'How useful is the smartwatch ECG?', *Trends Cardiovasc. Med.*, vol. 30, no. 7, pp. 442–448, 2020.

[75] N. Saghir, A. Aggarwal, N. Soneji, V. Valencia, G. Rodgers, and T. Kurian, 'A comparison of manual electrocardiographic interval and waveform analysis in lead 1 of 12-lead ECG and Apple Watch ECG: a validation study', *Cardiovasc. Digit. Health J.*, vol. 1, no. 1, pp. 30–36, 2020.

[76] J. Allen, 'Photoplethysmography and its application in clinical physiological measurement', *Physiol. Meas.*, vol. 28, no. 3, pp. R1–R39, Mar. 2007, doi: 10.1088/0967-3334/28/3/R01.

[77] S. Valenti *et al.*, 'A silicon photomultiplier-based analog front-end for DC component rejection and pulse wave recording in photoplethysmographic applications', presented at the 2022 IEEE International Symposium on Medical Measurements and Applications (MeMeA), IEEE, 2022, pp. 1–6.

[78] T. Ishikawa, Y. Hyodo, K. Miyashita, K. Yoshifuji, Y. Komoriya, and Y. Imai, 'Wearable motion tolerant PPG sensor for instant heart rate in daily activity', presented at the International Conference on Bio-Inspired Systems and Signal Processing, SCITEPRESS, 2017, pp. 126–133.

[79] P. Nabeel, J. Jayaraj, and S. Mohanasankar, 'Single-source PPG-based local pulse wave velocity measurement: a potential cuffless blood pressure estimation technique', *Physiol. Meas.*, vol. 38, no. 12, p. 2122, 2017.

[80] R. P. Smith, J. Argod, J.-L. Pépin, and P. A. Lévy, 'Pulse transit time: an appraisal of potential clinical applications', *Thorax*, vol. 54, no. 5, pp. 452–457, 1999.

[81] R. Pernice *et al.*, 'Reliability of short-term heart rate variability indexes assessed through photoplethysmography', presented at the 2018 40th Annual International Conference of the IEEE Engineering in Medicine and Biology Society (EMBC), IEEE, 2018, pp. 5610–5513.

[82] A. Schäfer and J. Vagedes, 'How accurate is pulse rate variability as an estimate of heart rate variability?: A review on studies comparing photoplethysmographic technology with an electrocardiogram', *Int. J. Cardiol.*, vol. 166, no. 1, pp. 15–29, 2013.

[83] J. J. Braithwaite, D. G. Watson, R. Jones, and M. Rowe, 'A guide for analysing electrodermal activity (EDA) & skin conductance responses (SCRs) for psychological experiments', *Psychophysiology*, vol. 49, no. 1, pp. 1017–1034, 2013.

[84] H. Selye, 'Forty years of stress research: principal remaining problems and misconceptions'.

[85] A. J. Cunanan *et al.*, 'The General Adaptation Syndrome: A Foundation for the Concept of Periodization', *Sports Med.*, vol. 48, no. 4, pp. 787–797, Apr. 2018, doi: 10.1007/s40279-017-0855-3.

[86] R. R. Freedman and P. Ianni, 'Role of cold and emotional stress in Raynaud's disease and scleroderma.', *Br. Med. J. Clin. Res. Ed*, vol. 287, no. 6404, p. 1499, 1983.

[87] G. Volpes, S. Valenti, A. Parisi, A. Busacca, L. Faes, and R. Pernice, 'Low-invasive multisensor real-time acquisition system for the assessment of cardiorespiratory and skin conductance parameters', presented at the 2022 IEEE 21st Mediterranean Electrotechnical Conference (MELECON), IEEE, 2022, pp. 936–941.

[88] H.-G. Kim, E.-J. Cheon, D.-S. Bai, Y. H. Lee, and B.-H. Koo, 'Stress and heart rate variability: a meta-analysis and review of the literature', *Psychiatry Investig.*, vol. 15, no. 3, p. 235, 2018.

[89] J. F. Thayer, S. S. Yamamoto, and J. F. Brosschot, ‘The relationship of autonomic imbalance, heart rate variability and cardiovascular disease risk factors’, *Int. J. Cardiol.*, vol. 141, no. 2, pp. 122–131, 2010.

[90] J. A. Healey and R. W. Picard, ‘Detecting stress during real-world driving tasks using physiological sensors’, *IEEE Trans. Intell. Transp. Syst.*, vol. 6, no. 2, pp. 156–166, 2005.

[91] J. Hernandez, P. Paredes, A. Roseway, and M. Czerwinski, ‘Under pressure: sensing stress of computer users’, presented at the Proceedings of the SIGCHI conference on Human factors in computing systems, 2014, pp. 51–60.

[92] A. Alberdi, A. Aztiria, and A. Basarab, ‘Towards an automatic early stress recognition system for office environments based on multimodal measurements: A review’, *J. Biomed. Inform.*, vol. 59, pp. 49–75, 2016.

[93] M. M. Jo∅ rgensen and R. Zachariae, ‘Autonomic reactivity to cognitive and emotional stress of low, medium, and high hypnotizable healthy subjects: Testing predictions from the high risk model of threat perception’, *Int. J. Clin. Exp. Hypn.*, vol. 50, no. 3, pp. 248–275, 2002.

[94] L. Arya and D. Sethia, ‘HRV and GSR as Viable Physiological Markers for Mental Health Recognition’, presented at the 2022 14th International Conference on COMmunication Systems & NETworkS (COMSNETS), IEEE, 2022, pp. 37–42.

[95] H. F. Posada-Quintero and J. B. Bolkhovsky, ‘Machine learning models for the identification of cognitive tasks using autonomic reactions from heart rate variability and electrodermal activity’, *Behav. Sci.*, vol. 9, no. 4, p. 45, 2019.

[96] A. Jain and V. Kanhangad, ‘Human Activity Classification in Smartphones Using Accelerometer and Gyroscope Sensors’, *IEEE Sens. J.*, vol. 18, no. 3, pp. 1169–1177, Feb. 2018, doi: 10.1109/JSEN.2017.2782492.

[97] R. Ahmed Bhuiyan, N. Ahmed, M. Amiruzzaman, and M. R. Islam, ‘A Robust Feature Extraction Model for Human Activity Characterization Using 3-Axis Accelerometer and Gyroscope Data’, *Sensors*, vol. 20, no. 23, p. 6990, Dec. 2020, doi: 10.3390/s20236990.

[98] D. Pollreisz and N. TaheriNejad, ‘Detection and Removal of Motion Artifacts in PPG Signals’, *Mob. Netw. Appl.*, vol. 27, no. 2, pp. 728–738, Apr. 2022, doi: 10.1007/s11036-019-01323-6.

[99] Y. Maeda, M. Sekine, and T. Tamura, 'Relationship between measurement site and motion artifacts in wearable reflected photoplethysmography', *J. Med. Syst.*, vol. 35, pp. 969–976, 2011.

[100] S. Ismail, U. Akram, and I. Siddiqi, 'Heart rate tracking in photoplethysmography signals affected by motion artifacts: A review', *EURASIP J. Adv. Signal Process.*, vol. 2021, no. 1, pp. 1–27, 2021.

[101] H. Chung, H. Ko, H. Lee, and J. Lee, 'Deep Learning for Heart Rate Estimation From Reflectance Photoplethysmography With Acceleration Power Spectrum and Acceleration Intensity', *IEEE Access*, vol. 8, pp. 63390–63402, 2020, doi: 10.1109/ACCESS.2020.2981956.

[102] R. J. Mitchell, S. R. Lord, L. A. Harvey, and J. C. T. Close, 'Obesity and falls in older people: Mediating effects of disease, sedentary behavior, mood, pain and medication use', *Arch. Gerontol. Geriatr.*, vol. 60, no. 1, pp. 52–58, Jan. 2015, doi: 10.1016/j.archger.2014.09.006.

[103] M. A. Cohen and J. A. Taylor, 'Short-term cardiovascular oscillations in man: measuring and modelling the physiologies', *J. Physiol.*, vol. 542, no. 3, pp. 669–683, 2002.

[104] S. C. Malpas, 'Neural influences on cardiovascular variability: possibilities and pitfalls', *Am. J. Physiol.-Heart Circ. Physiol.*, vol. 282, no. 1, pp. H6–H20, 2002.

[105] S. Schulz *et al.*, 'Cardiovascular and cardiorespiratory coupling analyses: a review', *Philos. Trans. R. Soc. Math. Phys. Eng. Sci.*, vol. 371, no. 1997, p. 20120191, 2013.

[106] A. J. Camm *et al.*, 'Heart rate variability: standards of measurement, physiological interpretation and clinical use. Task Force of the European Society of Cardiology and the North American Society of Pacing and Electrophysiology', *Circulation*, vol. 93, no. 5, pp. 1043–1065, 1996.

[107] A. Porta *et al.*, 'K-nearest-neighbor conditional entropy approach for the assessment of the short-term complexity of cardiovascular control', *Physiol. Meas.*, vol. 34, no. 1, p. 17, 2012.

[108] R. Sassi *et al.*, 'Advances in heart rate variability signal analysis: joint position statement by the e-Cardiology ESC Working Group and the European Heart Rhythm Association co-endorsed by the Asia Pacific Heart Rhythm Society', *Ep Eur.*, vol. 17, no. 9, pp. 1341–1353, 2015.

[109] J. S. Richman and J. R. Moorman, 'Physiological time-series analysis using approximate entropy and sample entropy', *Am. J. Physiol.-Heart Circ. Physiol.*, vol. 278, no. 6, pp. H2039–H2049, 2000.

[110] A. Porta, S. Guzzetti, R. Furlan, T. Gnecchi-Ruscone, N. Montano, and A. Malliani, 'Complexity and nonlinearity in short-term heart period variability: comparison of methods based on local nonlinear prediction', *IEEE Trans. Biomed. Eng.*, vol. 54, no. 1, pp. 94–106, 2006.

[111] C.-M. Chen *et al.*, 'Towards Wearable and Flexible Sensors and Circuits Integration for Stress Monitoring', *IEEE J. Biomed. Health Inform.*, vol. 24, no. 8, pp. 2208–2215, Aug. 2020, doi: 10.1109/JBHI.2019.2957444.

[112] M. Umair, N. Chalabianloo, C. Sas, and C. Ersoy, 'HRV and stress: A mixed-methods approach for comparison of wearable heart rate sensors for biofeedback', *IEEE Access*, vol. 9, pp. 14005–14024, 2021.

[113] D. Hernando, S. Roca, J. Sancho, Á. Alesanco, and R. Bailón, 'Validation of the apple watch for heart rate variability measurements during relax and mental stress in healthy subjects', *Sensors*, vol. 18, no. 8, p. 2619, 2018.

[114] P. Kakria, N. K. Tripathi, and P. Kitipawang, 'A Real-Time Health Monitoring System for Remote Cardiac Patients Using Smartphone and Wearable Sensors', *Int. J. Telemed. Appl.*, vol. 2015, pp. 1–11, 2015, doi: 10.1155/2015/373474.

[115] J. W. Kim, H. S. Seok, and H. Shin, 'Is ultra-short-term heart rate variability valid in non-static conditions?', *Front. Physiol.*, vol. 12, p. 596060, 2021.

[116] M. Finžgar and P. Podržaj, 'Feasibility of assessing ultra-short-term pulse rate variability from video recordings', *PeerJ*, vol. 8, p. e8342, 2020.

[117] C. J. Holmes, M. V. Fedewa, L. J. Winchester, H. V. MacDonald, S. A. Wind, and M. R. Esco, 'Validity of smartphone heart rate variability pre-and post-resistance exercise', *Sensors*, vol. 20, no. 20, p. 5738, 2020.

[118] F. Shaffer, S. Shearman, and Z. M. Meehan, 'The promise of ultra-short-term (UST) heart rate variability measurements', *Biofeedback*, vol. 44, no. 4, pp. 229–233, 2016.

[119] L. Pecchia, R. Castaldo, L. Montesinos, and P. Melillo, 'Are ultra-short heart rate variability features good surrogates of short-term ones? State-of-the-art review and recommendations', *Healthc. Technol. Lett.*, vol. 5, no. 3, pp. 94–100, 2018.

[120] G. R. Sandercock, P. D. Bromley, and D. A. Brodie, 'The reliability of short-term measurements of heart rate variability', *Int. J. Cardiol.*, vol. 103, no. 3, pp. 238–247, 2005.

[121] C. L. Protheroe, H. R. J. Ravensbergen, J. A. Inskip, and V. E. Claydon, 'Tilt Testing with Combined Lower Body Negative Pressure: a', *JoVE J. Vis. Exp.*, no. 73, p. e4315, 2013.

[122] M. Malik, H. Huikuri, F. Lombardi, G. Schmidt, and e-Health/Digital Rhythm Study Group of the European Heart Rhythm Association, 'The purpose of heart rate variability measurements', *Clin. Auton. Res.*, vol. 27, pp. 139–140, 2017.

[123] M. Vollmer, 'A robust, simple and reliable measure of heart rate variability using relative RR intervals', presented at the 2015 Computing in Cardiology Conference (CinC), IEEE, 2015, pp. 609–612.

[124] F. Shaffer, R. McCraty, and C. L. Zerr, 'A healthy heart is not a metronome: an integrative review of the heart's anatomy and heart rate variability', *Front. Psychol.*, vol. 5, p. 1040, 2014.

[125] M. Valente *et al.*, 'Univariate and multivariate conditional entropy measures for the characterization of short-term cardiovascular complexity under physiological stress', *Physiol. Meas.*, vol. 39, no. 1, p. 014002, 2018.

[126] W. Xiong, L. Faes, and P. C. Ivanov, 'Entropy measures, entropy estimators, and their performance in quantifying complex dynamics: Effects of artifacts, nonstationarity, and long-range correlations', *Phys. Rev. E*, vol. 95, no. 6, p. 062114, 2017.

[127] H. Azami, L. Faes, J. Escudero, A. Humeau-Heurtier, and L. E. Silva, 'Entropy Analysis of Univariate Biomedical Signals: Review and Comparison of Methods', 2020.

[128] G. D. Hutcheson, 'Ordinary least-squares regression', *Moutinho GD Hutcheson SAGE Dict. Quant. Manag. Res.*, pp. 224–228, 2011.

[129] L. Faes, S. Erla, A. Porta, and G. Nollo, 'A framework for assessing frequency domain causality in physiological time series with instantaneous effects', *Philos. Trans. R. Soc. Math. Phys. Eng. Sci.*, vol. 371, no. 1997, p. 20110618, 2013.

[130] L. Faes, S. Stramaglia, and D. Marinazzo, 'On the interpretability and computational reliability of frequency-domain Granger causality', *F1000Research*, vol. 6, 2017.

[131] C. W. J. Granger, 'Investigating causal relations by econometric models and cross-spectral methods', *Econom. J. Econom. Soc.*, pp. 424–438, 1969.

[132] J. Geweke, 'Measurement of linear dependence and feedback between multiple time series', *J. Am. Stat. Assoc.*, vol. 77, no. 378, pp. 304–313, 1982.

[133] D. Chicharro, 'On the spectral formulation of Granger causality', *Biol. Cybern.*, vol. 105, no. 5–6, pp. 331–347, 2011.

[134] O. N. Rahma *et al.*, 'Electrodermal activity for measuring cognitive and emotional stress level', *J. Med. Signals Sens.*, vol. 12, no. 2, p. 155, 2022.

[135] S. Prahl, 'Optical absorption of hemoglobin', *Or. Med. Cent. News*, 1999.

[136] O. Yossef Hay *et al.*, 'Pulse oximetry with two infrared wavelengths without calibration in extracted arterial blood', *Sensors*, vol. 18, no. 10, p. 3457, 2018.

[137] M. Abtahi, A. M. Amiri, D. Byrd, and K. Mankodiya, 'Hand motion detection in fNIRS neuroimaging data', presented at the Healthcare, MDPI, 2017, p. 20.

[138] S.-S. Oak and P. Aroul, 'How to design peripheral oxygen saturation (SpO2) and optical heart rate monitoring (OHRM) systems using the AFE4403', *Tex. Instrum.*, 2015.

[139] S. Lopez and R. Americas, 'Pulse oximeter fundamentals and design', *Free Scale Semicond.*, p. 23, 2012.

[140] E. D. Chan, M. M. Chan, and M. M. Chan, 'Pulse oximetry: understanding its basic principles facilitates appreciation of its limitations', *Respir. Med.*, vol. 107, no. 6, pp. 789–799, 2013.

[141] K. A. Reddy, B. George, N. M. Mohan, and V. J. Kumar, 'A novel calibration-free method of measurement of oxygen saturation in arterial blood', *IEEE Trans. Instrum. Meas.*, vol. 58, no. 5, pp. 1699–1705, 2009.

[142] A. Fusco, D. Locatelli, F. Onorati, G. C. Durelli, and M. D. Santambrogio, 'On how to extract breathing rate from PPG signal using wearable devices', presented at the 2015 IEEE Biomedical Circuits and Systems Conference (BioCAS), IEEE, 2015, pp. 1–4.

[143] K. V. Madhav, M. R. Ram, E. H. Krishna, N. R. Komalla, and K. A. Reddy, 'Estimation of respiration rate from ECG, BP and PPG signals using empirical mode decomposition', presented at the 2011 IEEE International Instrumentation and Measurement Technology Conference, IEEE, 2011, pp. 1–4.

[144] STMicroelectronics, 'MCU STM32L432KC'. Datasheet. Accessed: Sep. 05, 2023. [Online]. Available: https://www.st.com/resource/en/datasheet/stm32l432kc.pdf

[145] J. Hohl and S. Rush, 'The complete heart-lead relationship in the einthoven triangle', *Bull. Math. Biophys.*, vol. 30, no. 4, pp. 615–623, Dec. 1968, doi: 10.1007/BF02476678.

[146] I. Natgunanathan, N. Fernando, S. W. Loke, and C. Weerasuriya, 'Bluetooth Low Energy Mesh: Applications, Considerations and Current State-of-the-Art', *Sensors*, vol. 23, no. 4, p. 1826, 2023.

[147] Analog Devices, Inc., 'MAX30102-High-Sensitivity Pulse Oximeter and Heart-Rate Sensor for Wearable Health'. Datasheet. Accessed: Sep. 05, 2023. [Online]. Available: https://www.analog.com/media/en/technical-documentation/data-sheets/MAX30102.pdf

[148] Analog Devices, Inc., 'AD8232-Single-Lead, Heart Rate Monitor Front End'. Datasheet. Accessed: Sep. 05, 2023. [Online]. Available: https://www.analog.com/media/en/technical-documentation/data-sheets/ad8232.pdf

[149] InvenSense, Inc., 'MPU-6000 and MPU-6050 Product Specification'. Datasheet. Accessed: Sep. 05, 2023. [Online]. Available: https://invensense.tdk.com/wp-content/uploads/2015/02/MPU-6000-Datasheet1.pdf

[150] JN Huamao Technology Co., Ltd., 'HM-18/HM-19 BLE module'. Datasheet. Accessed: Jan. 22, 2024. [Online]. Available: https://acoptex.com/uploads/bluetooth40_en.pdf

[151] Analog Devices, Inc., 'LTC4056-4.2 Linear Li-Ion Charger with Termination in thinSOT'. Datasheet. Accessed: Jan. 22, 2024. [Online]. Available: https://www.analog.com/media/en/technical-documentation/data-sheets/405642f.pdf

[152] Analog Devices, Inc., 'ADP7118 Low Noise, CMOS LDO Linear Regulator'. Datasheet. Accessed: Jan. 22, 2024. [Online]. Available: https://www.analog.com/media/en/technical-documentation/data-sheets/adp7118.pdf

[153] STMicroelectronics, 'STM32CubeMX - initialization code generator'. Databrief. Accessed: Jan. 22, 2024. [Online]. Available: https://www.st.com/en/development-tools/stm32cubemx.html

[154] STMicroelectronics, 'STM32CubeIDE - integrated Development Environment for STM32'. Databrief. Accessed: Jan. 22, 2024. [Online]. Available: https://www.st.com/en/development-tools/stm32cubeide.html

[155] STMicroelectronics, 'UM1884 - Description of STM32L4/L4+ HAL and low-layer drivers'. User manual. Accessed: Jan. 22, 2024. [Online]. Available: https://www.st.com/resource/en/user_manual/um1884-description-of-stm32l4l4-hal-and-lowlayer-drivers-stmicroelectronics.pdf

[156] H. Sedghamiz, 'Matlab Implementation of Pan Tompkins ECG QRS Detector.'.

[157] R. B. Blackman and J. W. Tukey, 'The measurement of power spectra from the point of view of communications engineering—Part I', *Bell Syst. Tech. J.*, vol. 37, no. 1, pp. 185–282, 1958.

[158] F. Shaffer, Z. M. Meehan, and C. L. Zerr, 'A critical review of ultra-short-term heart rate variability norms research', *Front. Neurosci.*, vol. 14, p. 594880, 2020.

[159] G. Volpes *et al.*, 'Feasibility of Ultra-short Term Complexity Analysis of Heart Rate Variability in Resting State and During Orthostatic Stress', in *2022 12th Conference of the European Study Group on Cardiovascular Oscillations (ESGCO)*, Vysoké Tatry, Štrbské Pleso, Slovakia: IEEE, Oct. 2022, pp. 1–2. doi: 10.1109/ESGCO55423.2022.9931388.

[160] M. Javorka *et al.*, 'Basic cardiovascular variability signals: mutual directed interactions explored in the information domain', *Physiol. Meas.*, vol. 38, no. 5, p. 877, 2017.

[161] M. Javorka *et al.*, 'Towards understanding the complexity of cardiovascular oscillations: Insights from information theory', *Comput. Biol. Med.*, vol. 98, pp. 48–57, 2018.

[162] M. L. Munoz *et al.*, 'Validity of (ultra-) short recordings for heart rate variability measurements', *PloS One*, vol. 10, no. 9, p. e0138921, 2015.

[163] M. R. Esco and A. A. Flatt, 'Ultra-short-term heart rate variability indexes at rest and post-exercise in athletes: evaluating the agreement with accepted recommendations', *J. Sports Sci. Med.*, vol. 13, no. 3, p. 535, 2014.

[164] I. Cohen *et al.*, 'Pearson correlation coefficient', *Noise Reduct. Speech Process.*, pp. 1–4, 2009.

[165] C. O. Fritz, P. E. Morris, and J. J. Richler, 'Effect size estimates: current use, calculations, and interpretation.', *J. Exp. Psychol. Gen.*, vol. 141, no. 1, p. 2, 2012.

[166] J. Cohen, *Statistical power analysis for the behavioral sciences*. Academic press, 2013.

[167] M. Baumert, B. Czippelova, A. Ganesan, M. Schmidt, S. Zaunseder, and M. Javorka, 'Entropy analysis of RR and QT interval variability during orthostatic and mental stress in healthy subjects', *Entropy*, vol. 16, no. 12, pp. 6384–6393, 2014.

[168] W. L. Wasmund, E. C. Westerholm, D. E. Watenpaugh, S. L. Wasmund, and M. L. Smith, 'Interactive effects of mental and physical stress on cardiovascular control', *J. Appl. Physiol.*, vol. 92, no. 5, pp. 1828–1834, 2002.

[169] J. Paton, P. Boscan, A. Pickering, and E. Nalivaiko, 'The yin and yang of cardiac autonomic control: vago-sympathetic interactions revisited', *Brain Res. Rev.*, vol. 49, no. 3, pp. 555–565, 2005.

[170] G. G. Berntson, J. T. Cacioppo, P. F. Binkley, B. N. Uchino, K. S. Quigley, and A. Fieldstone, 'Autonomic cardiac control. III. Psychological stress and cardiac response in autonomic space as revealed by pharmacological blockades', *Psychophysiology*, vol. 31, no. 6, pp. 599–608, 1994.

[171] L. Faes, A. Porta, R. Cucino, S. Cerutti, R. Antolini, and G. Nollo, 'Causal transfer function analysis to describe closed loop interactions between cardiovascular and cardiorespiratory variability signals', *Biol. Cybern.*, vol. 90, no. 6, pp. 390–399, 2004.

[172] A. Porta, R. Furlan, O. Rimoldi, M. Pagani, A. Malliani, and P. Van De Borne, 'Quantifying the strength of the linear causal coupling in closed loop interacting cardiovascular variability signals', *Biol. Cybern.*, vol. 86, pp. 241–251, 2002.

[173] A. Porta *et al.*, 'Causal relationships between heart period and systolic arterial pressure during graded head-up tilt', *Am. J. Physiol.-Regul. Integr. Comp. Physiol.*, vol. 300, no. 2, pp. R378–R386, 2011.

[174] L. Faes, G. Nollo, and A. Porta, 'Information domain approach to the investigation of cardio-vascular, cardio-pulmonary, and vasculo-pulmonary causal couplings', *Front. Physiol.*, vol. 2, p. 80, 2011.

[175] B. E. Westerhof, J. Gisolf, J. M. Karemaker, K. H. Wesseling, N. H. Secher, and J. J. Van Lieshout, 'Time course analysis of baroreflex sensitivity during postural stress', *Am. J. Physiol.-Heart Circ. Physiol.*, vol. 291, no. 6, pp. H2864–H2874, 2006.

[176] G. Mijatovic *et al.*, 'Measuring the rate of information exchange in point-process data with application to cardiovascular variability', *Front. Netw. Physiol.*, vol. 1, p. 765332, 2022.

[177] J. Krohova *et al.*, 'Multiscale information decomposition dissects control mechanisms of heart rate variability at rest and during physiological stress', *Entropy*, vol. 21, no. 5, p. 526, 2019.

[178] H. Pinto, R. Pernice, M. E. Silva, M. Javorka, L. Faes, and A. P. Rocha, 'Multiscale partial information decomposition of dynamic processes with short and long-range correlations: theory and application to cardiovascular control', *Physiol. Meas.*, vol. 43, no. 8, p. 085004, 2022.

[179] A. Porta, T. Gnecchi-Ruscone, E. Tobaldini, S. Guzzetti, R. Furlan, and N. Montano, 'Progressive decrease of heart period variability entropy-based complexity during graded head-up tilt', *J. Appl. Physiol.*, vol. 103, no. 4, pp. 1143–1149, 2007.

[180] R. Pernice, G. Volpes, J. C. Krohova, M. Javorka, A. Busacca, and L. Faes, 'Feasibility of Linear Parametric Estimation of Dynamic Information Measures to assess Physiological Stress from Short-Term Cardiovascular Variability', presented at the 2021 43rd Annual International Conference of the IEEE Engineering in Medicine & Biology Society (EMBC), IEEE, 2021, pp. 290–293.

[181] J. P. Fauvel *et al.*, 'Mental Stress–Induced Increase in Blood Pressure Is Not Related to Baroreflex Sensitivity in Middle-Aged Healthy Men', *Hypertension*, vol. 35, no. 4, pp. 887–891, 2000.

[182] G. Baselli, A. Porta, and M. Pagani, 'Coupling arterial windkessel with peripheral vasomotion: modeling the effects on low-frequency oscillations', *IEEE Trans. Biomed. Eng.*, vol. 53, no. 1, pp. 53–64, 2005.

[183] L. Faes, D. Kugiumtzis, G. Nollo, F. Jurysta, and D. Marinazzo, 'Estimating the decomposition of predictive information in multivariate systems', *Phys. Rev. E*, vol. 91, no. 3, p. 032904, 2015.

[184] P. T. Clemson, J. B. Hoag, W. H. Cooke, D. L. Eckberg, and A. Stefanovska, 'Beyond the baroreflex: A new measure of autonomic regulation based on the time-frequency assessment of variability, phase coherence and couplings', *Front. Netw. Physiol.*, vol. 2, p. 891604, 2022.

[185] L. Faes *et al.*, 'Comparison of methods for the assessment of nonlinearity in short-term heart rate variability under different physiopathological states', *Chaos Interdiscip. J. Nonlinear Sci.*, vol. 29, no. 12, 2019.

[186] N. Bourdillon, L. Schmitt, S. Yazdani, J.-M. Vesin, and G. P. Millet, 'Minimal window duration for accurate HRV recording in athletes', *Front. Neurosci.*, vol. 11, p. 456, 2017.

[187] L. Salahuddin, J. Cho, M. G. Jeong, and D. Kim, 'Ultra short term analysis of heart rate variability for monitoring mental stress in mobile settings', presented at the 2007 29th annual international conference of the ieee engineering in medicine and biology society, IEEE, 2007, pp. 4656–4659.

[188] J. J. Goldberger, F. K. Le, M. Lahiri, P. J. Kannankeril, J. Ng, and A. H. Kadish, 'Assessment of parasympathetic reactivation after exercise', *Am. J. Physiol.-Heart Circ. Physiol.*, vol. 290, no. 6, pp. H2446–H2452, 2006.

[189] J. McNames and M. Aboy, ‘Reliability and accuracy of heart rate variability metrics versus ECG segment duration’, *Med. Biol. Eng. Comput.*, vol. 44, no. 9, pp. 747–756, 2006.

[190] R. Castaldo, L. Montesinos, and L. Pecchia, ‘Ultra-short entropy for mental Stress detection’, presented at the World Congress on Medical Physics and Biomedical Engineering 2018: June 3-8, 2018, Prague, Czech Republic (Vol. 2), Springer, 2018, pp. 287–291.

[191] S. Lee *et al.*, ‘Mental stress assessment using ultra short term HRV analysis based on non-linear method’, *Biosensors*, vol. 12, no. 7, p. 465, 2022.

[192] L. Faes, A. Porta, M. Javorka, and G. Nollo, ‘Efficient computation of multiscale entropy over short biomedical time series based on linear state-space models’, *Complexity*, vol. 2017, 2017.

[193] I. Lazic, R. Pernice, T. Loncar-Turukalo, G. Mijatovic, and L. Faes, ‘Assessment of cardiorespiratory interactions during apneic events in sleep via fuzzy kernel measures of information dynamics’, *Entropy*, vol. 23, no. 6, p. 698, 2021.

[194] R. Pernice *et al.*, ‘Low invasive multisensor acquisition system for real-time monitoring of cardiovascular and respiratory parameters’, presented at the 2020 IEEE 20th mediterranean electrotechnical conference (MELECON), IEEE, 2020, pp. 306–310.

[195] R. Pernice, A. Parisi, G. Adamo, S. Guarino, L. Faes, and A. Busacca, ‘A portable system for multiple parameters monitoring: towards assessment of health conditions and stress level in the automotive field’, presented at the 2019 AEIT International Conference of Electrical and Electronic Technologies for Automotive (AEIT AUTOMOTIVE), IEEE, 2019, pp. 1–6.

[196] D. Nuzzi, L. Faes, M. Javorka, D. Marinazzo, and S. Stramaglia, ‘Inclusion of instantaneous influences in the spectral decomposition of causality: Application to the control mechanisms of heart rate variability’, presented at the 2020 28th European Signal Processing Conference (EUSIPCO), IEEE, 2021, pp. 930–934.

[197] H. Akaike, ‘A new look at the statistical model identification’, *IEEE Trans. Autom. Control*, vol. 19, no. 6, pp. 716–723, 1974.

[198] S. Strano *et al.*, ‘Respiratory sinus arrhythmia and cardiovascular neural regulation in athletes.’, *Med. Sci. Sports Exerc.*, vol. 30, no. 2, pp. 215–219, 1998.

[199] L. Sparacino, R. Pernice, G. Nollo, and L. Faes, 'Causal and Non-Causal Frequency Domain Assessment of Spontaneous Baroreflex Sensitivity after Myocardial Infarction', presented at the 2020 11th Conference of the European Study Group on Cardiovascular Oscillations (ESGCO), IEEE, 2020, pp. 1–2.

[200] R. Pernice, L. Sparacino, G. Nollo, S. Stivala, A. Busacca, and L. Faes, 'Comparison of frequency domain measures based on spectral decomposition for spontaneous baroreflex sensitivity assessment after Acute Myocardial Infarction', *Biomed. Signal Process. Control*, vol. 68, p. 102680, 2021.

[201] J. P. Saul, R. D. Berger, P. Albrecht, S. Stein, M. H. Chen, and Rj. Cohen, 'Transfer function analysis of the circulation: unique insights into cardiovascular regulation', *Am. J. Physiol.-Heart Circ. Physiol.*, vol. 261, no. 4, pp. H1231–H1245, 1991.

[202] G. D. Pinna, R. Maestri, M. T. La Rovere, E. Gobbi, and F. Fanfulla, 'Effect of paced breathing on ventilatory and cardiovascular variability parameters during short-term investigations of autonomic function', *Am. J. Physiol.-Heart Circ. Physiol.*, vol. 290, no. 1, pp. H424–H433, 2006.

[203] J. E. Sanderson *et al.*, 'Impact of changes in respiratory frequency and posture on power spectral analysis of heart rate and systolic blood pressure variability in normal subjects and patients with heart failure', *Clin. Sci.*, vol. 91, no. 1, pp. 35–43, 1996.

[204] R. L. Burr, S. A. Motzer, W. Chen, M. J. Cowan, R. J. Shulman, and M. M. Heitkemper, 'Heart rate variability and 24-hour minimum heart rate', *Biol. Res. Nurs.*, vol. 7, no. 4, pp. 256–267, 2006.

[205] K. Deepak, 'The role of autonomic nervous system in rapid breathing practices', presented at the Proceedings: Science of Breath. International Symposium on Sudarshan Kriya, Pranayam and Consciousness, New Delhi: All India Institute of Medical Sciences, 2002, pp. 42–45.

[206] B. W. Kromenacker, A. A. Sanova, F. I. Marcus, J. J. Allen, and R. D. Lane, 'Vagal mediation of low-frequency heart rate variability during slow yogic breathing', *Psychosom. Med.*, vol. 80, no. 6, pp. 581–587, 2018.

[207] M. Javorka *et al.*, 'Respiratory sinus arrhythmia mechanisms in young obese subjects', *Front. Neurosci.*, vol. 14, p. 204, 2020.

[208] Y. Kwon *et al.*, 'Pulse arrival time, a novel sleep cardiovascular marker: the multi-ethnic study of atherosclerosis', *Thorax*, vol. 76, no. 11, pp. 1124–1130, 2021.

[209] B. Paliakaitė, S. Daukantas, and V. Marozas, ‘Assessment of pulse arrival time for arterial stiffness monitoring on body composition scales’, *Comput. Biol. Med.*, vol. 85, pp. 135–142, 2017.

[210] D. Ray, T. Collins, S. Woolley, and P. Ponnapalli, ‘A review of wearable multi-wavelength photoplethysmography’, *IEEE Rev. Biomed. Eng.*, 2021.

[211] I. Lee, N. Park, H. Lee, C. Hwang, J. H. Kim, and S. Park, ‘Systematic review on human skin-compatible wearable photoplethysmography sensors’, *Appl. Sci.*, vol. 11, no. 5, p. 2313, 2021.

[212] D. Giavarina, ‘Understanding bland altman analysis’, *Biochem. Medica*, vol. 25, no. 2, pp. 141–151, 2015.

[213] N. Stubán and N. Masatsugu, ‘Non-invasive calibration method for pulse oximeters’, *Period. Polytech. Electr. Eng. Arch.*, vol. 52, no. 1–2, pp. 91–94, 2008.

[214] G. Volpes *et al.*, ‘A portable multisensor system to assess cardiorespiratory interactions through photoplethysmography’, presented at the 2022 IEEE International Symposium on Medical Measurements and Applications (MeMeA), IEEE, 2022, pp. 1–6.

[215] K. V. Mardia and R. J. Marshall, ‘Maximum likelihood estimation of models for residual covariance in spatial regression’, *Biometrika*, vol. 71, no. 1, pp. 135–146, 1984.

[216] W. Härdle, J. Horowitz, and J. Kreiss, ‘Bootstrap methods for time series’, *Int. Stat. Rev.*, vol. 71, no. 2, pp. 435–459, 2003.

[217] K. B. Kim and H. J. Baek, ‘Photoplethysmography in Wearable Devices: A Comprehensive Review of Technological Advances, Current Challenges, and Future Directions’, *Electronics*, vol. 12, no. 13, p. 2923, 2023.

[218] A. Soni and K. Rawal, ‘Effect of physical activities on heart rate variability and skin conductance’, *Biomed. Eng. Appl. Basis Commun.*, vol. 33, no. 05, p. 2150038, 2021.

[219] Y. Chee, J. Lee, H. Park, and I. Kim, ‘Baroreflex sensitivity with pulse arrival time’, presented at the 2007 6th International Special Topic Conference on Information Technology Applications in Biomedicine, IEEE, 2007, pp. 67–69.

[220] G. Volpes *et al.*, ‘Feasibility of Ultra-Short-Term Analysis of Heart Rate and Systolic Arterial Pressure Variability at Rest and during Stress via Time-Domain and Entropy-Based Measures’, *Sensors*, vol. 22, no. 23, p. 9149, Nov. 2022, doi: 10.3390/s22239149.

[221] C. J. G. da Cruz, L. G. G. Porto, P. da Silva Rolim, D. de Souza Pires, G. L. Garcia, and G. E. Molina, 'Impact of heart rate on reproducibility of heart rate variability analysis in the supine and standing positions in healthy men', *Clinics*, vol. 74, p. e806, 2019.

[222] R. Perini and A. Veicsteinas, 'Heart rate variability and autonomic activity at rest and during exercise in various physiological conditions', *Eur. J. Appl. Physiol.*, vol. 90, pp. 317–325, 2003.

[223] U. R. Acharya, N. Kannathal, L. M. Hua, and L. M. Yi, 'Study of heart rate variability signals at sitting and lying postures', *J. Bodyw. Mov. Ther.*, vol. 9, no. 2, pp. 134–141, 2005.

[224] N. Watanabe, J. Reece, and B. I. Polus, 'Effects of body position on autonomic regulation of cardiovascular function in young, healthy adults', *Chiropr. Osteopat.*, vol. 15, pp. 1–8, 2007.

[225] E. Mejía-Mejía, K. Budidha, T. Y. Abay, J. M. May, and P. A. Kyriacou, 'Heart rate variability (HRV) and pulse rate variability (PRV) for the assessment of autonomic responses', *Front. Physiol.*, vol. 11, p. 779, 2020.

[226] H. Namazi, 'Complexity and Information-based Analysis of the Heart Rate Variability (HRV) while sitting, hand biking, walking and running', *Fractals*, vol. 29, no. 05, p. 2150201, Aug. 2021, doi: 10.1142/S0218348X21502017.

[227] H. Lee *et al.*, 'Adaptive scheduling of acceleration and gyroscope for motion artifact cancelation in photoplethysmography', *Comput. Methods Programs Biomed.*, vol. 226, p. 107126, Nov. 2022, doi: 10.1016/j.cmpb.2022.107126.